

Kinematical Analysis of Ionization and Fragmentation of Molecules

A Thesis

submitted for the award of Ph.D. degree of

MOHANLAL SUKHADIA UNIVERSITY

in the

Faculty of Science

by

Koushik Saha



Under the Supervision of

Dr. Bhas Bapat

Associate Professor

Space and Atmospheric Sciences Division

Physical Research Laboratory

Ahmedabad, India

DEPARTMENT OF PHYSICS
MOHANLAL SUKHADIA UNIVERSITY
UDAIPUR

Year of submission: 2013

To
my parents

DECLARATION

I, **Mr. Koushik Saha**, S/O Mr. Naba Kumar Saha, resident of Room No:104, PRL Thaltej Hostel, Thaltej, Ahmedabad-380054, hereby declare that the work incorporated in the present thesis entitled, “**Kinematical Analysis of Ionization and Fragmentation of Molecules**” is my own and original. This work (in part or in full) has not been submitted to any University for the award of a Degree or a Diploma. I have properly acknowledged the material collected from secondary sources wherever required. I solely own the responsibility for the originality of the entire content.

Date : December 6, 2013

(Koushik Saha)

CERTIFICATE

I feel great pleasure in certifying that the thesis entitled, “**Kinematical Analysis of Ionization and Fragmentation of Molecules**” embodies a record of the results of investigations carried out by Mr. Koushik Saha under my guidance. He has completed the following requirements as per Ph.D. regulations of the University.

- (a) Course work as per the university rules.
- (b) Residential requirements of the university.
- (c) Regularly submitted six monthly progress reports.
- (c) Presented his work in the departmental committee.
- (d) Published minimum of one research papers in a refereed research journal.

I am satisfied with the analysis of data, interpretation of results and conclusions drawn. I recommend the submission of thesis.

Date : December 6, 2013

Dr. Bhas Bapat
(Thesis Supervisor)
Associate Professor,
Physical Research Laboratory,
Ahmedabad, India

Countersigned by
Head of the Department

Contents

Acknowledgments	ix
Abstract	xiii
List of Publications	xv
Acronyms and Abbreviations	xvii
List of Tables	xix
List of Figures	xxi
1 Introduction	1
1.1 The Molecular Structure	2
1.2 The Perturbed Molecule	8
1.2.1 Ionization	8
1.2.2 Dissociative Ionization	12
1.3 Thesis Overview	14
2 Experimental Techniques	17
2.1 Electron Spectroscopy	18
2.1.1 Cylindrical Mirror Analyzer	18
2.2 Ion Momentum Spectroscopy	20
2.2.1 Time of flight measurement	22
2.2.2 Evaluation of ion momentum	25
2.2.3 Multi-particle coincidence	26

2.3	Experimental set-up	28
2.3.1	Target and excitation source	29
2.3.2	Electron spectrometer	31
2.3.3	Ion momentum Spectrometer	34
2.3.4	Detectors	36
2.3.5	Spectrometer housing and vacuum specifications	40
2.3.6	Data acquisition	40
3	Data Analysis Methodology	45
3.1	Calibration	45
3.1.1	Calibration of the electron spectrum	46
3.1.2	Calibration of the ion ToF spectrum	50
3.2	Ion-ion Coincidence Map	52
3.3	Newton Diagram	56
3.4	Kinetic Energy Release	58
3.5	Dalitz Plot	60
4	Results and Discussions	63
4.1	Valence ionization of CO	64
4.2	Core ionization and fate of excited molecule	70
4.2.1	Auger decay and fragmentation channels of S($2p$) core ion- ized OCS	71
4.2.2	Auger decay and fragmentation channels of S($2p$) core ion- ized CS ₂	76
4.3	Fragmentation kinematics of core ionized molecule	83
4.3.1	Break-up mechanisms of core ionized OCS and CS ₂	83
4.3.2	Kinetic energy release upon fragmentation of OCS and CS ₂ due to various S($2p$) Auger decays	90
4.4	Conformation of the transient molecular ion and its effect on frag- mentation kinematics	96

5 Summary and Future Directions	101
5.1 Summary	101
5.2 Future Scope	103
Bibliography	105
Publications attached with the thesis	113

Acknowledgments

The reason I have got so far as to write this thesis is thanks to all those people whose continuous help and support was always with me. When I look back now, I feel humble with gratitude towards them who have walked with me through all these years of my PhD tenure and made this journey a memorable experience.

First and foremost, I would like to express my heartfelt gratitude to my supervisor, Dr. Bhas Bapat for his guidance and unending support. His enthusiasm, involvement and insight helped me greatly during the long and challenging task of development of the experimental set-up and running the experiments. I cherish the discussions with him, which increased my understanding and motivated me to do better. He gave me immense freedom to carry out research work independently. The quality of my work benefitted greatly from his thorough and critical revision. I thank him for always being there for me and keeping faith in me which gave me encouragement when I needed it the most.

I am obliged to Dr. K P Subramanian for critically reviewing my work and pointing out areas where improvements could be made. His support during the experiments was very crucial. I am grateful to him for the valuable advices and help I received during the course of my PhD.

I am greatly indebted to Dr. S B Banerjee for his continual support during the experiments and otherwise. His joyful company made those long hours during the experiments very enjoyable. I also thank the other members of my group, I A Prajapati, V K Lodha, Dr. B Sivaraman and Prashant Kumar for

their help and also for the wonderful time I had with them. I acknowledge my seniors Rajesh Kushawaha and Arvind Saxena for the stimulating discussions we had on various subjects. I am thankful to my friend Amrendra for his help, suggestions and for those long conversations we had on academic as well as non-academic topics.

The work reported in this thesis stemmed from series of experiments carried out at RRCAT, Indore and IUAC, New Delhi. I deeply appreciate the support given by the staff at IUAC and RRCAT. I am specially grateful to Dr. C P Safvan, Mridula and Ajit for their help while carrying out experiments at IUAC. I am also grateful to Dr. G S Lodha, Dr. M H Modi and R K Gupta of RRCAT without whose support the work presented here might not have been possible.

I cannot be thankful enough to Physical Research Laboratory for giving me the opportunity to pursue my dreams of doing PhD. My thanks to all the members of PRL family for gifting me the wonderful years of my PhD tenure. I am grateful to our Director, Prof. J N Goswami and Dean Prof. Utpal Sarkar for their support. I must thank the academic committee for reviewing my research work. A warm thanks to all the members of Space and Atmospheric Sciences Division and Molecular and Laser Physics Group for attending my seminars and giving valuable suggestions.

The construction of the experimental set-up would not have been possible without the support from PRL workshop. I owe heartfelt appreciation to Girish Ubale, Vishnubhai Patel, Rajeshkumar Kaila, and Vipul Patel for their help. I also acknowledge the timely support from Space Application Center in building the experimental set-up. I am thankful to all the staff members of PRL computer center, library, administration and dispensary for the crucial support that they have provided. Thanks to all the canteen staffs for taking care of daily needs.

My friends, Abhishek, Amrendra, Arun, Chinmay, Siddhartha, Sunil, Susanta, Vema and Yogita, shared my frustrations and joys. They provided me with a homely atmosphere away from home. I cannot thank them enough and I will always cherish the moments I spent with them. I thank Arko and Abhishek for the amazing time we had experimenting on culinary skills. I am thankful to Diganta, Fazlul, Sashi, Tanmay, Monojit and Nigam for their company.

I could not have began this journey without the support of my family. I thank my sister and brother in law for their help. A special thanks to my niece, Anwasha, for giving me so much joy. Words cannot express my gratitude for my parents. I have always had their support and blessings for all my endeavours. Their words of encouragement has always been the guiding light in my life.

Abstract

This thesis is concerned with the study of molecular fragmentation due to various electron loss and decay mechanisms. Molecules are quantum mechanical systems in which the electrons and nuclei are in a dynamic equilibrium. Loss of electrons through ionization due to perturbation such as charged particle impact or photoabsorption, disturbs the equilibrium of the molecular system. The perturbation may excite the molecule electronically, vibrationally, rotationally or a combination of these. The excited state attained by the molecule depends on the energy gained from the perturbation. The configuration of the electrons and nuclei in the excited molecular ion is completely different from that of the molecule in the ground state, hence the ground state equilibrium of the molecule may not be maintained. De-excitation inevitably follows, often leading to dissociation of the molecule.

The energy supplied to a molecule upon projectile impact is shared among its electronic and nuclear degrees of freedom. Since there is a priori no fixed pattern in which the energy transferred to the molecule is shared between the electrons and nuclei, the question that immediately arise is, will this energy sharing affect the kinematics of dissociation? And if so, how? What kind of kinematical differences are induced due to various energy sharing mechanisms? To address these questions, the fragmentation of molecules is studied in the light of the kinematical differences between various electron loss and decay processes. Systematic analysis of the electron decay mechanisms and their subsequent effect on the kinematics of molecular dissociation, has been carried out and presented in this thesis. Manifestations of the kinematical differences may be changes in

fragmentation pathways, kinetic energy release upon dissociation and the conformation of the transient molecular ion, corresponding to different energy sharings.

The studies are limited to simple di- and tri-atomic molecules such as CO, OCS and CS₂. Analysis of the fragmentation processes for valence and core ionized molecules is carried out.

Keywords : Shell selective excitation, Auger decay, Molecular fragmentation, Electron spectroscopy, Ion momentum spectroscopy.

List of Publications

1. Ion-induced triple fragmentation of CO_2^{3+} into $\text{C}^+ + \text{O}^+ + \text{O}^+$,
M. R. Jana, P. N. Ghosh, B. Bapat, R. K. Kushawaha, **K. Saha**, I. A. Prajapati, and C. P. Safvan, *Phys. Rev. A*, **84**, 062715, (2011).
2. A combined electron-ion spectrometer for studying complete kinematics of molecular dissociation upon shell selective ionization,
K. Saha, S. B. Banerjee, and B. Bapat, *Rev. Sci. Instrum.*, **84**, 073101 (2013).
3. Three body dissociation of CS_2^{2+} subsequent to various $\text{S}(2p)$ Auger transitions,
K. Saha, S. B. Banerjee, and B. Bapat, *J. Chem. Phys.*, **139**, 164309 (2013).
4. Dissociation of OCS upon various $\text{S}(2p)$ Auger decay transitions,
K. Saha, S. B. Banerjee, and B. Bapat, *J. Phys. Conf. Ser.*, (in press).
5. State selective fragmentation kinematics of OCS^{2+} following $\text{S}(2p)$ Auger decay,
K. Saha, S. B. Banerjee, and B. Bapat, (under preparation).

Acronyms and Abbreviations

CCD	Charged Couple Device
CEM	Channel Electron Multiplier
CFD	Constant Fraction Discriminator
CMA	Cylindrical Mirror Analyzer
COLTRIMS	Cold Target Recoil Ion Momentum Spectroscopy
DLD	Delay Line Detector
FWHM	Full Width Half Maximum
KER	Kinetic Energy Release
LCAO	Linear Combination of Atomic Orbitals
MCP	Micro Channel Plate
MCS	Multi Channel Scalar
PEC	Potential Energy Curve
PES	Potential Energy Surface
RIMS	Recoil Ion Momentum Spectroscopy
TDC	Time to Digital Convertor
TGM	Toroidal Grating Monochromator
ToF	Time of Flight
VMI	Velocity Map Imaging

List of Tables

2.1	Schematic of a typical list mode data file	27
4.1	KER values (in eV) for different dissociation channels of OCS^{2+} .	92
4.2	KER values (in eV) for different dissociation channels of CS_2^{2+} . .	95

List of Figures

1.1	A typical potential energy curve of a diatomic molecule.	4
1.2	Molecular orbitals of N ₂	7
1.3	Schematic of the Auger decay process.	11
1.4	Molecular potential energy curves depicting excitation to a purely repulsive state.	13
2.1	Schematic representation of CMA.	19
2.2	Illustration of the working principle of ion momentum spectroscopy.	22
2.3	Schematic of a typical double field ion momentum spectrometer. .	23
2.4	Schematic representation of multi-particle coincidence detection. .	26
2.5	Schematic of the combined electron ion spectrometer.	28
2.6	The normalized angular density distribution ($\rho(\theta)/\rho(0)$) of gas jet.	30
2.7	Simulated trajectory of electrons through the CMA.	33
2.8	Simulated trajectories of ions through the ion momentum spectrometer.	35
2.9	Schematic representation of a CEM.	36
2.10	Schematic representation of a MCP.	38
2.11	Schematic of the arrangement of two MCPs stacked together along with a delay line anode depicting the principle of position encoding.	39
2.12	Data acquisition scheme.	41
3.1	Electron spectra of Helium for different photon energies.	46
3.2	CMA calibration curve.	47
3.3	Electron spectrum of Argon at 155 eV photon energy.	48

3.4	Time of flight spectrum of Argon corresponding to ionization of $3p$ shell by 155 eV photons.	52
3.5	Ion-ion coincidence map between Hit1 and Hit2 upon dissociation of CO_2 due to photoionization by 155 eV photons.	54
3.6	Newton diagram for three body break-up of CO_2 via $\text{C}^+:\text{O}^+:\text{O}$ channel.	57
3.7	Molecular potential energy curves depicting KER of a molecule AB dissociating to A^+ and B^+	58
3.8	The KER distribution upon fragmentation of CO_2 into O^+ and CO^+	59
3.9	Characteristic momentum vector geometry of a triatomic transient molecular ion in Dalitz plot.	61
4.1	Electron spectrum of CO at 155 eV photon energy.	65
4.2	Time of flight spectrum of CO corresponding to different electron energies.	66
4.3	Ion-ion coincidence map showing $\text{C}^+:\text{O}^+$ island.	68
4.4	Broad features of the $\text{S}(2p)$ Auger electron spectrum of OCS	72
4.5	Time of flight spectra of OCS corresponding to different $\text{S}(2p)$ Auger decay states of the molecule.	73
4.6	Ion-ion coincidence map of OCS corresponding to different Auger decay states.	75
4.7	Broad features of the $\text{S}(2p)$ Auger electron spectrum of CS_2	78
4.8	Time of flight spectra of CS_2 corresponding to different $\text{S}(2p)$ Auger decay states.	79
4.9	Ion-ion coincidence map of CS_2 corresponding to different final Auger states	80
4.10	Newton diagram of $\text{C}^+:\text{S}^+:\text{O}$ fragmentation channel for $(3h - 1p)$ Auger state.	85
4.11	Newton diagram of $\text{C}^+:\text{O}^+:\text{S}$ fragmentation channel for $(3h - 1p)$ Auger state.	86

4.12	Newton diagram of O^+S^+C fragmentation channel for $(3h - 1p)$ Auger state.	87
4.13	Newton diagram of C^+S^+S fragmentation channel for $(3h - 1p)$ Auger state.	88
4.14	Newton diagram of S^+S^+C fragmentation channel for $(3h - 1p)$ Auger state.	89
4.15	Kinetic energy release (KER) distribution for various fragmenta- tion channels of OCS^{2+} corresponding to different final Auger states.	91
4.16	Kinetic Energy Release (KER) distribution of various fragmenta- tion channels of CS_2^{2+} corresponding to different final Auger states.	94
4.17	Dalitz plots for various dissociation channels of CS_2^{2+} precursor ion.	97
4.18	Dalitz plot of C^+S^+S fragmentation channel for different KER range.	98
4.19	Dalitz plot of S^+S^+C fragmentation channel for different KER range.	99

Chapter 1

Introduction

The internal structure and properties of matter have always captivated human imagination. The idea that matter is made up of indivisible identical entities is perhaps one of the greatest realizations of human civilization. This indivisible unit of matter was named “atomos” by Democritus around 450 BC, from which the term “atom” is derived. It was not until the early 19th century that studies suggesting the existence of atoms came into light. Based on earlier studies by Antoine Lavoisier (law of conservation of mass) and Joseph Louis Proust (law of definite proportions), John Dalton proposed that chemicals are composed of unique indivisible entities which combine to form compounds in such a way that their ratio is a small whole number [1]. Dalton’s atomic theory in effect gives us the first hints to how a molecule is formed from atoms. The concept of indivisibility of the atom remained unquestioned until the discovery of the electron by Joseph John Thomson in 1897 [2]. His discovery suggested that the atom was divisible and thus must have an internal structure. Later, in 1911, scattering experiments conducted by Ernest Rutherford revealed that most of the atomic mass is concentrated in a small volume of positively charged nucleus, while the negatively charged electrons revolve around the nucleus and constitute most of the volume of the atom [3].

The next phase in the understanding the atom came along with the development of quantum mechanics. Neils Bohr, in 1913, proposed an atomic model

where the electrons only occupy certain stationary orbits around the nucleus having discrete energy and size [4]. Following this, pioneering works by Wolfgang Pauli (exclusion principle) [5], Erwin Schrödinger (wave mechanics) [6–9] and many others, helped to develop the quantum mechanical framework of the atom. The modern view of atoms or molecules is a quantum mechanical one in which the discrete orbit idea is replaced by a probabilistic picture. The electrons which surround the nucleus in certain atomic orbitals are represented by wavefunctions that have definite quantum numbers. A molecule too is thought to have discrete orbitals, and often understood as being a mixture of atomic orbitals. The static structure and properties of atoms and molecules have been studied extensively in the past century. A wealth of information such as binding energy, electronic energy levels, dipole moment etc. is available to us for almost every atom and molecule [10]. The situation is quite different when we address the time evolution of the atoms or molecules under the influence of an external perturbation. The difficulty in studying the dynamics of such systems lies in the fact that apart from being a many body problem (which is also the case for static system), the influence of the perturbation on each of the constituents of atom or molecule is to be taken into account. Furthermore, in the case of ionizing perturbation, the loss of electrons results in a change in the number of particles describing the system. The electron–electron as well as the electron–nuclear interaction of the perturbed atom or molecule changes drastically from the static situation. The study of the dynamics of the perturbed molecule is much more complex than that of an atom. The complexity arises due to greater degrees of freedom of a molecule which are needed to be tracked in order to extract its dynamical properties. This thesis, attempts to study molecular systems which are perturbed due to ionization, by tracking and selecting some degrees of freedom, thereby giving a deeper insight into the dynamics of dissociation of molecular ions.

1.1 The Molecular Structure

We begin by an overview of the theoretical description of a molecule. In the quantum mechanical description, a molecule can be represented by a wavefunction Ψ ,

and the solution of the Schrödinger equation of the molecular Hamiltonian yields complete information of the molecular system. The Schrödinger equation of a molecule is given by

$$\mathbf{H}\Psi = \mathbf{E}\Psi \quad (1.1)$$

where \mathbf{H} is the Hamiltonian operator and \mathbf{E} is the total energy of the system. The molecular Hamiltonian can be written as,

$$\mathbf{H} = \underbrace{-\frac{\hbar^2}{2} \sum_{\alpha} \frac{1}{m_{\alpha}} \nabla_{\alpha}^2}_{T_N} - \underbrace{\frac{\hbar^2}{2m_e} \sum_i \nabla_i^2}_{T_e} + \underbrace{\sum_{\alpha} \sum_{\beta > \alpha} \frac{Z_{\alpha} Z_{\beta} e^2}{r_{\alpha\beta}} - \sum_{\alpha} \sum_i \frac{Z_{\alpha} e^2}{r_{i\alpha}} + \sum_j \sum_{i > j} \frac{e^2}{r_{ij}}}_V \quad (1.2)$$

α and β refer to nuclei while i and j refer to electrons. m_{α} and m_e represents mass of nucleus and electron respectively. r denotes distance, Z is atomic number and e is electronic charge. T_N and T_e are the kinetic energy operators of the nuclei and the electrons respectively, while V represents the potential energy operator of the system.

Solving the Schrödinger equation for a many particle system such as a molecule is a daunting task, hence various approximations are made to simplify the situation. The Born-Oppenheimer approximation [11–14] is one of them. It exploits the fact that the nucleus is much heavier than the electrons, hence the electronic motion is much faster than nuclear motion. To a good approximation, as far as the electrons are concerned, the nuclei can be regarded as fixed in space during electronic motion. Following this approximation, the molecular wavefunction Ψ can be divided into electronic (ψ_e) and nuclear (ψ_N) parts and can be solved separately, thus simplifying the problem. The electronic Schrödinger equation taking into account the nuclear repulsion for a fixed nuclear configuration is written as,

$$(H_e + V_{NN})\psi_e = U\psi_e \quad (1.3)$$

where, $H_e = -\frac{\hbar^2}{2m_e} \sum_i \nabla_i^2 - \sum_\alpha \sum_i \frac{Z_\alpha e^2}{r_{i\alpha}} + \sum_j \sum_{i>j} \frac{e^2}{r_{ij}}$, is the electronic Hamiltonian, $V_{NN} = \sum_\alpha \sum_{\beta>\alpha} \frac{Z_\alpha Z_\beta e^2}{r_{\alpha\beta}}$, is the nuclear repulsion term and $U = E_e + V_{NN}$ is the total energy which includes electronic energy (E_e) along with the internuclear repulsion (V_{NN}). Equation 1.3 can be solved relatively easily because the electronic wavefunction and energy only has parametrical dependence on the nuclear configuration. With the change in the nuclear configuration (when the motion of the nuclei is taken into account), the solution of the equation changes hence yielding different values of U . Thus, as the nuclei move, the electronic energy can be considered to vary as a function of the parameters defining the nuclear configuration and U then represents the potential energy of the entire system. The variation of this potential energy as a function of the nuclear degrees of freedom gives the potential energy curve (PEC) of diatomic molecules or in general the potential energy surface (PES) for polyatomic molecules. The equilibrium conformation of the molecule is the one which corresponds to the minimum potential energy of this curve (or surface). A typical potential energy curve of a diatomic molecule is shown in Fig. 1.1.

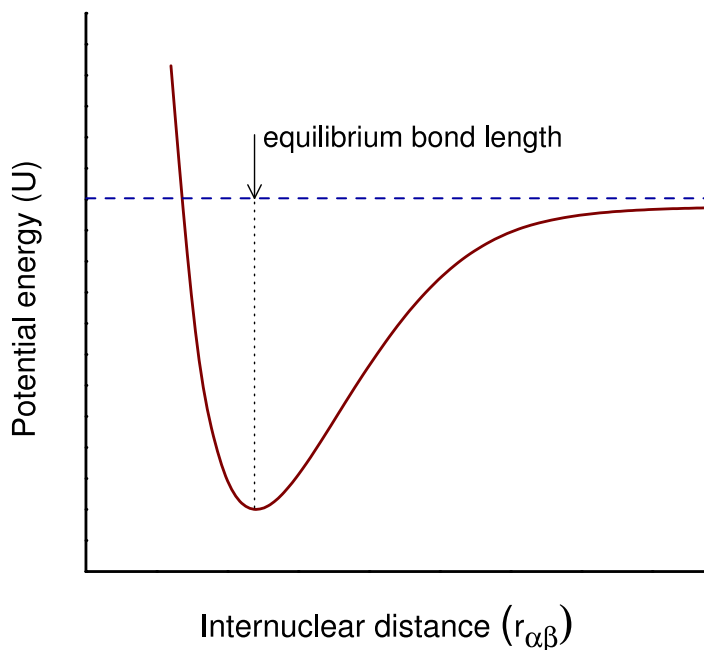


Figure 1.1: A typical potential energy curve of a diatomic molecule.

The total energy of the molecular system can be calculated by solving the nuclear Schrödinger equation,

$$H_N \psi_N = \mathbf{E} \psi_N \quad (1.4)$$

where the Hamiltonian is given by, $H_N = -\frac{\hbar^2}{2} \sum_{\alpha} \frac{1}{m_{\alpha}} \nabla_{\alpha}^2 + U$. Here \mathbf{E} gives the total energy of the molecule since the Hamiltonian includes operators of both nuclear energy and electronic energy.

The next task is to define the molecular wavefunction itself, particularly the electronic part of the wavefunction (ψ_e). A simple approximation can be made in the construction of ψ_e , that they are composed of the wavefunctions of the atoms that form the molecule. Such an assumption is valid in the sense that at large internuclear distance the atoms must retain their own wavefunctions independent of the other atoms constituting the molecule. Thus, the molecular electronic wavefunction can be represented by a linear combination of atomic orbitals (LCAO) *i.e.*,

$$\psi_e = \sum_p c_p \phi_p \quad (1.5)$$

where, ϕ_p are the atomic orbitals and c_p are constants. In principle an infinite number of atomic orbitals (*i.e.* $p = \infty$) are required to create a molecular orbital, but in practice only a finite number of orbitals are used for this purpose. If for simplicity only two atomic orbitals are used, equation 1.5 then becomes,

$$\psi_e = c_a \phi_a + c_b \phi_b \quad (1.6)$$

ϕ_a and ϕ_b are the two atomic orbitals and c_a , c_b are the respective coefficients. Solving this equation for c_a and c_b using variational principle, it can be shown [13, 14] that there are two solutions,

$$\psi_{e1} = C[\phi_a + \phi_b] \quad \text{and} \quad \psi_{e2} = C[\phi_a - \phi_b] \quad (1.7)$$

where C is the normalization constant. Of the two solutions, ψ_{e1} , yields lower energy and is called the bonding molecular orbital while, ψ_{e2} , is higher in energy and is the antibonding molecular orbital. It should be noted here that ψ_e represents only the spatial part of the electronic wavefunction. To get the complete wavefunction of an electron in a molecule, the spin part also needs to be included. For each spatial wavefunction (ψ_e) two different spin configurations, spin up and spin down, are possible which if represented by χ_u and χ_d respectively will yield the complete electronic wavefunction Φ_e as,

$$\Phi_e = \psi_e \chi_u \quad \text{or} \quad \Phi_e = \psi_e \chi_d \quad (1.8)$$

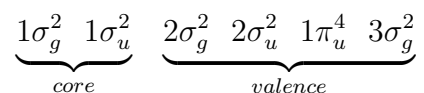
depending on the electronic spin.

Just as the atomic orbitals are named s, p, d, f, \dots depending on the orbital quantum number, the molecular orbitals are named depending on the modulus of the projection of the total angular momentum (m_z) along the internuclear axis. For $|m_z| = 0, 1, 2, \dots$ molecular orbitals are named $\sigma, \pi, \delta, \dots$ etc. Some distinction is also made depending on symmetry of the orbital. Spatially symmetric orbital wavefunctions are called gerade while antisymmetric ones are called ungerade and are denoted by “g” or “u” subscript respectively (*e.g.* σ_g, σ_u). These molecular orbitals are filled according to Pauli’s exclusion principle to give the electronic configuration of the molecule. The quantum mechanical state of the molecule itself can be represented by a term symbol given by,

$${}^{2S+1}\Lambda_{(g/u)}^{(+/-)}$$

Λ is the modulus of the projection of total electronic orbital angular momentum along the internuclear axis. For $\Lambda = 0, 1, 2, \dots$ the term symbol is denoted by $\Sigma, \Pi, \Delta, \dots$ etc. S is the total electronic spin quantum number and $2S + 1$ denotes the multiplicity, while (g/u) signifies parity and $(+/-)$ denotes whether

the molecule is symmetric (+) upon reflection along any plane containing the internuclear axis or asymmetric (-). For example, the ground state electronic configuration of the most abundant molecule in the atmosphere, N_2 , can be written as,



where, the core and valence orbitals are shown within braces. It follows that the molecular term symbol of N_2 will be $^1\Sigma_g^+$. A pictorial representation of the molecular orbital structure of N_2 is shown in Fig. 1.2.

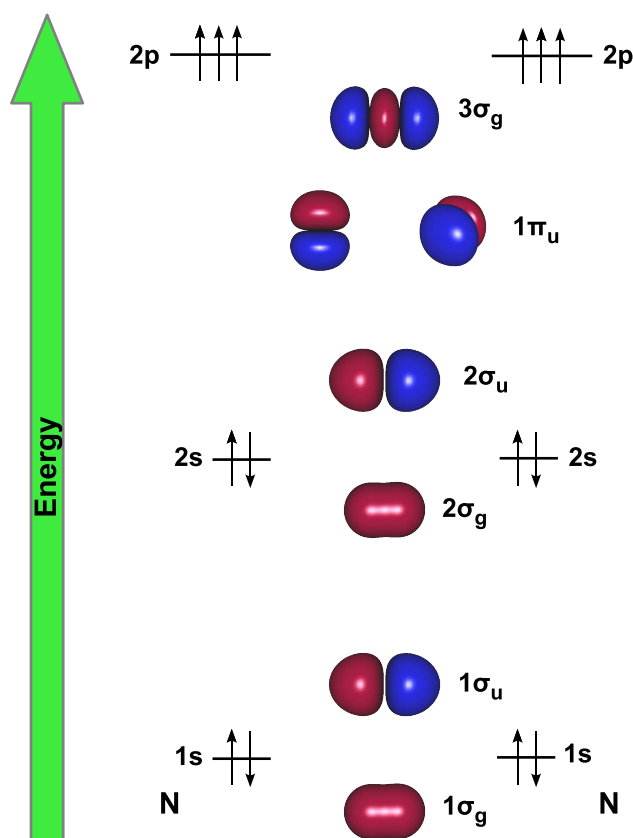


Figure 1.2: Molecular orbitals of N_2 .

1.2 The Perturbed Molecule

A molecule can be perturbed by particle impact or by absorption of radiation. The type of excitation process that the molecule is subjected to depends on the energy gained by the molecule due to the perturbation. As a consequence, the molecule can undergo excitation with no electron loss but minor nuclear rearrangement (vibrational or rotational excitation of molecule), excitation with no electron loss but separation of nuclei (dissociation), excitation with electron loss (ionization), excitation with electron loss and nuclear separation (dissociative ionization). A molecule is excited vibrationally or rotationally when the energy supplied by the perturbation is comparable to the vibrational or rotational quantum spacings, which correspond to purely nuclear degrees of freedom of the molecule. In this case, the molecule remains in the potential well shown in Fig. 1.1 but is excited to higher vibrational or rotational levels. Dissociation occurs when the perturbing energy is sufficiently high enough such that molecular bonds are broken. The process may be viewed as the reverse mechanism to molecule formation where the atoms come together to create a molecule via bond formation. For dissociation to occur, the perturbation must supply enough energy to the molecule required to come out of the potential well. Once the molecule is out of the potential well it is no longer a bound system and the atoms can separate from each other. When the energy transferred to the molecule is greater than the separation of the electronic energy levels, the Born-Oppenheimer approximation allows us to treat the perturbation as electronic excitation followed by nuclear rearrangement. In our study, we focus on ionization where the perturbation causes electron loss from the molecule and ionization induced dissociation of molecule or dissociative ionization.

1.2.1 Ionization

The process by which electrons are ejected from or captured in an atom or molecule is called ionization. For our case, only ionizations producing positively charged species due to loss of electrons are relevant. Ionization of an atom or

molecule occurs due to an external perturbation usually in the form of projectile impact. The projectile can be photon, electron or ion, and depending on parameters such as their energy, charge state (for ions) etc. it may produce singly or multiply charged species. In this discussion only photon impact ionization of molecules will be considered, which is the process studied in the course of this work.

When a molecule is irradiated with photons, the electron absorbs the photon energy. If the photon energy is more than the binding energy of the electron, the electron breaks free from the molecular potential thus ionization occurs. The probability that electron in a certain orbital will be ionized upon photoabsorption is given by the Fermi Golden Rule,

$$P = \frac{2\pi}{\hbar} |M_{fi}|^2 \rho \quad (1.9)$$

where, P gives the probability of the transition of the electron from its bound state to continuum. $|M_{fi}| = \int \phi_f^* H' \phi_i d\tau$, is the transition matrix element for the perturbation H' between final and initial state of the system given by ϕ_f and ϕ_i respectively. ρ gives the density of final states. Higher the value of P , more is the likelihood of the transition, which is the case when the photon energy matches the difference between the energy levels of the ground and excited state, or matches the binding energy in case of ionization. Certain selection rules can be derived based on equation 1.9, which gives the information about whether a transition is favourable or not [15, 16].

The energy of the photon plays a crucial role in photoionization process. The Fermi golden rule shows that there is an energy selectivity in the case of excitation by photons, so by selecting the photon energy it is possible to bring about preferential ionization of the valence and core orbitals. In the case of valence ionization, electron from a valence molecular orbital is emitted with a kinetic energy,

$$E_{pe} = E_P - BE \quad (1.10)$$

where, E_P is the photon energy and BE is the binding energy of the orbital. This electron is called the photoelectron and by measuring its energy (E_{pe}) the binding energy of the valence orbital can be calculated if photon energy is known, thereby revealing the identity of the valence orbital which has been ionized.

The situation is quite different when a core orbital of a molecule is ionized. The core orbitals of a molecule is formed out of the core orbitals of constituent atoms. But there is a binding energy difference in the core orbital of an isolated atom and the core orbital of the atom in a molecule. This difference arises due the weak bonding between the core orbitals of different atoms in a molecule. Nevertheless, the core orbital may be considered to be by and large localized at the corresponding atomic sites. Upon ionization, electron from the core orbital is ejected with an energy E_{pe} (see equation 1.10) and a vacancy is created in the core orbital. This triggers an electronic decay process wherein a valence electron fills the core vacancy. The excess energy due to this electronic decay can be expelled by two different mechanisms. First, by emission of photons producing characteristic X-rays which have definite energy determined by the binding energy of the core and valence orbitals. The second mechanism is via the ejection of a valence electron which takes up the excess energy. This electron is called the Auger electron, and the process Auger decay, named after Pierre Auger, who discovered it in 1923 [17]. Auger decay is a double ionization process which involves ejection of a core electron and a valence electron (called the photoelectron and the Auger electron, respectively, when they are in the continuum) with the production of two holes in the valence orbitals as shown in the schematic in Fig. 1.3.

Just as in the case of photon emission, X-rays are of specific energy, Auger electrons also have definite kinetic energy given by,

$$E_{auger} = BE_C - BE_{V_i} - BE_{V_f} \quad (1.11)$$

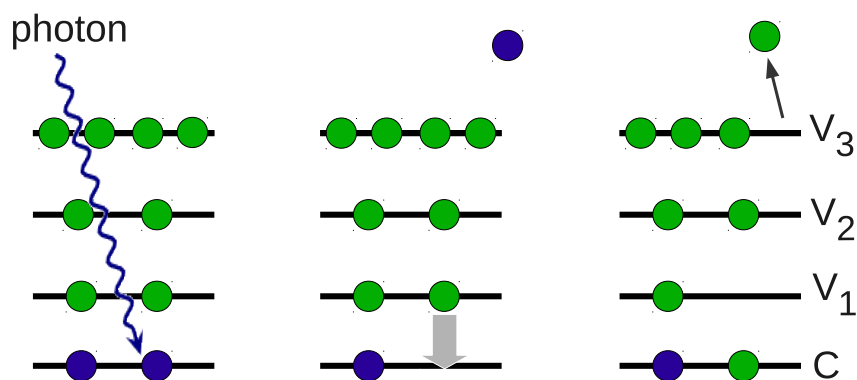


Figure 1.3: Schematic of the Auger decay process. C denotes the core orbital while the V's represent valence orbitals.

where, BE_C , BE_{V_i} and BE_{V_f} denotes the binding energy of, the core orbital, the valence orbital from which the electron fills the core vacancy and the valence orbital from which the Auger electron is ejected, respectively. As it is evident, the Auger electron energy (E_{auger}) is independent of the photon energy and is characteristic of the orbitals that take part in Auger decay. Usually, a particular core ionization may be followed by decay from various valence orbitals, giving rise to Auger electrons of different energies, each corresponding to unique combination of valence orbitals that are involved in the decay mechanism. Thus, the kinetic energy of the Auger electron indicates which valence orbitals are participating in the ionization process. In effect, the kinetic energy of the Auger electrons carries the information about the final electronic configuration of the molecular ion that is formed upon core ionization. This feature of the Auger decay is the key to the selectivity in the excitation of a molecule that we have investigated in the course of this work.

It is to be noted that though valence and core ionization processes have been discussed here for photon impact only, these ionizations are equally possible in the case of electron or ion impact. But, unlike photoionization, the exact amount

of energy taken up by the molecular electron upon ion or electron impact is uncertain due to the range of impact parameters involved. Thus it is extremely difficult to control or estimate a priori the energy transfer to a molecule subject to charged particle impact. Hence the energy selectivity offered by photons is missing, and it becomes difficult, though not impossible, to track the excitation through the energy of the ejected electrons..

1.2.2 Dissociative Ionization

Dissociative ionization, as the name suggests is the process of molecular dissociation induced by ionization. In the ground state configuration of a molecule the electrons and nuclei are in a dynamic equilibrium. Loss of electrons through ionization disturbs the equilibrium of the molecular system. Dissociation of the molecule occurs when it is excited into such an electron-nuclei configuration that the minimum of the potential energy is only attained when the nuclei are far apart, free from any mutual interactions. As a result, the molecular bonds are broken and the molecule separates either partially or completely into its atomic constituents which may be singly or multiply charged. Due to the differing time scales of electronic and nuclear motions, this process can be regarded to be occurring in two steps. In the first step, ionization leads to the loss of electrons within a timescale of femtoseconds. Next, dissociation occur yielding various ionic species within a period of about picoseconds. Thus, when the molecule undergoes transition from the neutral ground state to the charge excited state due to ionization, the nuclei are assumed to be static as the electronic motion is much faster than nuclear motion. Hence only vertical transitions occur between the potential energy curve (or surface) of the ground state of molecule and the excited state. This is known as Frank Condon principle.

Energetics play an important role in molecular fragmentation. To elucidate this, let us consider the case where molecule is excited by photoionization. In photoionization the photon energy is shared between the ejected electrons and the residual molecular ion. The energy gained by the molecular ion through

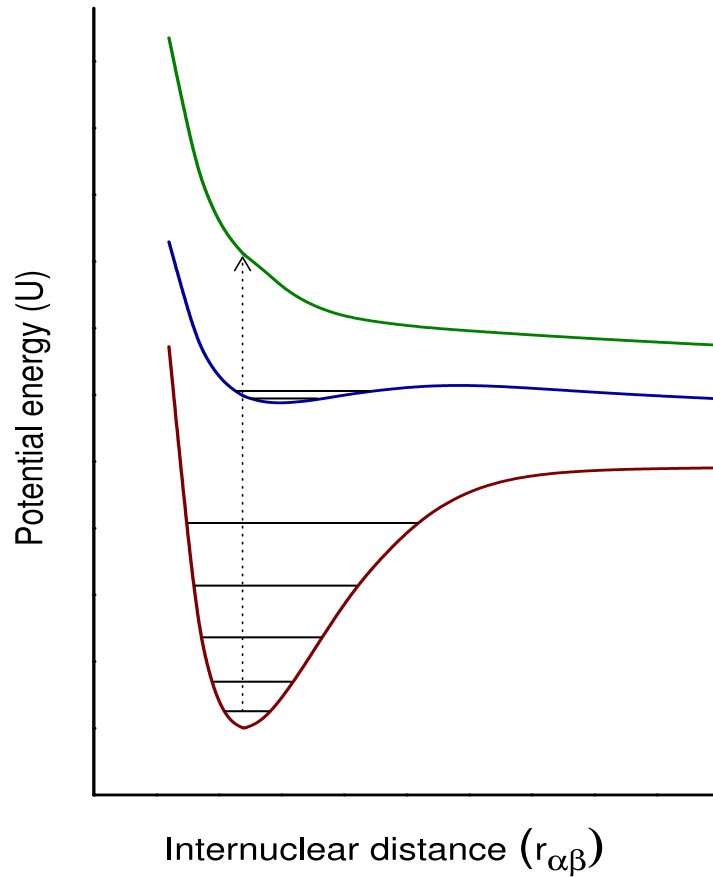


Figure 1.4: Molecular potential energy curves depicting excitation to a purely repulsive state. Red curve denotes ground state, blue curve denotes stable excited state while green curve denotes dissociative state PEC of the molecule. Horizontal lines mark the vibrational levels.

ionization is called excitation energy and is given by,

$$E_{exi} = E_P - E_{elec} \quad (1.12)$$

where, E_P is the photon energy and E_{elec} represents the kinetic energy of all the ejected electrons. The excitation energy (E_{exi}) which is distributed among the internal degrees of freedom of the molecular ion is a vital parameter that governs which excited state the molecule will be promoted to upon ionization. The excited state potential energy structure may be bound in nature, in which case the molecular ion does not dissociate. In general, for a particular charge state, the bound potential energy states of stable molecular ion are lower in energy than of the dissociative states. When the excitation energy is sufficiently high, the molecular ion is excited into a state which has a repulsive potential energy curve

(see Fig. 1.4) thus dissociation occurs producing fragment ions. Fragmentation processes are highly dependent on the nature of the potential energy curve of the excited molecular ion state and the fragment ions bear the signature of this. In dissociative ionization a variety of excited states of the molecular ion are accessed yielding fragment ions with a wide gamut of kinematic properties.

1.3 Thesis Overview

The formation and dissociation of molecular ions under the impact of various projectiles has been an active area of research for several decades [18, 19]. Observation of the time evolution of the transient molecular ion yields the dynamics of the dissociation. However, in an experiment we can only determine the kinematics of the system in the asymptotic limit *i.e.* when the fragments due to dissociation are free from the Coulomb field of each other. Kinematically complete analysis of molecular dissociation is an important step towards understanding the dynamics of the process. Knowledge of the correlated kinematics of the fragments upon molecular dissociation enables us to gain valuable insights about parameters such as the angular distributions and the kinetic energy distributions of the fragments, and thereby obtain the properties of the excited precursor molecular ion states in great detail.

Since various transient states are attained depending on the excitation energy supplied to the molecule through ionization, the kinematics of dissociation is expected to depend on the ionization and subsequent electronic decay processes. This work attempts to study the differences in the dissociation mechanisms of molecules for various electron loss mechanisms triggered by selective ionization of a particular molecular orbital.

To carry out these studies, a combined electron ion spectrometer was built which is capable of analyzing both the electrons and ions simultaneous in a dissociation event. The experimental techniques employed for the study is discussed

in Chapter 2. A detailed description of the experimental set-up and the data acquisition technique is also provided in this chapter. From the raw data, information about the kinematics of electrons and fragment ions were extracted using various methods. These data analysis methodology are discussed in Chapter 3. Details about the procedure followed to calibrate the experimental set-up, identify the fragmentation channels, reveal the kinetic energy distribution of the fragment ions and excited state molecular ion geometry is described in this chapter. Chapter 4 concerns with the results that are obtained from our studies. The fate of valence shell ionized CO molecule is discussed. Kinematically complete studies of molecular fragmentation were done for different Auger transitions in sulphur bearing molecules upon ionization of sulphur $2p$ core orbital. Results for OCS and CS₂ are reported in this chapter. The work is summarized and the inferences drawn from our studies is outlined in Chapter 5. This chapter also discusses the future possibilities for further scientific explorations related to the study.

Chapter 2

Experimental Techniques

Probing the kinematical changes in molecular dissociation effected by various ionization mechanisms requires a combination of different experimental techniques. To reveal the ionization mechanism due to projectile impact on a molecule, the electrons emitted from the molecule are needed to be energy analyzed. This can be achieved by electron spectroscopy techniques. On the other hand, to understand fully the fragmentation of molecule brought upon by the ionization process, the fragment ions must not only be identified, but also their kinematical parameters such as their momenta, kinetic energy etc. must be recorded. Ion momentum spectroscopy techniques are used to accomplish this. Thus, for our purpose, these techniques are needed to be applied simultaneously in such a manner that they perform as a compatible unison. The details about these techniques, the experimental set-up and several aspects about the experiments performed are discussed in the following sections of this chapter. The general techniques of electron spectroscopy and ion momentum spectroscopy are presented first. Then the details about the collision system, experimental set-up, associated detectors and data acquisition techniques are presented.

2.1 Electron Spectroscopy

The study of parameters such as the kinetic energy distribution, angular distribution etc. of electrons emitted upon ionization is known as electron spectroscopy. The origins of electron spectroscopy can be traced back to as early as 1887 when Heinrich Hertz observed that metal surfaces irradiated with ultraviolet rays lead to emission of charge from the surface [20]. Following this observation, various experiments were done to study the characteristics of this photoemission [21, 22]. In 1905, Albert Einstein gave the theoretical explanation of the observed photoemission as electrons being emitted from the metal surface upon absorption of photons [23]. The phenomena was called as photoelectric effect. Since then, with the development of technology, various studies have been done which have led to a significant advancement in the field of electron spectroscopy. It has now become a standard tool for investigating various properties of solid targets as well as of individual atoms and molecules [24, 25].

In general, the study of the kinetic energy of emitted electrons is done using analyzers having electric or magnetic fields. The working principle of these analyzers is spatial or temporal dispersion of electrons according to their energy under the influence of the field. Various electron analyzers such as parallel plate analyzer, spherical sector analyzer, Wien filter etc. are used for this purpose [26, 27]. These spectrometers have their own advantages and disadvantages. A cylindrical mirror analyzer (CMA), which is a spatially dispersing analyzer employing a static electric field of cylindrical symmetry, was used in our experiments as an electron spectrometer due to its high luminosity.

2.1.1 Cylindrical Mirror Analyzer

The CMA comprises of two cylinders of different radii having a common axis with the source of electrons at one end and a detector at the other of the axis (see Fig. 2.1). The cylinder with the smaller radius has two slits with a particular distance between them. These act as entrance and exit slits for the incident electrons.

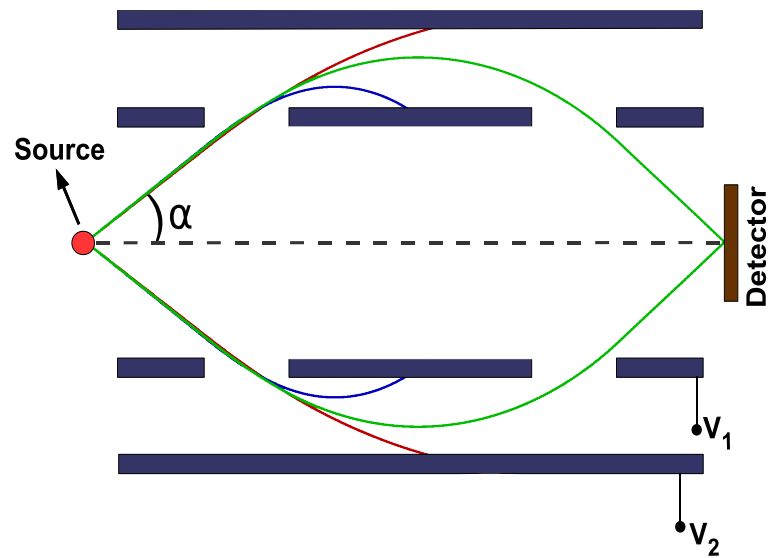


Figure 2.1: Schematic representation of CMA showing trajectories of electrons with different energies. V_1 and V_2 represents the potentials applied in inner and outer cylinder.

Electrons emitted at a certain polar angle (α) enter the cavity between the two cylinders. The two cylinders are maintained at different potentials keeping the outer cylinder always at a negative potential with respect to the inner one. An electrostatic field is generated across the cylinders due to the potential difference. Due to this field electrons experience Coulomb force and only those having an appropriate energy are focussed through the exit slit for detection. Electrons lower or higher in energy hit the inner or the outer cylinder and are lost. This kind of design is advantageous as it provides total azimuthal acceptance and gives a large flux at the detector. Varying the electric field by changing the potentials on the cylinders enable electrons of different energy to pass through the analyzer thus giving it energy selectivity. The energy of detected electrons can be found as the function of the applied potential. Scanning the potential within suitable range and recording the flux at each pass voltage, generates the electron energy spectrum.

The energy resolution of the CMA depends on its geometric parameters. If ΔE is the range of electron energy spread that is admissible through the CMA

when it is set to collect electrons of energy E , the resolution is given by [27],

$$\frac{\Delta E}{E} = C_w \frac{w}{L} + C_\alpha (\Delta\alpha)^2 + C'_\alpha (\Delta\alpha)^3 \quad (2.1)$$

where, w is the slit width and L is the dispersive length *i.e.* the length travelled by the electrons along the CMA axis due its trajectory through the dispersive field. The first term in the right hand side of equation 2.1 represents the linear resolution of the CMA due to energy spread owing to finite slit widths and can be written as,

$$C_w \frac{w}{L} = \frac{2w}{D}$$

where, D gives the dispersion of electrons for a certain geometric configuration of the CMA. The second and the third term gives the energy spread due to the angular deviation ($\Delta\alpha$) of the electron incident on the CMA entrance slit from the ideal entry angle (α). These terms may be written as,

$$C_\alpha (\Delta\alpha)^2 = \frac{\Delta L}{D} \quad \text{and} \quad C'_\alpha (\Delta\alpha)^3 = \frac{2\Delta L}{D}$$

where, ΔL is the variation in the dispersive length (L) due to the angular deviation ($\Delta\alpha$) of the incident electrons. The resolution of the CMA can be improved by changing the geometric parameters, like reducing the slit width (w), but with the increase in resolution there is loss of luminosity. Usually, a compromise is made between the resolution and the luminosity while designing a CMA.

2.2 Ion Momentum Spectroscopy

Ion Momentum Spectroscopy is a technique capable of revealing the kinematical parameters of recoil ions produced in projectile impact ionization of atoms or molecules. Although some studies were reported as early as 1960s [28–31], major advances in the study of the recoil ions happened in the last few decades. In late 1980s studies were done to obtain the mean energy of recoil ions in projectile-atom collisional experiments [32–34]. On the other hand, the momentum distribution of the recoil ions was first measured by Ullrich *et.al.* [35, 36] at about the

same time. The component of ion momenta transverse to the projectile beam direction could be extracted with these experiments. The measurement of complete recoil ion momentum vector was first reported by Ali *et.al.* [37] in ion-atom collisions. Information about all the momentum components with collection over nearly the entire solid angle of the emitted recoil ions was now accessible. This new technique proved to be very effective in measuring the correlated momenta of the fragment ions produced in molecular dissociation and the technique was employed to study kinematics of dissociative ionization of molecules [38–42]. Various developments have occurred and techniques have evolved to study the recoil ions with more precision. In an attempt to improve the resolution of ion momentum, the thermal width of the target momentum was reduced by using precooled supersonic target jets, which is now known as the Cold Target Recoil Ion Momentum Spectroscopy (COLTRIMS) [43–45]. Complete momentum information of electrons emitted in the collision process along with the recoil ions can be obtained using spectrometers which are known as “reaction microscopes” [46–49]. Other than these, techniques like Velocity Map Imaging (VMI) [50–53] are routinely used to reveal the momenta of recoil ions and electrons in collisional experiments involving atomic or molecular ionization. The details about the development, techniques and application of momentum spectroscopy can be found in many comprehensive reviews [54–57].

The principle of ion momentum spectroscopy is as follows. An ensemble of atoms or molecules is ionized by projectile (photon, electron or ion) impact in small interaction volume. It is important for the ensemble to have a small momentum and spatial spread. A homogeneous electric field is generated by applying suitable potentials to meshes which are placed on either side of the interaction volume (see Fig. 2.2). Electrons and ions formed due to ionization are extracted by the electric field in opposite directions to each other. The electrons are detected immediately after extraction while the ions are guided by the extraction field into a field free drift region. The ions then fly through this region without any influence of external fields and get detected by a position

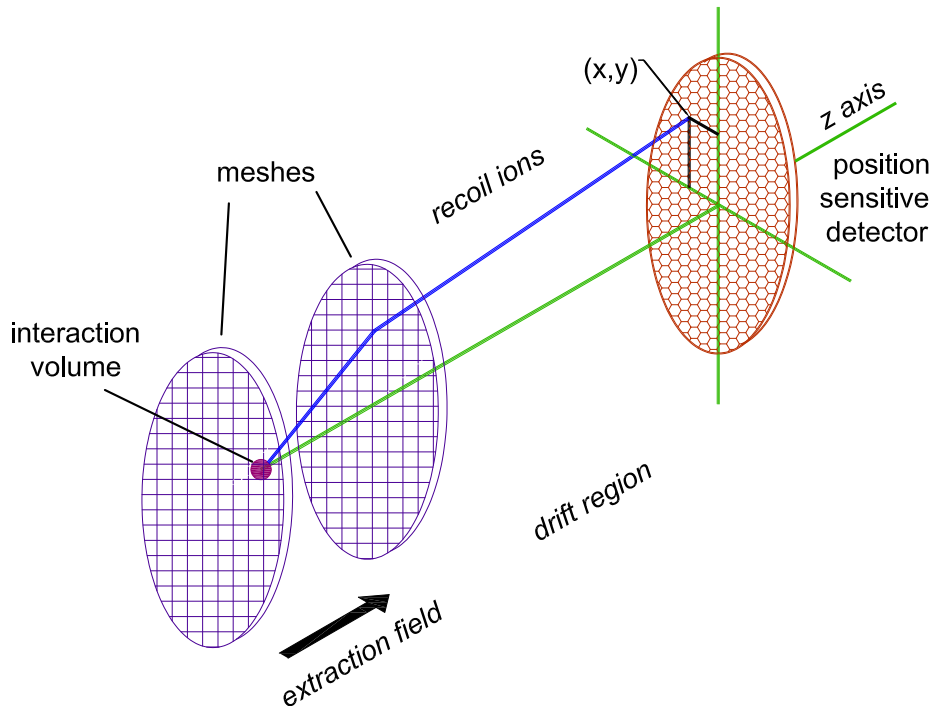


Figure 2.2: Illustration of the working principle of ion momentum spectroscopy.

sensitive detector which is placed at the end of the drift region. Upon detection, the time of flight (ToF) through the spectrometer for each ion and its position (x, y) of impact on detector plane is recorded (provided a trigger corresponding to its birth is available).

2.2.1 Time of flight measurement

The time of flight of ions through the spectrometer depends on the electric field configuration. Though a single extraction field is enough for ToF measurements, in many cases, the ions are accelerated by a secondary homogeneous electric field after extraction and then they are allowed to enter the drift region. In principle, a number of such acceleration fields may be applied after the extraction of ions to improve resolution. The discussion here will be limited to double field configuration since we have employed a double field type spectrometer for our experiments. In double field configuration, the extraction region is followed by a acceleration region where electric fields of appropriate magnitudes are applied while the drift region is kept field free as usual [58]. The schematic diagram of

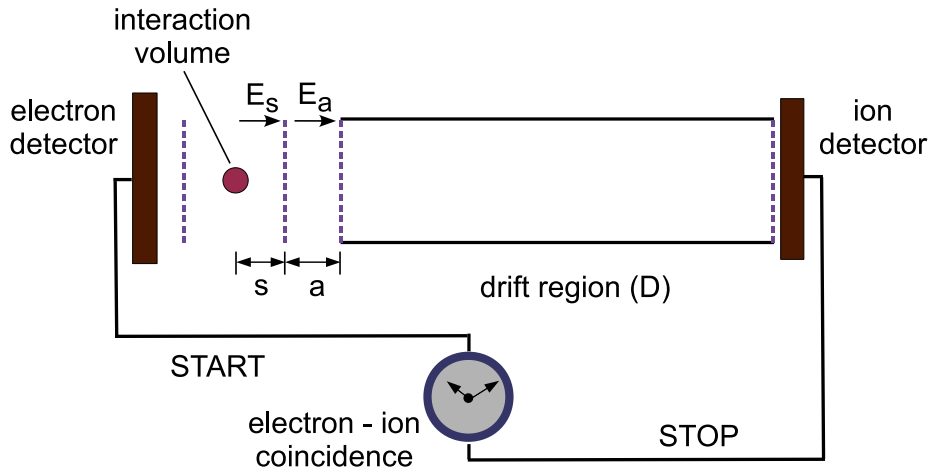


Figure 2.3: Schematic of a typical double field ion momentum spectrometer. Meshes (blue dashed lines) on which suitable potentials are applied to generate homogeneous electric fields also demarcate various regions. The interaction volume, usually formed by the overlap of projectile and target beams, is set in the middle of the extraction region. s and a are the distance the ion has to travel through the extraction region and the acceleration region having electric field E_s and E_a respectively. D is the length of the drift region.

such a spectrometer is given in Fig. 2.3. The ToF is measured taking START from the either electron detection signal or the projectile beam signal if the beam is pulsed. The STOP is marked by the ion detection itself. The ToF of an ion can be derived analytically by considering its flight time through each region in the spectrometer. For an ion of mass m , charge q with a initial velocity v_z along the spectrometer axis, the ToF is given by,

$$t = \frac{-v_z + \sqrt{v_z^2 + 2\frac{qsE_s}{m}}}{\frac{qE_s}{m}} + \frac{-\sqrt{v_z^2 + 2\frac{qsE_s}{m}} + \sqrt{v_z^2 + 2\frac{qsE_s}{m} + 2\frac{qaE_a}{m}}}{\frac{qE_a}{m}} + \frac{D}{\sqrt{v_z^2 + 2\frac{qsE_s}{m} + 2\frac{qaE_a}{m}}} \quad (2.2)$$

where, the first term in right hand side gives the flight time of the ion through the extraction region of length $2s$ and extraction field E_s . The next term is the duration of ion flight through the acceleration region of length a and field E_a . The last term is time of flight of the ion through the drift region of length D . If the ion has no initial velocity equation 2.2 becomes,

$$t_0 = \sqrt{\frac{m}{q}} \left(\frac{\sqrt{2sE_s}}{E_s} + \frac{-\sqrt{2sE_s} + \sqrt{2sE_s + 2aE_a}}{E_a} + \frac{D}{\sqrt{2sE_s + 2aE_a}} \right) \quad (2.3)$$

As evident from equation 2.3, $t_0 \propto \sqrt{m/q}$, where the proportionality constant depends on the known spectrometric parameters. Ions with different mass to charge ratio (m/q) will have characteristic ToFs thus revealing its identity.

The resolution of ToF depends on spatial extent of the interaction volume along the spectrometer axis and the distribution in the initial velocity of the ions. Identical ions produced at different positions within the interaction volume will travel different distances through the accelerating field thus yielding a ToF spread instead of a single valued ToF. On the other hand similar ions produced at the same point in the ionization volume but with different initial velocities will travel the same distance in different flight time durations. Due to these factors, each ionic species will finally yield a ToF distribution instead of a single ToF value and the centroid of the distribution gives the ToF of ions with no initial velocity *i.e.* t_0 . The ToF resolution is given by the ratio $t_0/\Delta t$ where Δt denotes the full width half maximum value of the ToF distribution. Since the mean ToF is proportional to square root of mass, the mass resolution of a spectrometer is given by,

$$\frac{m}{\Delta m} = \frac{1}{2} \frac{t_0}{\Delta t} \quad (2.4)$$

To improve ToF resolution, spectrometers are designed following some focussing conditions. Different focussing conditions are applied to minimize the effect of spatial extent and velocity distribution of ion on their ToF. The space focussing condition which reduces the effect of the spatial spread of the ionization volume on the ion flight time is given by [58],

$$D = 2s\sqrt[3]{k} \left(1 - \frac{1}{k + \sqrt{k}} \frac{a}{s} \right) \quad (2.5)$$

where, $k = (sE_s + aE_a)/sE_s$. A different set of focussing conditions is employed to resolve the effect of initial velocity distribution of ions on their ToFs. These velocity focussing conditions are not relevant in our case since we are interested in measurement of the ion momentum. Infact, it is the spread in the ToF values due to different initial velocities of an ionic species that reveals the distribution of its momentum component along the spectrometer axis.

2.2.2 Evaluation of ion momentum

The ToF information along with the knowledge of the position (x, y) of ion hit on the detector plane is used to derive all the momenta components (p_x, p_y, p_z) of the recoil ions. The ToF alone holds the information about the momentum component along the spectrometer axis (p_z) . From equation 2.2 and 2.3 and considering the fact that the initial velocity of the ions is very small compared to the velocity gained due to the extraction field (E_s) *i.e.* $v_z \ll \sqrt{qsE_s/m}$, we have,

$$\frac{v_z}{m} = qE_s(t_0 - t) \quad (2.6)$$

$$\therefore p_z = qE_s(t_0 - t) \quad (2.7)$$

which gives the momentum component along the spectrometer axis of an ion of mass m , charge q having a ToF t with t_0 being the ToF of an identical ion with zero initial velocity.

The other two component of momentum (p_x and p_y) transverse to the spectrometer axis requires the knowledge of ion hit position (x, y) as well as the ToF (t). These momentum components are given by,

$$\begin{aligned} p_x &= m(x - x_0)/t \\ p_y &= m(y - y_0)/t \end{aligned} \quad (2.8)$$

where, x_0 and y_0 represents the centroid value of the spatial spread of ionization volume projected on the detector plane. The total momentum resolution depends on the ToF resolution as well as the position resolution of the position

sensitive detector. It also greatly depends on the spatial extent of the ionization volume and thermal velocity spread of the target atoms or molecules. Thus a well localized target source, with small spatial and velocity spread, is highly desirable for momentum spectroscopy.

2.2.3 Multi-particle coincidence

An essential aspect in the study of molecular fragmentation kinematics is to gain correlated information of kinematical parameters of all the fragment ions. For this purpose, in each dissociation event, all ionic fragments must be detected in coincidence with the emitted electrons as well as with one other. This is known as multi-particle coincidence. In this technique, the detection of emitted electron in a dissociative ionization event marks the START of a time window which remains open for a certain period of time (in our case $32 \mu\text{s}$). Fragment ions having different m/q arrive at ion detector at different instance and each ion detection marks individual STOP upon which its ToF along with position of hit on the detector is recorded (see Fig. 2.4). Hence this is a common START multiple STOP process. All ionic fragments produced in the dissociation event are detected like this within the stipulated time window. Electron detection from next dissociation event restarts the clock and the process is repeated again. The information about the ionic fragments is thus recorded on an event by event basis

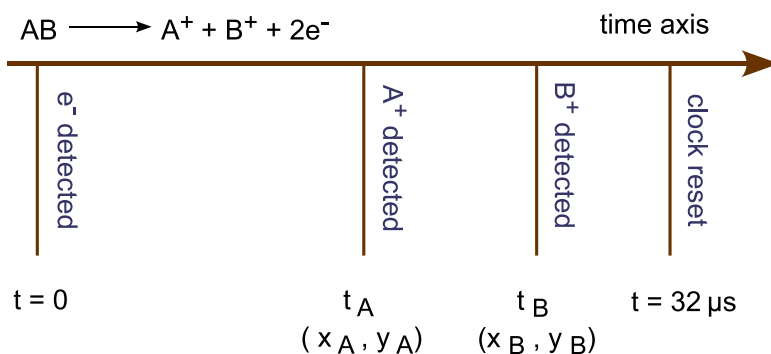


Figure 2.4: Schematic representation of multi-particle coincidence detection of a molecular dissociation event producing ions A^+ and B^+ along with two electrons denoted by e^- .

Event number	Ion 1	Ion 2	Ion 3	Ion 4
...
1001	$(t, x, y)_{1001,1}$	$(t, x, y)_{1001,2}$
1002	$(t, x, y)_{1002,1}$
1003	$(t, x, y)_{1003,1}$	$(t, x, y)_{1003,2}$	$(t, x, y)_{1003,3}$...
1004	$(t, x, y)_{1004,1}$	$(t, x, y)_{1004,2}$
1005	$(t, x, y)_{1005,1}$	$(t, x, y)_{1005,2}$	$(t, x, y)_{1005,3}$	$(t, x, y)_{1005,4}$
...

Table 2.1: Schematic of a typical list mode data file. t represents ToF while (x, y) the ion hit position.

and is stored in a list mode file. The schematic representation of a typical list mode file is given in Table 2.1.

An important requirement in multi-particle coincidence detection is to reject contribution from different dissociations which may lead to spurious coincidence data. This is by and large achieved by satisfying the single collision condition. Under this condition, only one projectile particle is allowed to interact with a single target species at a time. To maintain single collision condition, the rate of incidence is controlled such that average time gap between two ionization events is much larger than the time required for transport of ions to the detector. The clock reset trigger (i.e the next electron detection or next ionizing pulse) should arrive much after the slowest ion has reached the detector, reducing thereby the chances of false coincidences. But false coincidences may still arise due to stray ionizations and is in general present in every coincidence experiment.

If the correlated momenta of all the ions formed due to a molecular dissociation are known, then the momentum of a neutral species produced in the same dissociation event can be evaluated by momentum conservation laws. Since the momentum of the transient molecular ion in the target reference frame is zero so should be the total momenta of all the fragments after dissociation. The mo-

momentum information about the undetectable neutral species can hence be known but is limited to cases where there is only a single neutral fragment in the dissociation process. For multiple neutral species, the momentum of the neutrals cannot be uniquely determined from the momentum balance equation.

2.3 Experimental set-up

An experiment that employs electron energy spectroscopy along with ion detection with full kinetic information will be able to reveal the kinematical changes in fragmentation of molecules triggered by different electron loss mechanisms. We have designed and constructed a spectrometer with these capabilities. The instrument is a combination of a CMA and ion momentum spectrometer coupled axially opposite to each other. The CMA identifies the electronic decay process by analyzing the energy of the ejected electron from a molecule while the ion momentum spectrometer reveals in tandem the corresponding dissociation kinematics by analyzing the fragment ions for their charge state, mass, as well as momentum and detect them in a time ordered sequence. The schematic of the set-up is shown in Fig. 2.5. Description of the set-up is given in the following sections.

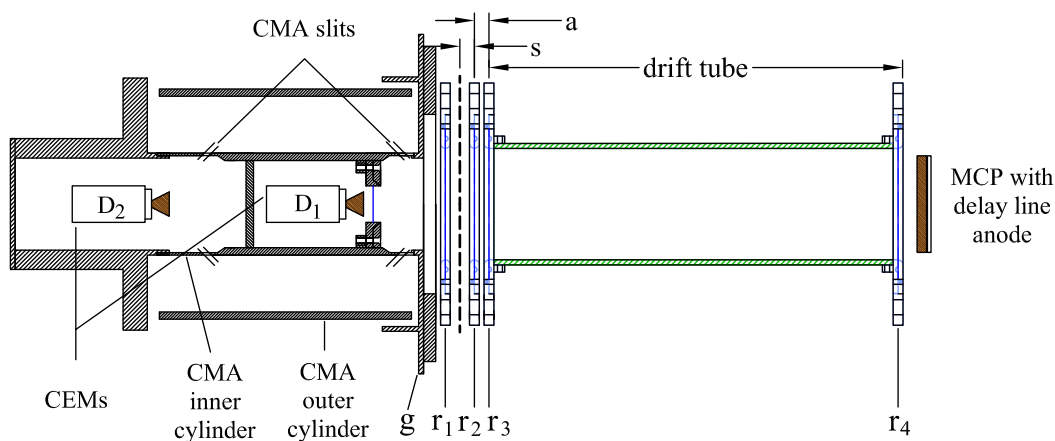


Figure 2.5: Schematic of the combined electron ion spectrometer. The thick dashed line denotes the projectile beam molecular beam plane. Blue lines represents the meshes for generating the extraction fields. D1 and D2 are the electron detectors. See text for details. The slits of the CMA are shown exaggerated for clarity.

2.3.1 Target and excitation source

A primary requirement for this kind of experiments is a collision zone that is well localized in space, and target atoms or molecules that have a narrow spread of kinetic energies so that adequate resolution is ensured. This is by-and-large achieved by a crossed projectile beam and target beam geometry. In our set-up a fine capillary of length 50 mm having an internal diameter of 0.15 mm is used to obtain a effusive beam of the target. A number density of 10^{12} cm^{-3} target molecules is obtained with this arrangement. The target gas beam density profile can be estimated and the spatial extent of the collision zone can be known with the knowledge of the angular density distribution of the gas jet. The density at a point in the gas jet located at a certain distance from the exit plane of the capillary making an angle θ with the capillary axis (*i.e.* half angle of the gas beam spread) is given by [59, 60],

$$\rho(\theta) = \frac{n r^2 j(\theta) \cos^2 \theta}{d^2} \quad (2.9)$$

where, n is the average number density, r is the radius of the capillary and d is the projection of the distance of the point from capillary exit plane along the capillary axis while $j(\theta)$ represents the angular distribution function. When $\tan \theta \geq \gamma$, where $\gamma = 2r/l$, l being the length of the capillary, $j(\theta)$ can be written as,

$$j(\theta) = \xi_0 \cos \theta \left(1 + \frac{2\beta \exp(\delta^2)}{\delta\sqrt{\pi}} \right) \quad (2.10)$$

where, $\delta = \sqrt{\frac{\xi_0^2 l}{(\xi_1 - \xi_0)\lambda \cos \theta}}$, λ being the mean free path of the molecules, and

$$\beta = \int_0^1 \sqrt{1-x^2} \left[\operatorname{erf} \left\{ \delta \left(1 + \frac{\gamma x}{\tan \theta} \left(\frac{\xi_1}{\xi_0} - 1 \right) \right) \right\} - \operatorname{erf}(\delta) \right] dx$$

ξ_0 and ξ_1 are constants whose values are determined to be 0.515γ and 1.223 respectively [59] for $\gamma \rightarrow 0$, as in our case. The density of the gas is maximum along the axis of the capillary *i.e.* when $\theta = 0$. The angular distribution function $j(0)$ in this case is given by,

$$j(0) = \xi_0 + \frac{\sqrt{\pi}}{2} \frac{\xi_0 \exp(\delta^2)}{\delta} \left[\operatorname{erf} \left(\frac{\xi_1}{\xi_0} \delta \right) - \operatorname{erf}(\delta) \right] + \left(\frac{1 - \xi_1}{\xi_0} \right) \exp \left[-\delta^2 \left(\frac{\xi_1}{\xi_0} - 1 \right) \right]$$

The normalized angular density distribution ($\rho(\theta)/\rho(0)$) can thus be obtained and is shown in Fig. 2.6 for our system. The angular extent of the gas jet at full width half maximum value of density was found to be about 20° . Taking the FWHM of the gas density to be the limit where significant number of molecules are present, the spatial spread of the gas jet 3 mm from the capillary exit where the projectile beam crosses it was evaluated to be about 2.2 mm. The spatial extent of the collision zone can be estimated provided the projectile beam width is known. In a crossed target beam projectile beam arrangement, set orthogonal to each other, the spatial extent of the overlap is governed by the beam which has a smaller width, in our case the target gas jet. Thus the collision zone width for our experiments is about 2.2 mm. The knowledge about the collision zone size is important to compute various resolution parameters of the spectrometer.

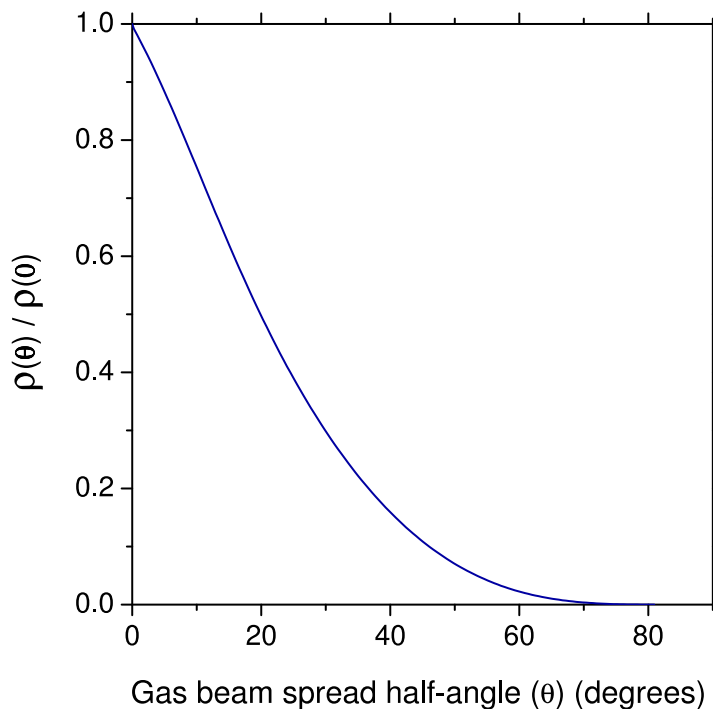


Figure 2.6: The normalized angular density distribution ($\rho(\theta)/\rho(0)$) of gas jet.

As explained earlier, photons are ideal projectiles for this study. Photon beam energy has to be tuned so as to selectively ionize a specific electronic shell in a molecule, which makes it necessary to employ synchrotron radiation in the soft x-ray band for our experiments. Experiments were performed at Indus-1 Synchrotron facility at RRCAT, Indore. The Indus-1 synchrotron is a 450 MeV electron storage ring with peak storage current of 100 mA. Beam lifetime of Indus-1 is about 4 hours. Radiation in the VUV range is produced at a bending magnet with a critical wavelength of 61 Å. A toroidal grating monochromator (TGM) at Indus-1 beamline (BL-4) is used to select the photon wavelength. At this beamline the photon wavelength can be varied from 40 Å to 1000 Å using two independent grating. Of these, the one we used covers the range 40–120 Å, corresponding to an energy range of 310–100 eV. But in practice, the photon flux beyond 270 eV at our beamline was found to negligible, in part due to the ageing of the gratings. Since our experiments have been carried out at photon energies above 150 eV, the problem of higher order contamination is minor. The photon beam had a cross section of $1 \times 3 \text{ mm}^2$ with a photon flux of about 10^{10} s^{-1} . The energy resolution, $E/\Delta E$, of the mono energetic photon beam was about 300. A polyimide filter was used between the experimental station and the monochromator to avoid contamination of the beam line by the target gas.

Our spectrometer is not limited to photoionization experiments but can also be operated with electron or ion beams, by the simple addition of a Faraday cup at the beam exit.

2.3.2 Electron spectrometer

Energy analysis of the electrons emitted due to ionization of the target gas is done by a Cylindrical Mirror Analyzer (CMA). This analyzer is mounted co-axially opposite to the ion momentum spectrometer (Fig. 2.5). Since a low event rate is mandatory for electron–ion coincidence measurements, it is vital that the genuine electrons from the reaction volume are efficiently detected and analyzed by the electron analyzer. A single pass CMA [61] has a high luminosity, while

offering reasonable energy resolution, and was therefore chosen as the analyzer. In the standard CMA configuration there is no electric field in the reaction zone. In our case, however, this requirement cannot be met as the reaction zone has to be immersed in an electric field for extracting the ions. The CMA is designed with this constraint. The length of the CMA is 106 mm with slit to slit distance of 79.8 mm. The slit width is 3 mm. The outer diameter of the inner barrel and the inner diameter of the outer barrel of the CMA are 42 mm and 89 mm respectively. A grounded disc (g, see Fig. 2.5) with an aperture of 40 mm at its center is placed in front of the CMA. This disc creates a retarding field that compensates for the increase in energy of the electrons due to the field in the extraction gap. Thus, the electrons enter the CMA with almost the same energy with which they were ejected from the atom/molecule albeit with a spread in energies owing to varying angles of ejection. This energy compensation is beneficial due to the fact that the resolution of the CMA decreases with increase in energy. So, for the same initial energy electron, energy enhanced electrons (due to the extraction field) without any energy compensation will be detected with a lower resolution than the electrons which undergo retardation due to the grounded disc. In the standard configuration the included angle of the cone of trajectories entering the CMA is $42^\circ \pm 2^\circ$. In the present configuration the trajectories of electrons are altered by the extraction field. This results in transport of electrons ejected at angles greater than the standard angle to the CMA for energy analysis.

Simulations of the electron spectrometer were done using SIMION 8.0 [62]. Trajectories of electrons of different energy were studied. As expected, simulations show, that due to the electric field applied for ion extraction, the correct angle of ejection for any electron to enter the analyzer depends on the energy with which it is ejected. The extraction field (in the interaction zone) and the subsequent retarding field before the entrance into the CMA radial field distorts the envelope of trajectories entering the CMA, resulting in a larger portion of the Newton sphere being projected onto the CMA slits, increasing the luminosity of the analyzer in comparison with the standard configuration without an

extraction field. For isotropically emitted 70 eV electrons, the acceptance with a field of 166 V/cm is 1.3 times the acceptance without field. The gain is 1.16 for 140 eV electrons. Simulations show that the optimum distance between the source of electrons from entrance slit plane of the CMA assembly is 15 mm. The effusive target jet is therefore set at that distance. The appropriate voltages to be applied to the outer barrel of the CMA for electrons with various energies were calculated. The CMA voltage was found to vary linearly with the energy of the electrons maintaining constant scale factor of 1.6. The angular acceptance of the slit was found to span $\pm 2^\circ$ around the ideal ejection angle for all electron energies. Simulated electron trajectories, assuming a point source for electron emission, are shown in Fig. 2.7.

Two detectors are used in this CMA assembly. One is placed inside the inner barrel of the CMA for detecting energy un-analyzed electrons (D_1), whereas the other is placed at the end of the CMA assembly to detect energy analyzed

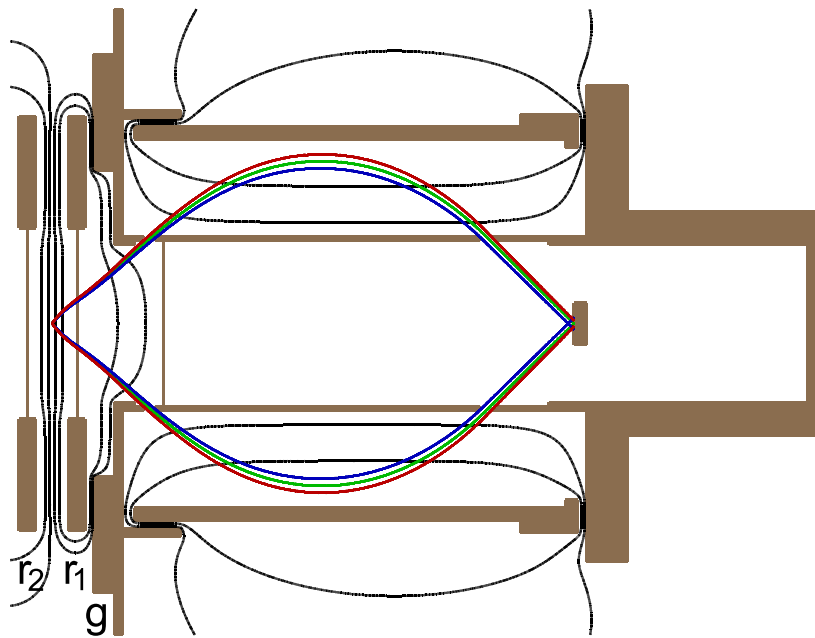


Figure 2.7: Simulated trajectory of electrons with 70 eV energy through the CMA. Trajectory for electrons with ideal angle of ejection is represented by green. Red and blue trajectories are for electrons with ejection angle varying by $+2^\circ$ and -2° respectively from the ideal ejection angle. Black contours are the equipotential lines.

electrons (D_2). A grounded mesh is put in front of the detector D_1 so that field applied to it for electron detection does not affect the trajectory of the electrons entering the CMA. The CMA barrels, meshes and detectors were insulated from each other using Delrin spacers and inserts. The volume and exposed area of the insulators used was kept as small as possible to reduce trapped gas load and spurious static charge effects. The CMA parts were fabricated according to our specifications by the PRL and SAC workshops.

2.3.3 Ion momentum Spectrometer

The ion momentum spectrometer consists of a double field Wiley–McLaren [58] type Time of Flight (ToF) spectrometer with a position sensitive ion detector. The spectrometer is second order space focusing ToF spectrometer, i.e, it compensates for the effect of spatial spread of the ions on their flight times to second order in the initial spread. Three rings (marked r_1, r_2, r_3 , see Fig. 2.5) with the provision to hold a fine meshes are used to generate the extraction field for the ions formed due to ionization. These rings have a outer diameter of 100 mm and an inner (open) diameter of 42 mm. All rings are fitted with fine mesh to generate a uniform electric field. The extraction gap (s) is 6 mm and the acceleration gap (a) too is 6 mm. The gas-jet is placed midway between r_1 and r_2 . After the ring stack is a drift tube of length 162 mm and inner diameter of 42 mm. The drift tube is terminated with a ring and mesh assembly (marked r_4 , see Fig. 2.5). Beyond the drift tube is a position sensitive detector for position resolved detection of the ions. By applying suitable potentials to the extraction rings a static electric field of 166 V/cm is generated in the extraction region, while an electric field 1000 V/cm is created in the acceleration region. The drift region is kept field-free by shorting the drift tube and the rings r_3, r_4 . The detector is biased at -2300 V for detection of ions. The fragment ions formed due to an ionization event were first extracted and then accelerated by the respective electric fields. Then they flew through a field free drift tube to be detected by the position sensitive detector. Upon detection both ToF and ion momentum are recorded. The detection technique is based on multi-particle coincidence technique which

employs electron-ion as well as ion-ion coincidence as described in the previous section. For electron-ion coincidence either the energy analyzed electron or the non energy analyzed electron can be used as the START.

Particle trajectory simulation for this spectrometer was carried out using SIMION 8.0 [62]. Assuming a point source for ion creation and applying the extraction fields as mentioned earlier, it was observed that singly charged ionic fragments having kinetic energy upto 7 eV can be detected without any loss irrespective of their direction of emission. For doubly and triply charged ionic fragments the kinetic energies for which there is complete detection are 14 eV and 21 eV respectively. This is true for any ionic species as the divergence of the ions in the extraction field is roughly proportional to the ratio of the square root of kinetic energy gained by the ion to its charge. The simulated trajectories for a few ionic species are shown in Fig. 2.8.

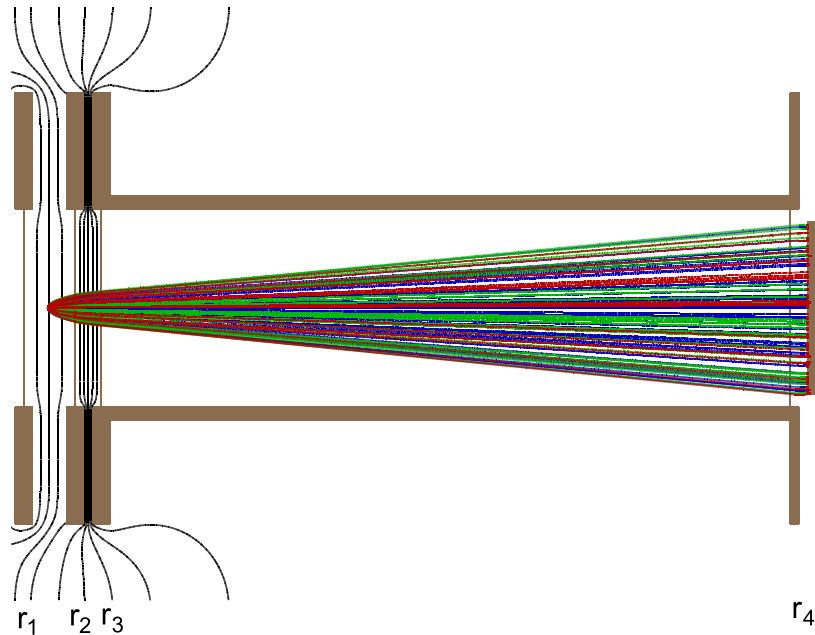


Figure 2.8: Simulated trajectories of C^+ , N^+ and O^+ ions with 7 eV initial kinetic energy emitted isotropically from a point. Black contours are the equipotential lines.

2.3.4 Detectors

Different detectors, based on the multiplication of secondary electrons created by the impact of a charged particle, are used for detection of electrons and ions in the experiment. Though the basic working principle of these detectors is same, they differ greatly in the shape, size and utility.

Electron Detector

Channel Electron Multipliers (CEMs) are used in our experiment for electron detection. A CEM usually has a funnel like structure which is built from glass with a coating of a low work function material and has undulations at the narrow end of the funnel as shown in Fig. 2.9. The wider end of the CEM funnel serves as the electron input side while the narrower end is the detection side. The inner surface of the CEM is coated with a semiconducting low work function material which is highly resistive in nature. At the end of the funnel structure is a metallic anode from which the electron detection pulse is collected. A potential difference is created within the CEM by biasing the narrower end of the funnel with positive high voltage with respect the wider end. When an electron strikes the inner surface of the CEM funnel it produces secondary electrons from the

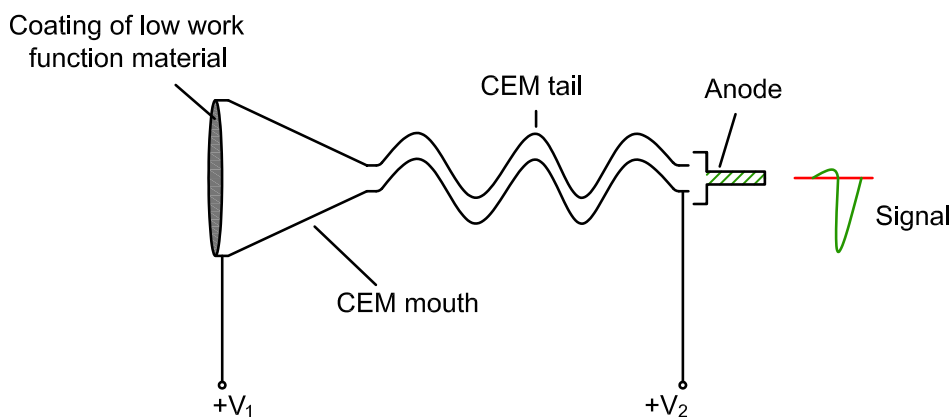


Figure 2.9: Schematic representation of a CEM. For electron detection potential applied at CEM mouth (V_1) and CEM tail (V_2) both must be positive, but satisfy the condition $V_1 < V_2$. The anode itself does a capacitive pick-up of the electron shower and generates the signal.

coating material. These electrons are accelerated due to the potential difference within the CEM and they in turn strike the CEM inner wall to produce more electrons. Due to the positive bias, the electrons moves towards the narrower end of the CEM thus suffering more collisions with walls generating more secondary electrons. The probability of secondary electron creation is further increased by the undulations on the narrow end of CEM which increases the path for the electrons through the narrow channel. Thus for a single electron hit on the CEM surface, an electron shower containing about $10^7 - 10^8$ electrons is generated within the CEM. This electron shower is collected by the anode when it emerges out of the CEM and hence a pulse corresponding to the electron detection is recorded. Alternatively an accelerating potential may be applied to the anode, and the signal can be generated with a capacitive decoupling arrangement.

In our set-up, two CEMs (from Dr. Sjuts Optotechnik, Model : KBL 10RS) of active diameter of 10 mm are used as electron detectors in the CMA assembly. A positive bias of +1800 V is applied to both the CEMs for electron detection.

Ion Detector

For position sensitive detection of ions, a micro channel plate with a delay line anode is used in our experiment. A micro channel plate (MCP), as the name suggests, is a glass plate of about 2 mm thickness having several closely stacked parallel through pores of micrometer diameter (see Fig. 2.10). These micro pores or channels are usually at an angle with the plate surface. Each of these channels has a inner wall coating of a semiconducting and low work function material. For ion detection, a potential difference is maintained across the MCP by applying negative high voltage on ion impingement side with respect to the detection side. Each micro channel in the MCP acts as electron multiplier. When an ion hits the inner surface of a micro channel, secondary electrons are produced from the semiconducting material. These electrons are accelerated due to potential difference across the MCP and hits the wall of channel to generate a cascade of electrons thus amplifying the initial electrons signal by several orders of magnitude. The

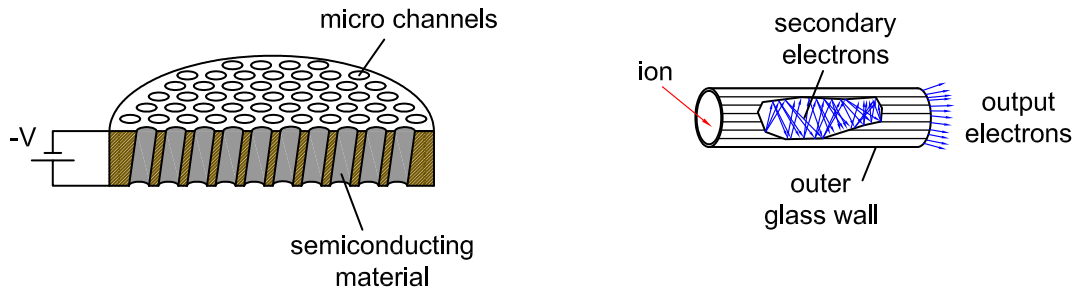


Figure 2.10: [Left] Schematic representation of a MCP. [Right] Electron multiplication inside a micro channel.

flux of electrons eventually emerges out from the opposite end of the channel and is collected by a metallic anode thus producing a ion detection pulse. To increase the gain, it is often necessary to stack a set of MCPs one after the other. When two MCPs are stacked together such that the orientations of the microchannels of the plates mirror each other, it is called Chevron (V-shaped) configuration. In this configuration, the electron shower from the first MCP is further amplified when it passes through the micro channels of the second MCP thus increasing the overall gain. We have used a MCP Chevron pair for our experiments.

The ion hit position on the MCP can be detected by monitoring the position of the electron shower being generated by the ion hit. Various techniques are employed for position detection of the ions e.g. phosphor screen combined with a charged couple device (CCD), wedge and strip type anode, delay line anode etc. We use a delay line anode in our set-up due to its fast readout time and good position resolution for large area of detection. The delay line anode comprises of two bare copper wires which are wound around many loops over a insulating support keeping a fixed gap between the loops. The pairs of wires are wound perpendicular to each other with certain spacing between them. This arrangement is coupled with the MCP such that the electron shower generated due to ion hit falls on the delay lines as shown in Fig. 2.11. When an electron shower falls on the delay lines, the time difference for the signals to arrive at the two ends of the wire depends on the position of the electron shower on the delay line grid. For the crossed pair of delay lines forming x and y grid, the position (x, y)

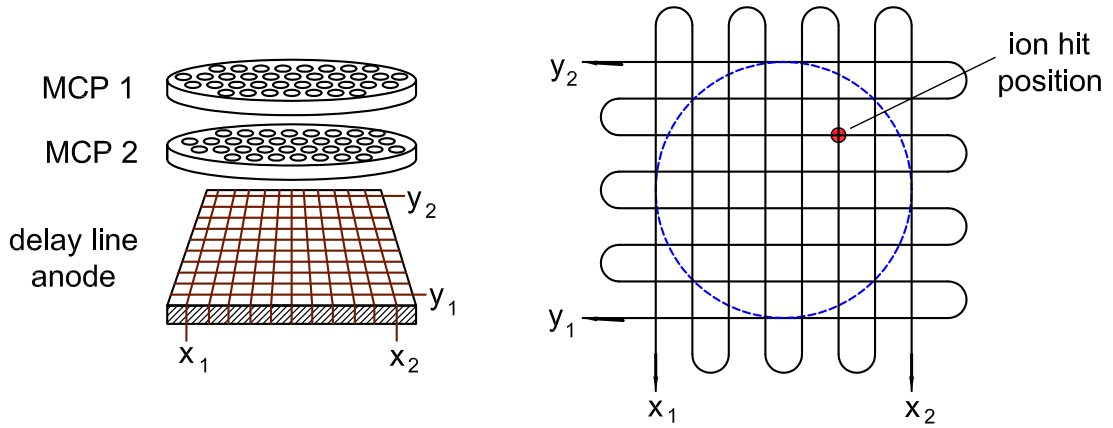


Figure 2.11: [Left] Schematic of the arrangement of two MCPs stacked together along with a delay line anode. The distances between the detectors and delay line wires are exaggerated. [Right] Position encoding of ion detection using a delay line anode. The blue circle marks the effective area of the MCP.

of the ion hit can thus be derived from the time difference between the pairs of signal arriving at the ends of each delay line,

$$x = (t_{x_1} - t_{x_2})v_{sig} \quad y = (t_{y_1} - t_{y_2})v_{sig} \quad (2.11)$$

where, v_{sig} is the signal propagation speed along the delay line which is close to the speed of light. It is to be noted that since the signal propagation time from one end of the delay line to the other is constant for a given length, the total propagation time for x and y delay line *i.e.* $(t_{x_1} + t_{x_2})$ and $(t_{y_1} + t_{y_2})$ is constant irrespective of ion hit position. These time sums can be used during analysis as a consistency check to differentiate true counts from spurious ones.

In our set-up, two MCP of an active area of 40 mm diameter in Chevron configuration along with a delay line anode for position detection is used (from Roentdek GmbH). A negative bias of -2300 V is applied across the MCPs to detect ions.

2.3.5 Spectrometer housing and vacuum specifications

The spectrometer assembly is housed in a stainless steel vacuum chamber with all metal joints. The chamber has a diameter of 160 mm and length of 725 mm with four orthogonal CF63 ports in one plane for the crossed target and projectile beams. The spectrometer is mounted with its axis along the axis of the chamber, so that the projectile beam, gas jet and the spectrometer axis are mutually perpendicular. There are auxiliary ports for pumping, electrical connections and vacuum gauges. The chamber is pumped by a 520 l/s turbomolecular pump backed by a dry scroll pump. The chamber pressure after bake out is 2×10^{-8} mbar, which rises to 5.0×10^{-7} mbar when gas is introduced at 5.0 mbar stagnation pressure behind the effusive capillary. An ionization gauge is used to monitor the chamber pressure while stagnation pressure is monitored by a Pirani gauge. Besides the capillary, gas can be admitted into the vacuum chamber through a 6 mm aperture which is kept away from the ionization region, while maintaining the flow rate. This aperture and the effusive capillary has the same gas input line with the provision of controlling both of them by separate valves. This bypass gas inlet line is used to purge the gas line and can also be useful for recording spectra with the gas flooding the vacuum chamber. Vaporized liquid samples can also be used as target for which the gas line is kept warm to avoid any condensation of the sample in the gas line.

2.3.6 Data acquisition

The experiments are conducted under single collision condition. Simultaneous detection of all the ionic species in coincidence with the electrons ejected in the process are done on an event by event basis. The electrons emitted due to the ionization of atoms/molecules are energy analyzed by the CMA and the energy analyzed electrons are detected by CEM D₂. CEM D₁, on the other hand, detects non energy analyzed electrons. The electron detection signal from the CEM are first amplified by a preamp (ORTEC VT 120) and then fed to a Constant Fraction Discriminator (Philips Scientific, Model 715) to generate a standard pulse

irrespective of small variations in pulse shape and amplitude of the detector output. For generation of electron spectrum, electrons with different energies are admitted in the CMA by varying the voltage in its outer cylinder. A multichannel scalar card (MCS, from FAST ComTec) controls the variable voltage that is applied to the CMA as well as converts the processed electron detection signal from D_2 into digital signal. The digital signal counts are stored as function of CMA voltage in a computer as an ascii file which essentially gives the electron spectrum.

Once the electron spectrum is acquired, the CMA is set to a particular voltage so as to admit electrons with particular energies corresponding to a specific

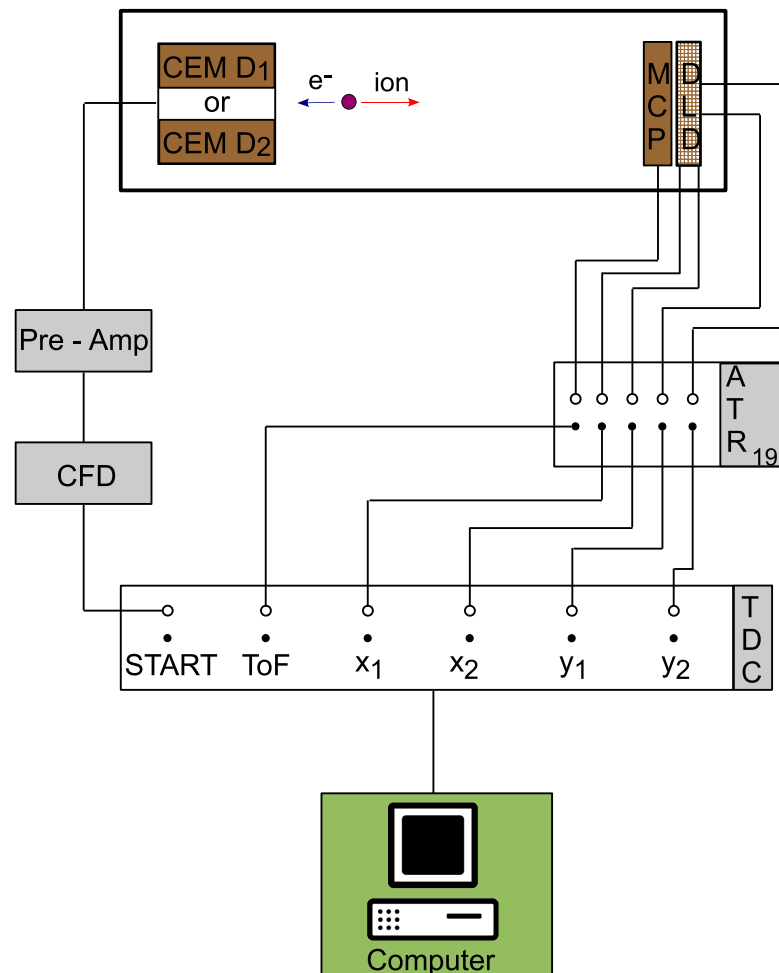


Figure 2.12: Data acquisition scheme.

feature in the spectrum. Taking the discriminated output of electron detection signal from D_2 as START for the ion ToF clock, fragment ions are detected in coincidence with the energy analyzed electrons. Hence, the kinematic information of the fragment ions corresponding to a particular electron decay mechanism producing electrons of a specific energy is revealed. Alternatively, the ion ToF clock START can also be marked by electron detection signal at CEM D_1 to give a consolidated fragment ion spectrum not based on any electron energy discrimination. The STOP signal of the ion ToF clock is derived from the ion detection pulse output of the MCP. For each ion STOP four signals are generated by the delay line, which are processed to obtain the position of the ion hit [63, 64]. All signals from an ion hit (MCP collector and four delay lines) are amplified and discriminated in a ATR 19 unit (Roentdek GmbH). After discrimination all ion flight times (start–stop intervals) are digitized by a time to digital convertor ((TDC), also from Roentdek GmbH). The digitized output is read on an event by event basis and stored as a list-mode file in a computer hard disk by the data acquisition and analysis software called “Computer Based Online-offline Listmode Data Analyzer” or COBOLD PC in short. The TDC has a time resolution of 500 ps. The position resolution depends on the ability to separate the delay line signals in time. For an ideal situation, the time sums of the delay line signals should be single valued. But, in practice, this is not the case and distribution of the time sums gives the effective position resolution of the detector. For our detector it is found to be 0.85 mm. For each event trigger, the TDC remains active for 32 μ s during which up to four fragment ions can be recorded. This makes our spectrometer suitable for studying the complete kinematics of fragmentation of small molecules. The event rate for electron-ion coincidence from the first CEM (D_1) was typically 300–3000 Hz and that with the second CEM (D_2) was 30–150 Hz. The event rate depends on the photon flux at a particular wavelength and the target gas density and additionally, for the second channeltron (D_2), the CMA pass voltage. As is evident, the event rate for the energy discriminated electrons is low hence the first CEM (D_1) becomes extremely useful for calibration and optimization of the ToF spectrometer.

The raw data for electron detection is stored as a histogram and is available as an ascii file and the TDC output for ion detection is stored as a binary file in list-mode format. The data files are used for offline analysis. List mode data acquisition gives us enormous flexibility in analyzing the data after the experiment. This is discussed in the next chapter.

Chapter 3

Data Analysis Methodology

The raw data is analyzed after the experiment employing different methods so as to bring out various information about the kinematics of ionization and the subsequent fragmentation of molecules. The data is first used for calibration of electron and ion spectra before actual analysis can be done. The raw data contains both genuine as well as spurious events. The false events are inherently present in any coincidence experiment like ours due to factors such as unequal count rates for electrons and ions, detection efficiency and dead time issues of the detectors, influence of the background etc. Data analysis is thus done under various conditions and consistency checks so as to minimize the effect of the spurious events and obtain accurate results. Different kinematical parameters are extracted from the data during analysis. These kinematical parameters along with the coincident identification of fragment ions with the energy analyzed electron reveal the complete kinematics of molecular fragmentation due to a particular ionization and electron decay mechanism. The calibration procedures and various data analysis methodology are presented in the following sections.

3.1 Calibration

The first step in any data reduction process is calibration of the data. In our case, the calibration of electron spectrum and that of ion spectrum is done independently but under identical conditions as employed during all the experiments

performed by simultaneously operating the electron and ion spectrometers.

3.1.1 Calibration of the electron spectrum

Calibration of the electron spectrum was done using photoelectrons from ionization of Helium. Photons of various energies were used to generate photoelectrons having different energies. Helium was chosen as target gas for calibration, because it is a simple two electron system with a relatively simple electron spectrum. The electron spectra of Helium due to ionization by photons of various energies are shown in Fig. 3.1. Each spectrum is background subtracted assum-

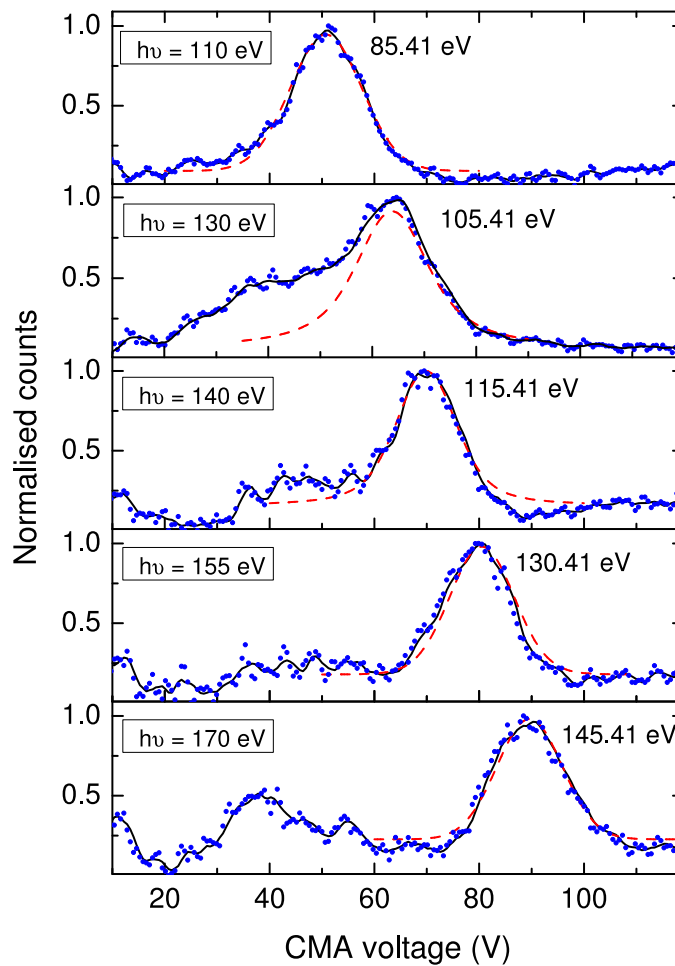


Figure 3.1: Electron spectra of Helium for different photon energies. The dots are experimental data. The black curve is generated by 5 point Savitzky–Golay smoothing [65]. The dashed curve is the Gaussian fit to the spectrum. The photoelectron energies indicated are calculated by subtracting the $1s$ binding energy from the photon energy. The structures on the left hand side of the $1s$ peak may be due to double ionization of Helium.

ing the background to be quadratically decreasing function. The raw spectra are smoothed using the Savitzky–Golay method [65]. The peak in each spectrum is then fitted with Gaussian function. The centroid value of the Gaussian corresponds to single ionization of the $1s$ orbital of Helium which has a binding energy of 24.59 eV [10]. The observed peak is broad owing primarily to the varying energy gain of electrons born at points with different potentials in the extraction gap.

The CMA was calibrated using the Helium $1s$ photo electrons for different photon energies. Fig.3.2 shows the CMA voltage to electron energy relation. The simulated and the experimental calibration curves are seen to have a close agreement. The linearity of the pass energy with the voltage applied to the CMA has a R^2 (coefficient of determination) value of 0.99.

Estimates of the energy resolution, ΔE , of the CMA are derived based on purely geometrical considerations, from simulations and from actual observation.

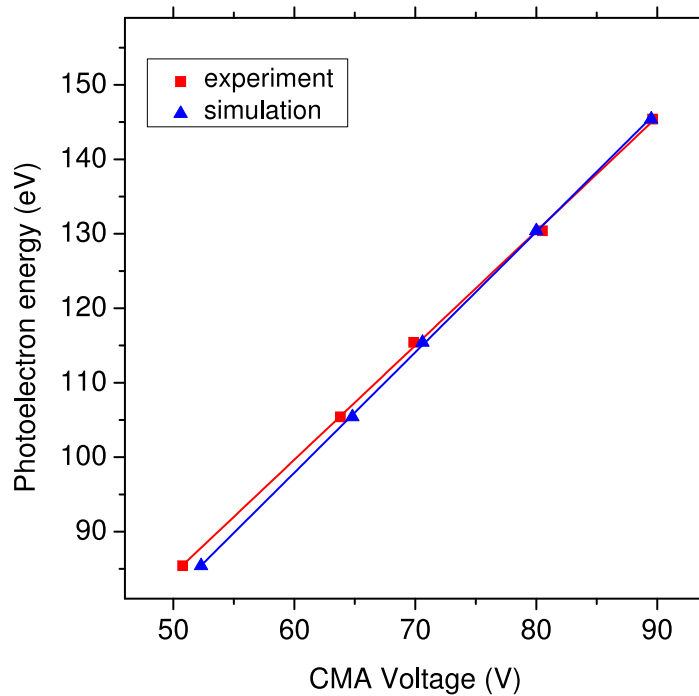


Figure 3.2: CMA calibration curve. Red line is the experimental results and blue line from simulations.

The value of ΔE based on CMA geometry is calculated using equation 2.1, retaining terms up to the second order. The C_w and C_α coefficients have values 2.28 and 35.3 respectively in our case and the values of the geometrical parameters such as slit width (w), angular acceptance of the slit ($\Delta\alpha$) are mentioned earlier. Using these values, for $E = 140$ eV, ΔE is calculated to be 18.1 eV. The value of ΔE from simulations, taking into account the transverse spatial spread of the photon beam, the divergence of the effusive beam (about 2.2 mm at the photon beam molecular beam overlap) and the voltages applied to the spectrometer, is about 40 eV at $E = 140$ eV.

The experimental determination of ΔE is done from the electron spectrum of Argon recorded at 155 eV photon energy shown in Fig. 3.3. This photon energy is well below the $2p$ threshold of Argon hence the electron spectrum generated

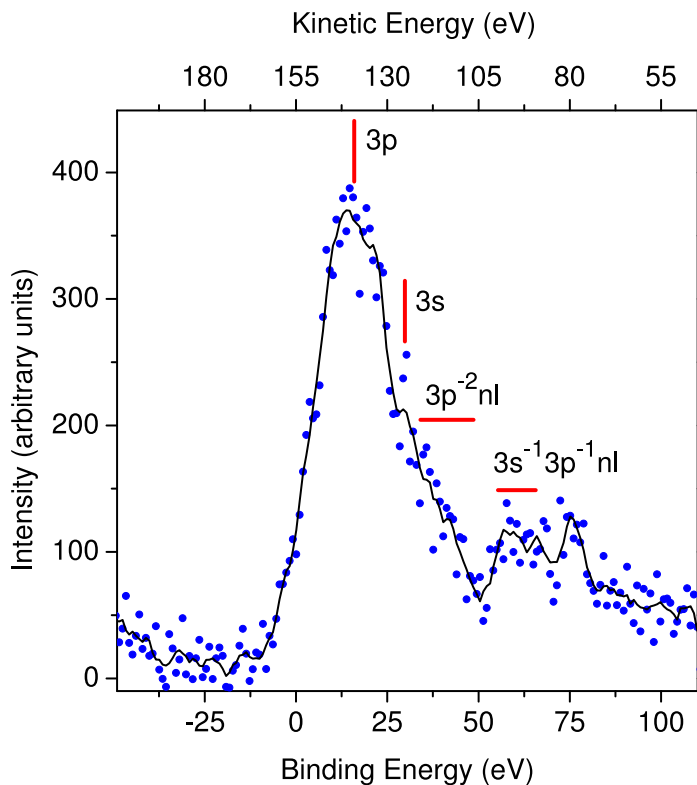


Figure 3.3: Electron spectrum of Argon at 155 eV photon energy. The dots are the experimental data. The black line is generated by Savitzky–Golay smoothing. The $3p$ and $3s$ binding energy values are taken from the NIST database [10], while positions of the satellites denoted by horizontal lines are taken from Kikas *et. al.* [66].

is only due to the valence shell electrons. The raw spectrum is background subtracted and then smoothed using the Savitzky–Golay method [65]. The $3p$ and $3s$ lines are identified according to the NIST database [10] and two bands corresponding to few satellite lines are identified following Kikas *et. al.* [66]. The binding energy scale is obtained by subtracting the kinetic energy of the electrons from the photon energy. The kinetic energy of $3p$ electrons at this photon energy is about 140 eV (binding energies of Argon $3p_{3/2}$ and $3p_{1/2}$ electrons are 15.7 eV and 15.9 eV respectively). Thus, the peak corresponding to $3p$ electrons is used to evaluate the experimental energy resolution (ΔE). For electron of energy $E = 140$ eV, the experimental ΔE was determined to be about 24 eV.

The actual CMA resolution is better than the simulated value primarily due to the asymmetric overlap of the effusive beam with the photon beam. Simulations in conjunction with the actual spectra show, that the overlap between the photon beam and the molecular beam is not optimal. The central axis of the neutral beam (where the number density is highest) does not intersect the photon beam at the mid-point of the transverse spatial extent of the photon beam. The mid-point of the photon beam spot is approximately 1 mm off the mid-plane of the effusive jet, toward the ion spectrometer and does not lie in the virtual zero potential plane as it ideally should, when the extraction voltages are symmetric (but opposite in sign). However, the the distribution of electrons and ions formed in the interaction volume is defined by the distribution of molecules in the effusive beam, not the spatial profile of the photon beam as, the photon beam profile is essentially flat across a 3 mm extent along the spectrometer axis. Due to this asymmetry in overlap, the effective extent of the interaction region is about half of the spread of the effusive beam. This reduction in spatial extent of the interaction region causes the experimental energy resolution to be better than that predicted by simulations. The asymmetry of the interaction region with respect to the zero potential plane in the extraction field, will also lead to a smaller flux of electrons being born closer to the CMA, and in general there will be few electrons contributing to the lower binding energy side of any given peak.

However, the effect is not obvious in the electron spectrum, owing, primarily to the moderate resolution.

3.1.2 Calibration of the ion ToF spectrum

Mass calibration of the ToF spectrum was done using photoionization of Argon at 210 eV (non resonant with Argon shell energies) with the START signal taken from CEM D_1 .

Argon was chosen as it is an easily available atomic gas which yields multiply charged ionic species upon ionization. Molecular gases are less suitable as they produce fragments with large kinetic energy, and few multiply charge parent molecular ions. Analysis of all ion spectra are done employing the time-sum conditions (see section 2.3.4 Ion detector) to reduce contribution from false events. Since ToF varies linearly with $\sqrt{m/q}$, noting the centroid value of ToF peak (t_0) for different charge states of Argon ion and linear fitting of the t_0 vs. $\sqrt{m/q}$ plot gives the calibration equation for a particular set of experimental conditions. The calibration equation evaluated from the linear fit is,

$$t_0 = 576.003\sqrt{m/q} - 35.96 \quad (3.1)$$

The accuracy of this calibration equation was tested by using it to identify ToF peaks of molecular ions whose m/q was known. The calibration equation was found to be satisfactorily accurate. Identification of any unknown ion mass peak in the ToF spectrum is done by employing this equation. Ideally, the intercept of the linear fit equation (*i.e.* equation 3.1) should be zero. But in practice, due to uncertainties in the applied extraction field and length of various regions of the spectrometer and also due to processing delays of the electronics used, the situation deviates from the ideal condition. During analysis however corrective measures are taken by applying appropriate shift in the ToF spectrum such that it resembles the ideal situation.

The FWHM of the Ar^+ peak was found to be 16 ns while the mean ToF

is 3607 ns, which gives a ToF resolution $t/\Delta t = 226$ corresponding to a mass resolution $m/\Delta m = 113$ (see equation 2.4). The ToF resolution also limits the resolution of the component of the ion momentum along the direction of the electric field. The resolution of the axial component of momentum (Δp_z) is given by

$$\Delta p_z = qE_{ext}\Delta t,$$

where q is charge and E_{ext} is the electric field applied in the extraction region. For Ar^+ , $\Delta p_z = 21.6$ atomic units. The resolution of the transverse component of ion momentum is determined by the position resolution of the delay line detector

$$\Delta p_{x,y} = m\Delta x, y/t$$

For Ar^+ , this value is 8 atomic units. In practice however, the accuracy with which the momentum of an ionic species can be determined is affected by additional factors such as the size of the interaction region, thermal energy spread of the target, non-uniformity of the applied fields and deviations in position of the interaction region from the virtual zero potential plane. The uncertainty in measurement of momentum (Δp) is thus estimated from the standard deviation of experimentally obtained distribution in each momentum component for Ar^+ ion. This value is evaluated to be 31.1 atomic units.

Though, using detector D_1 facilitates easy calibration and optimization of the ion spectrometer owing to its large count rate, the background counts in the spectrum are more due to stray electrons. The ToF spectrum when triggered by an energy analyzed electron has fewer false coincidences due to the rejection of stray electrons. The ToF spectrum, triggered by START from an energy analyzed electron (i.e, by CMA detector D_2), corresponding to the $3p$ peak of the electron spectrum is shown in Fig. 3.4.

The asymmetry in the peak shapes of the ToF spectrum can be attributed to the deviation of the interaction region towards the ion spectrometer as discussed earlier. The ion source extent is thus sharply curtailed on the CMA side, resulting

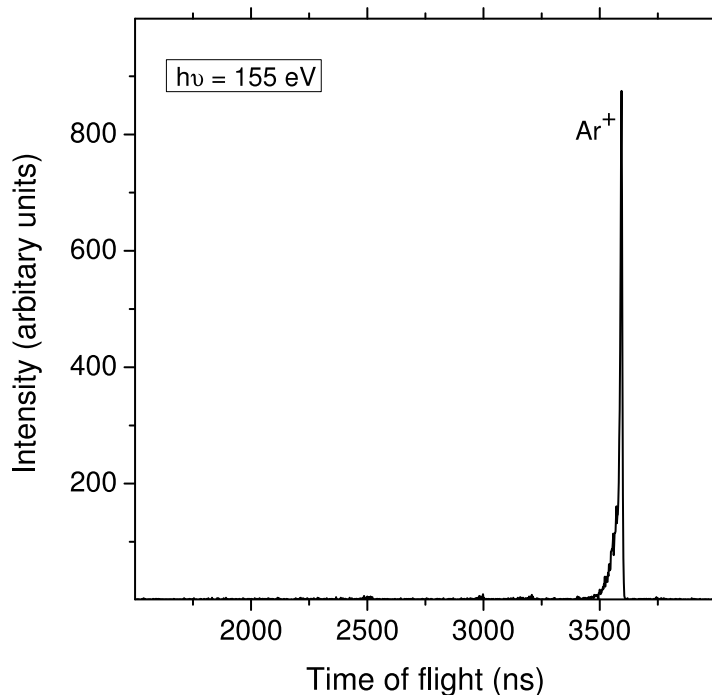


Figure 3.4: Time of flight spectrum of Argon corresponding to ionization of $3p$ shell by 155 eV photons.

in a tail on the lower ToF side of the ToF peak and a sharp truncation on the higher ToF side as can be seen in Fig. 3.4.

3.2 Ion-ion Coincidence Map

Fragmentation of an ionized molecule occur via various pathways. Different dissociation pathways or fragmentation channels as it is called, lead to different fragment ions. The fragmentation channels arising from unstable molecular ions can be visualized in the ion-ion coincidence map, where the ToF of multiple ionic fragments produced in a dissociation event are plotted against each other by sorting the event list. Multi-coincidence detection of the ionic fragments on a event by event basis is mandatory for their coincidence representation. The first fragment ion to be detected in a dissociation event is named as Hit1, the second ion is named Hit2 and so forth. Among the fragment ions arising from the same ionization event, usually a coincidence map is plotted between the ToF of two fragment ions that are detected in succession *i.e.* between Hit1 and Hit2 or Hit2

and Hit3 etc. A ion-ion coincidence map between ToF of Hit1 and ToF of Hit2 for fragmentation of CO₂ upon photoionization by 155 eV photons is shown in Fig. 3.5. The ToF of the ions which are detected later are plotted along y-axis while the x-axis represents the ToF of the ion detected earlier. Since, ions detected later have a larger ToF than of those detected former to them, the lower half of the plot below the line having a slope of 1 remains empty. Since the ToF of a fragment reveals its identity, correlated ToFs of the fragments gives us information about the set of fragments produced in a dissociation event. Hence, each island in the coincidence map denotes a particular fragmentation channel as shown in Fig. 3.5. For a polyatomic molecule like CO₂, if dissociation yields more than two ions, additional coincidence maps (Hit2 and Hit3 coincidence map in case of CO₂) are required to trace the dissociation pathways. In general, for n fragment ions being produced upon dissociation $(n - 1)$ coincidence maps are needed to reveal the complete fragmentation channels.

The cross section of a fragmentation channel or its branching ratio, is reflected in the intensity of the corresponding island in the ion-ion coincidence map. While measuring the cross-section of various fragmentation channels the contribution from false coincidences should be considered. The effect of false coincidences can be reduced by various methods depending on the experimental conditions [67–69]. In our experiment, evaluation of the contribution from false coincidence counts in the electron-ion-ion coincidence data was done as follows. The average counts in a small region where no coincidences are expected, but not lying far from an expected feature, was taken to be the false coincidence contribution to each point in the coincidence spectrum. The contribution due to false coincidence was thus estimated to be about 10% of the total. Features in the coincidence map having significantly higher counts than the threshold value for the false coincidences are considered to be genuine. Another source of error may arise due to the dead time of the MCP and the associated electronics for the detection of ions. Two ions with same mass to charge ratio arriving at the MCP within its dead time are not distinguished and is recorded as a single ion. In our

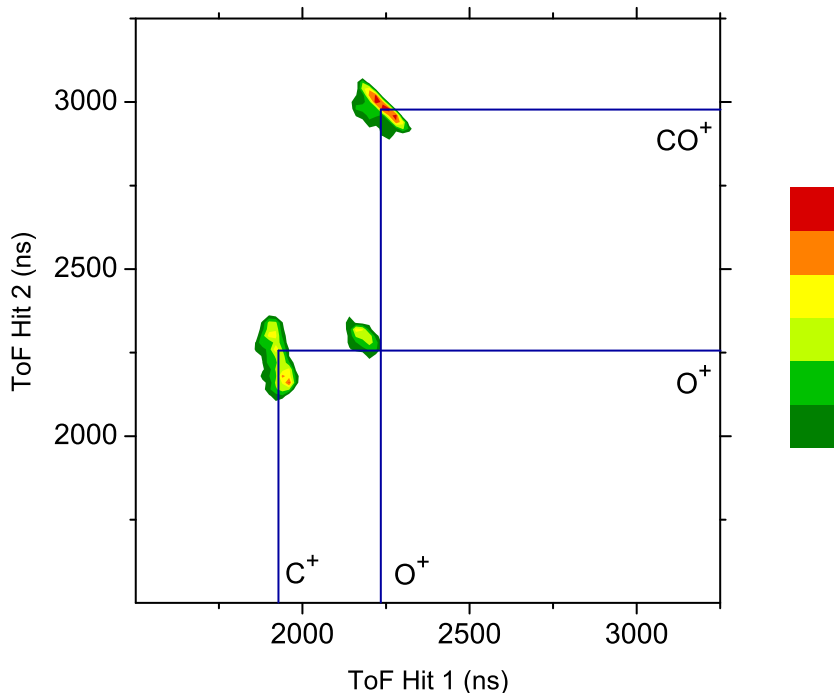


Figure 3.5: Ion-ion coincidence map between Hit1 and Hit2 upon dissociation of CO_2 due to photoionization by 155 eV photons. The colour bar which indicates intensity (increasing from green to red) represents the cross-section for various fragmentation channels. The data presented is above the threshold for false coincidence counts. The set of fragment ions that form a coincidence island are shown in the plot. Three fragmentation channel can be identified, namely, $\text{O}^+ : \text{CO}^+$ which arise due to two body break-up of CO_2 . $\text{O}^+ : \text{O}^+$, which is formed upon three body break-up of CO_2 producing a neutral C atom and two singly charged O atoms and, $\text{C}^+ : \text{O}^+$, in which three body break-up of CO_2 lead to a singly charged C and O atoms while the other O atom may be either neutral or singly charged. The presence of the fragmentation channel $\text{C}^+ : \text{O}^+ : \text{O}^+$ can be confirmed if in addition to $\text{C}^+ : \text{O}^+$ coincidence in Hit1 vs. Hit2 coincidence map, there is an $\text{O}^+ : \text{O}^+$ coincidence in the Hit2 and Hit3 coincidence map.

set-up the dead time is less than 20 ns which leads to a loss of about 27% of the total counts for simultaneous detection of O^+ and O^+ ions with 1 eV kinetic energy, considering a isotropic distribution of the ions.

In addition to the identification of various fragmentation channels, the ion-ion coincidence map also yields information about the dissociation mechanisms. Various insights about a fragmentation process can be gained by studying the structure of the corresponding coincidence island [70]. In general, diagonal island like structure with slope of -1 signifies two body break-up of the molecule

producing two fragment ions with equal and opposite momenta. This can be seen in Fig. 3.5 for two body break-up of CO_2 via $\text{O}^+ : \text{CO}^+$ channel. Three body break-ups on the other hand produce islands having different shapes with various slopes due to complex dissociation mechanisms. A three body break-up may be sequential where the atoms separate from each other one by one or it may be concerted where the separation occurs simultaneously. Both of these break-up mechanisms leave a characteristic signature on the coincidence island between the fragment ions. For a sequential three-body break-up where a neutral or an ion detaches first followed by the separation of the ions for which the coincidence map is plotted, lead to a island with slope of -1 . On the other hand, a sequential or two-step break-up, with one ion separated in the first step, and the remaining two fragments both of which may be charged or only one of them may carry charge separate in the second step, results in an island of slope $-(q_1/q_2)[(m_1 + m_{n,3})/m_1]$, or $-(q_1/q_2)[m_2/(m_2 + m_{n,3})]$. Here, m_1 and m_2 refer to the lighter and heavier ion respectively for which the coincidence map is plotted while q_1 and q_2 are their respective charges. $m_{n,3}$ is the mass of the neutral fragment or the ionic fragment as the case may be. Among the two possible island slope values in this break-up mechanism, an intermediate of $m_1 m_{n,3}$ will yield the first one while second value holds for $m_2 m_{n,3}$ intermediate. The other fragmentation mechanism, namely, concerted break-up, *i.e.* simultaneous breaking of all bonds, may result in an ion-ion coincidence island having slope of any value. In particular, it may result in an island of slope nearly -1 , if the central atom in a triatomic linear molecule like CO_2 has negligible momentum. Infact, such an island can be observed in Fig. 3.5 for three body break-up of CO_2 giving rise to $\text{O}^+ : \text{O}^+$ channel.

Ion-ion coincidence maps are used to identify the fragmentation patterns as well as the mechanism of dissociation for various molecules studied here.

3.3 Newton Diagram

The representation of the correlated momenta of the fragment ions in the molecular frame of reference is called Newton diagram. In this plot, the momentum of the fragment species are normalized and mapped with respect to one of the fragments created following the same dissociation channel. The latter is represented as a vector of unit magnitude along the x -axis, while the normalized momenta of other fragments appears along the y -axis. This kind of 2-D plot is limited to correlated momentum representation of upto three fragments at most. A typical Newton diagram is shown in Fig. 3.6 for three body break-up of CO_2 via $\text{C}^+:\text{O}^+:\text{O}$ channel. Here, the momentum of the second ionic fragment (O^+) is taken as the reference and shown as a unit vector along x -axis, while the momenta of the two other partners are normalized with respect to the second ionic fragment and are mapped in the upper (C^+) and lower (O) half of the diagram respectively. The momentum of the neutral O atoms is determined applying momentum conservation laws. In a three-body break-up such as this, the fragment species may have any momenta but must be confined in a plane while for a two-body break-up momentum conservation dictates that two fragments be produced with equal and opposite momenta. Thus, for a two body break-up Newton diagram will ideally have the momenta distribution with equal magnitude and confined only along the x -axis but on opposite quadrants of the plot.

The Newton diagram can lead to the geometry of the transient molecular ion at the time of break-up [71] and also shed light on the dissociation mechanism. The geometry of the transient molecular ion in the case of three-body break-up of a triatomic molecule can be estimated to some extent by computing the relative angles between the fragment momenta shown in the Newton diagram. A linear triatomic transient molecular ion will yield the momentum distribution of the central atom mostly confined near the origin. Deviation of the central atom momenta from the origin suggests a bent geometry of the transient molecular ion where the degree of deviation marks the degree of bending. This can

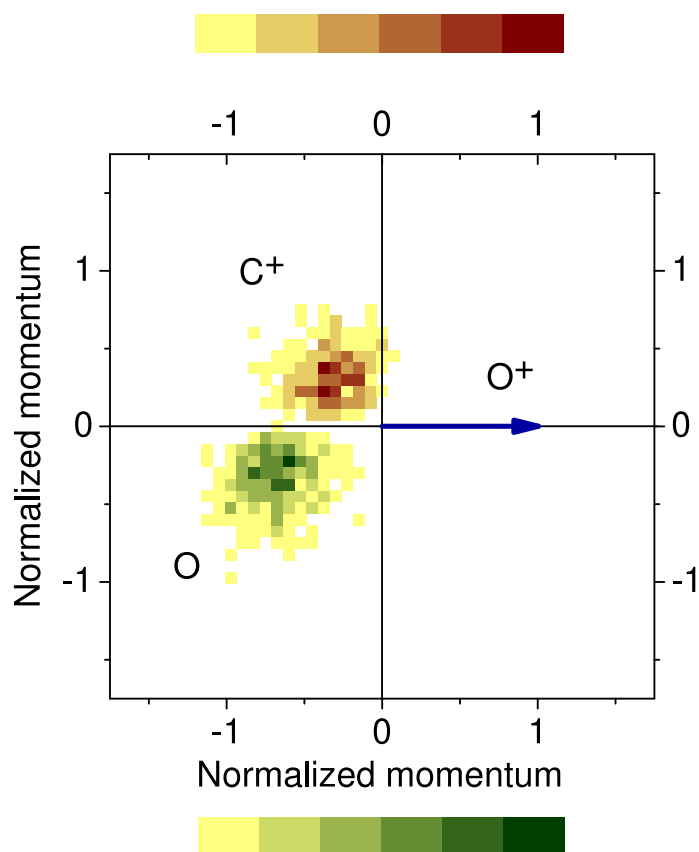


Figure 3.6: Newton diagram for three body break-up of CO₂ via C⁺:O⁺:O channel. The blue arrow along x -axis denotes the momentum of O⁺ normalized to 1. The normalized momentum distribution of C⁺ and O is shown in the upper and lower half of the graph. Colour bar indicates intensity, increasing from light to dark.

be observed in Fig. 3.6 for dissociation of CO₂ via C⁺ : O⁺ : O channel indicating that the linear CO₂ molecule attains a bent geometry at time of break-up.

Different dissociation mechanisms produces distinct features in the Newton diagram. In the case of sequential fragmentation of the triatomic molecule, the distribution of the momenta shows a semicircular feature. This is attributed to the rotation of the diatomic intermediate before it breaks up, as observed in the case of dissociation of CO₂³⁺ [72]. Also, in a sequential break-up mechanism, the momenta distribution of the fragments produced upon break-up of the intermediate will be equal in magnitude and opposite in direction while the other partner will be at an angle of 90° with respect to these fragments. In the case of

a concerted break-up no such feature is observed. Thus by observing Fig. 3.6, one can infer that the dissociation mechanism is a concerted one.

3.4 Kinetic Energy Release

Perhaps the most important parameter required to understand the kinematics of molecular fragmentation is the kinetic energy release (KER). When an excited unstable molecular ion fragments, the excess energy is released in the form of kinetic energy of the fragments. In our experiment, the kinetic energy of each fragment ion in a dissociation process is evaluated from the experimentally measured momenta of the ion. If p is the momentum of an ion of mass m , then its kinetic energy is given by $KE = p^2/2m$. The correlated momenta of all ions pro-

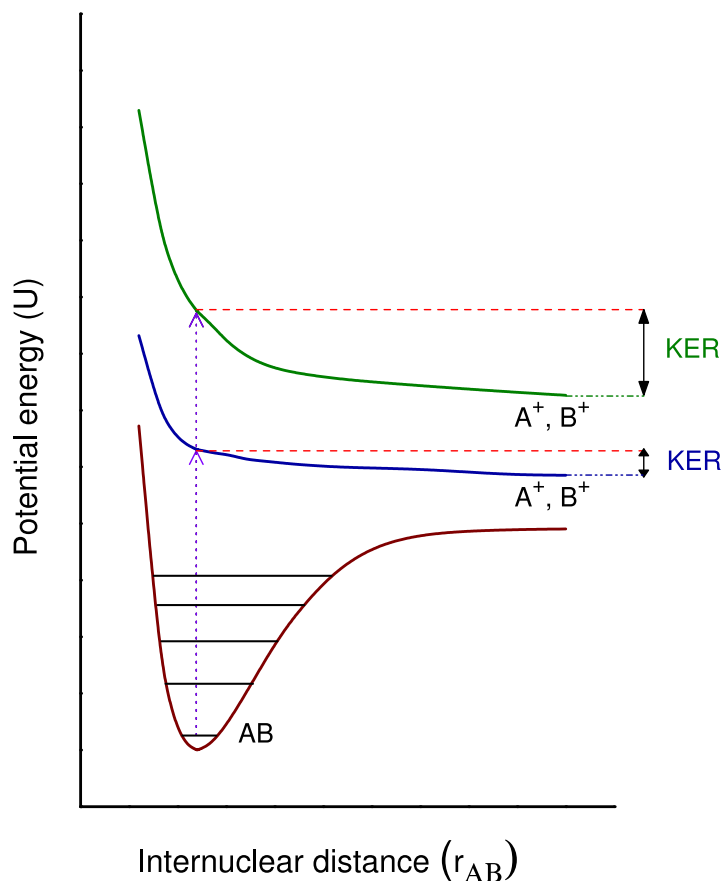


Figure 3.7: Molecular potential energy curves depicting KER of a molecule AB dissociating to A^+ and B^+ . The dotted arrow represents the excitation energy supplied to the molecule by ionization. Note that excitation of the molecule into more repulsive PEC will lead to higher KER.

duced in the dissociation event yields the correlated kinetic energy information of the fragments ions. Kinetic energy of a neutral fragment from a dissociation event can also be derived using conservation laws, provided all the other fragments are ionic. The sum of the kinetic energy of all the fragments produced in the dissociation event gives the total kinetic energy that is released in the fragmentation process.

The KER in a dissociation event is governed by the nature of potential energy curve (or surface) the molecular ion is excited to during dissociative ionization. The KER value is the difference between the internal energy of the molecular ion and that of the fragments at asymptotic limit. Fig. 3.7 shows the schematic representation of KER for few typical potential energy curves (PECs). It can be seen that PECs which are more repulsive in nature tend to yield more KER. Usually, a set of PECs are accessed for a given ionizing perturbation. Decays of the molecular ion following these different PECs give different KER values. Thus, in experiment, for a particular dissociation channel a distribution of KER is obtained. The range of the KER distribution depends on the nature of the PECs

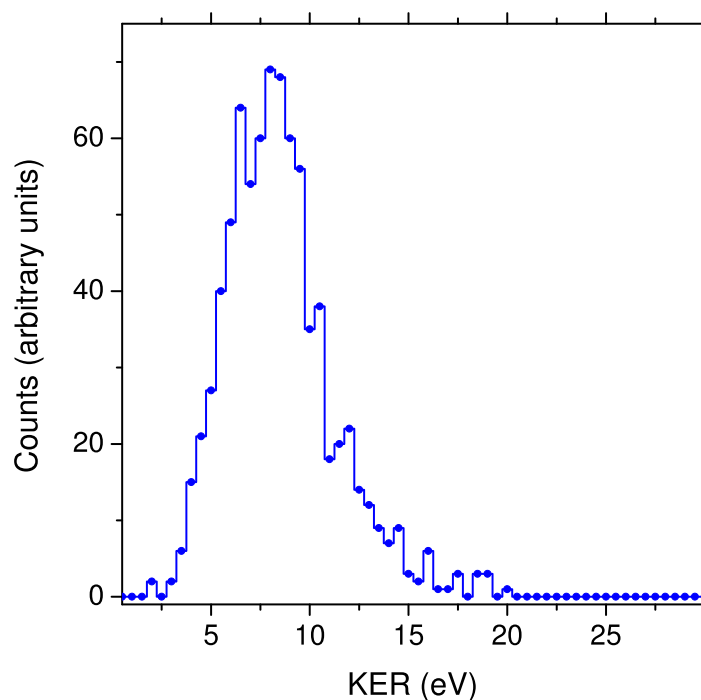


Figure 3.8: The KER distribution upon fragmentation of CO_2 into O^+ and CO^+

from which the fragmentation occurs, while its intensity distribution depends on how much the different PECs are populated due to the ionizing perturbation. Hence, the knowledge of the KER proves to be essential for identification of PECs which take part in dissociation and also to know the likelihood that a PEC will be accessed due dissociative ionization. The KER distribution for fragmentation of CO_2 into O^+ and CO^+ is shown in Fig. 3.8. The accuracy in the computation of KER in our experiment is limited by the momentum resolution. The estimated error in an ion pair KER measurement is 0.46 eV.

3.5 Dalitz Plot

The conformation of the transient molecular ion can be visualized in great detail in a Dalitz plot [73]. The geometry information is revealed by computing the correlated momenta of the fragments in terms of reduced energy which forms the co-ordinate of these plots. The most general form of the Dalitz plot co-ordinates for a triatomic molecule are given by

$$\begin{aligned} \text{DalitzX} &= \frac{E_2 - E_1}{\sqrt{3E}} \\ \text{DalitzY} &= \frac{E_3}{E} - \frac{1}{3} \end{aligned} \quad (3.2)$$

where, E_1 , E_2 and E_3 represents the kinetic energy of the individual fragments while E is the total kinetic energy released upon dissociation. These coordinates are arrived upon by representing the energy phase space of the three fragments formed upon dissociation of the molecule in terms of only two coordinates linked by the energy and momentum conservation laws [74, 75]. For a homonuclear triatomic molecule momentum and energy conservation dictates that the Dalitz plot be confined in a circular region of radius $1/3$. But for heteronuclear molecule the Dalitz phase space is oval in shape. If two atoms in a triatomic molecule belongs to the same element (like CO_2) the Dalitz plot can be represented within a circular region having radius $1/3$ if the co-ordinates are modified to,

$$\begin{aligned} \text{DalitzX} &= \sqrt{\frac{M}{m_3} \frac{E_2 - E_1}{3E}} \\ \text{DalitzY} &= \frac{M}{m} \frac{E_3}{3E} - \frac{1}{3} \end{aligned} \quad (3.3)$$

where, M is the mass of the molecule, m is the mass of the atoms of the same element while E_1 and E_2 are their respective kinetic energies [75]. m_3 is the mass of the other atom and E_3 represents its kinetic energy. E is the total KER from the fragmentation process. Each point in the Dalitz plot represents a certain momentum vector geometry of the transient molecular ion at the time of break-up as illustrated in Fig. 3.9 for a few points.

The Dalitz plot co-ordinates given by equation 3.3 is used in our analysis.

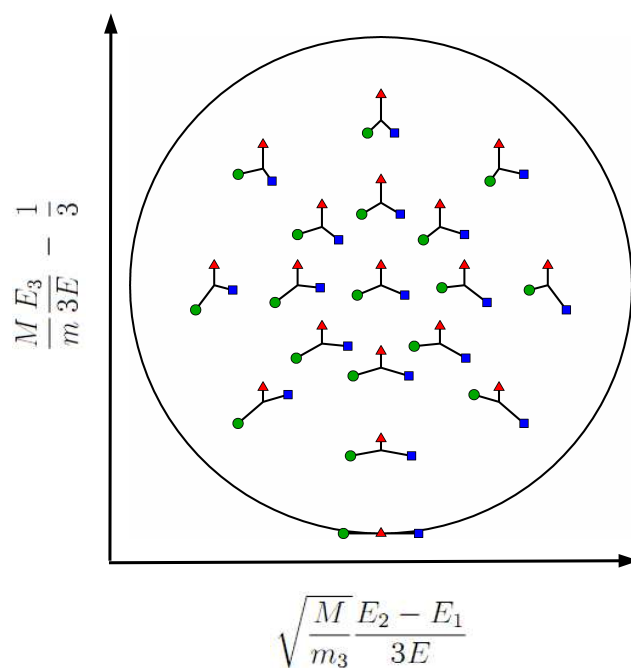


Figure 3.9: Characteristic momentum vector geometry of a triatomic transient molecular ion in Dalitz plot. See text for details. \blacktriangle denotes the momentum of the ion having mass m_3 . \blacksquare marks the momentum of the first atomic fragment of mass m to be detected while \bullet gives the momentum of the other atom having mass m .

The data analysis techniques discussed are essential to understand the ionization and dissociation mechanisms of molecules. We have employed these methods extensively to gain valuable insights about different ionization mechanisms and its effect on molecular fragmentation. The results of our studies are presented in the next chapter.

Chapter 4

Results and Discussions

The focus of our work is to study the dependence of dissociation pattern and the kinematics of dissociation of molecular ions on the ionization mechanism leading to their formation. Ionization may involve participation of different orbitals and this leaves its unique signature on electron decay mechanisms which in turn affect the energetics of the process. Thus, the state attained by transient molecular ion and its subsequent dissociation is expected to be dependent on the electron relaxation mechanisms consequent to the primary ionization. We have studied the dissociation in simple molecules (di- and tri-atomic molecules) following valence as well as core ionization leading to various electron decays. Small molecules are suitable for this study because kinematically complete detection of the fragments arising due to fragmentation can be achieved. Also, the electron relaxation mechanisms in large molecules are fairly complex thus making it difficult to track the subsequent fate of the molecule. We report here case studies for valence ionization of CO while the dissociation of OCS and CS₂ upon sulphur (*2p*) core ionization is dealt with in detail. For core ionization, studies are limited to sulphur (*2p*) ionization as energetically the *2p* shell (core) of sulphur is accessible with the range of photon wavelengths available at Indus-1 synchrotron.

4.1 Valence ionization of CO

Absorption of photons by a molecule leading to the emission of electrons from the valence orbitals is termed valence photoionization. For a given photon energy, the kinetic energy with which the photoelectron is emitted depends on the binding energy of the orbital from which it is ionized. This as discussed earlier is given by $E_{pe} = E_P - BE$ (equation 1.10 Chapter 1) where, E_P is the photon energy and BE is the binding energy of the orbital. In general, if the photon energy is sufficiently high, a number of valence orbitals are accessible for ionization. Thus, upon valence photoionization of molecules, electrons of different kinetic energies are produced which bear the information about which valence orbital has been ionized. Ionization of different valence orbitals leaves the molecular ion with different electronic configurations and internal energy gained via the ionization process. Hence, the time evolution of the molecular ions formed upon ionization of various valence orbitals may be quite different from each other, affecting its stability and dissociation patterns. In our study on CO, the effect of ionization of various valence orbitals upon molecular ion formation and its subsequent dissociation has been highlighted.

We have carried out ionization of CO at 155 eV photon energy. This photon energy is non-resonant with the energy levels of CO, but is sufficiently higher than the double ionization threshold of CO, so at this energy some deep-lying electronic levels can be excited to ionization. It is to be noted, that the core (K) shell of neither O nor C can be ionized with this photon energy. Thus only valence ionization of CO is possible at this photon energy.

The electron spectrum of CO recorded by the CMA upon excitation by photon beam of energy 155 eV is shown in Fig. 4.1. The kinetic energy of the electrons is shown at the top axis of Fig. 4.1, while the binding energy is obtained by subtracting the kinetic energy from the photon energy (*i. e.* $BE = E_P - E_{pe}$) is shown at the bottom axis. The raw spectrum is background subtracted following

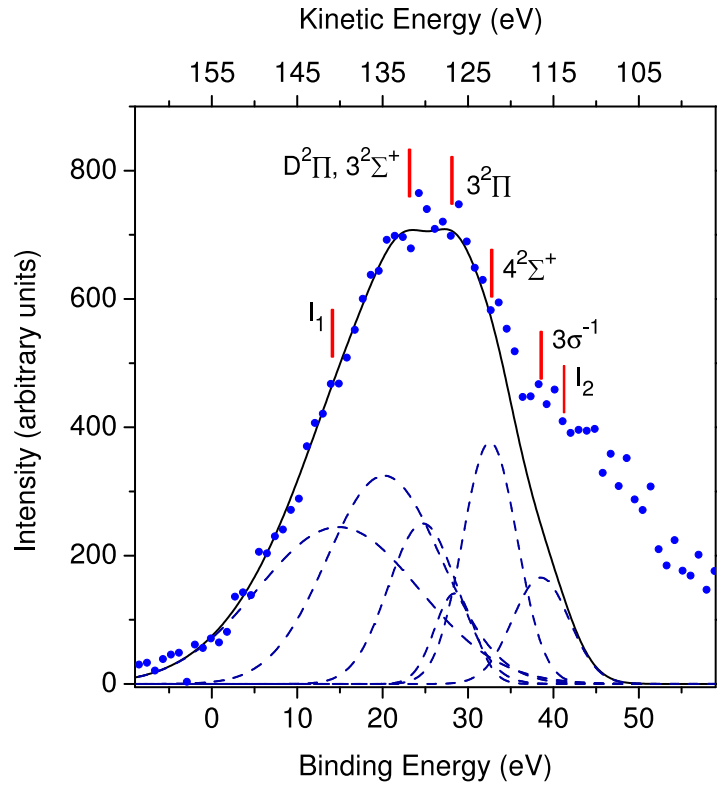


Figure 4.1: Electron spectrum of CO at 155 eV photon energy. Dots are experimental data. The black curve is the sum of multiple Gaussian fits, the latter shown by dashed curves. The fit extends only up to the double ionization threshold, as beyond this energy the two ejected electrons share the energy continuously, leading to a continuum distribution. I_1 and I_2 indicate the single and double ionization potentials, taken from the NIST database [10] and Hochlaf *et.al.* [76], respectively. Line identification in the range 22 eV to 40 eV follows Eland *et.al.* [77].

a quadratic fit to the background, and a multiple Gaussian fit is made to the subtracted spectrum following the Levenberg–Marquardt method [78]. The initial values of the centroids and the number of Gaussians for the fitting procedure were set by a correspondence with the major features reported by Eland *et.al.* [77]. The centroids were not frozen to the initial values in the fitting procedure. In the final fit, the centroids were found to deviate from the values in the literature by approximately 1 eV. The first and second ionization potentials I_1 and I_2 values are taken from the NIST database [10] and Hochlaf *et.al.* [76], respectively. The fit extends only up to the double ionization threshold, as beyond this energy the two ejected electrons share the energy without restriction, leading to a continuum distribution.

The binding energy scale up to I_2 depicted in the Fig. 4.1 gives us a measure of the energy gained by the molecular ion through ionization (*i.e.* the excitation energy). The excitation energy is given by $E_{exi} = E_P - E_{elec}$ (equation 1.12 in Chapter 1) where, E_P is the photon energy and E_{elec} represents the kinetic energy of all the ejected electrons. Thus, for single ionizations, the magnitude of E_{exi} is equal to the binding energy. For valence double ionization, the excitation energy can only be determined if the kinetic energy with which both the electrons are emitted is known. In our experiment the energy of only one electron can be determined at a time, thus the excitation energy upon valence double ionization can not be estimated.

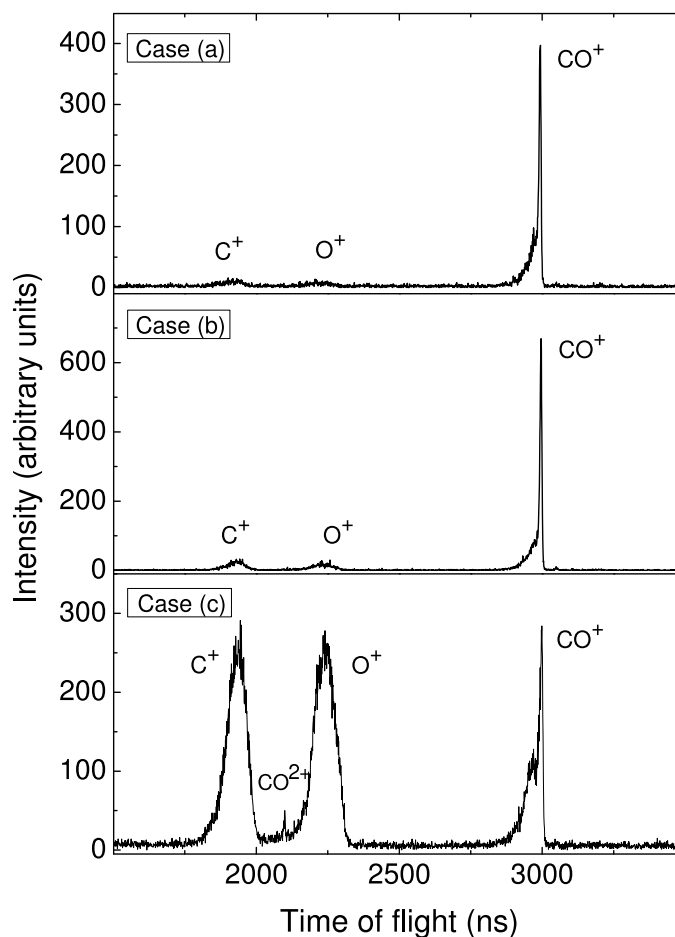
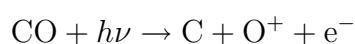
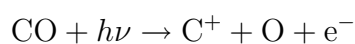


Figure 4.2: Time of flight spectrum of CO corresponding to different electron energies as described in the text.

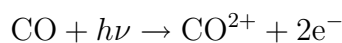
We present the ion ToF spectra triggered by electrons falling in three energy bands of the electron spectrum corresponding to

- (a) excitation just above the single ionization threshold of CO
- (b) excitation well above single ionization, but below double ionization, mostly leading to $D^2\Pi, 3^2\Sigma^+$ states of CO^+
- (c) excitation just above the double ionization threshold of CO

The ToF spectra shown in Fig. 4.2 are obtained at different pass energies, and recording the ion spectrum in each case. The ToF spectra in the three cases are drastically different, indicating that the stability and the fragmentation patterns of the molecule are strongly affected by which of the various valence orbitals is ionized. The species resulting from relaxation of singly ionized CO can be summarized by the following processes:



while those resulting from doubly ionized CO can be summarized by the following processes:



The difference in the yield of various species produced due to different valence ionization of CO can be attributed to the different excited state PECs accessed depending on the energy available to the molecular ion post electron removal. When ionization of low binding energy orbitals occurs, like in cases (a) and (b),

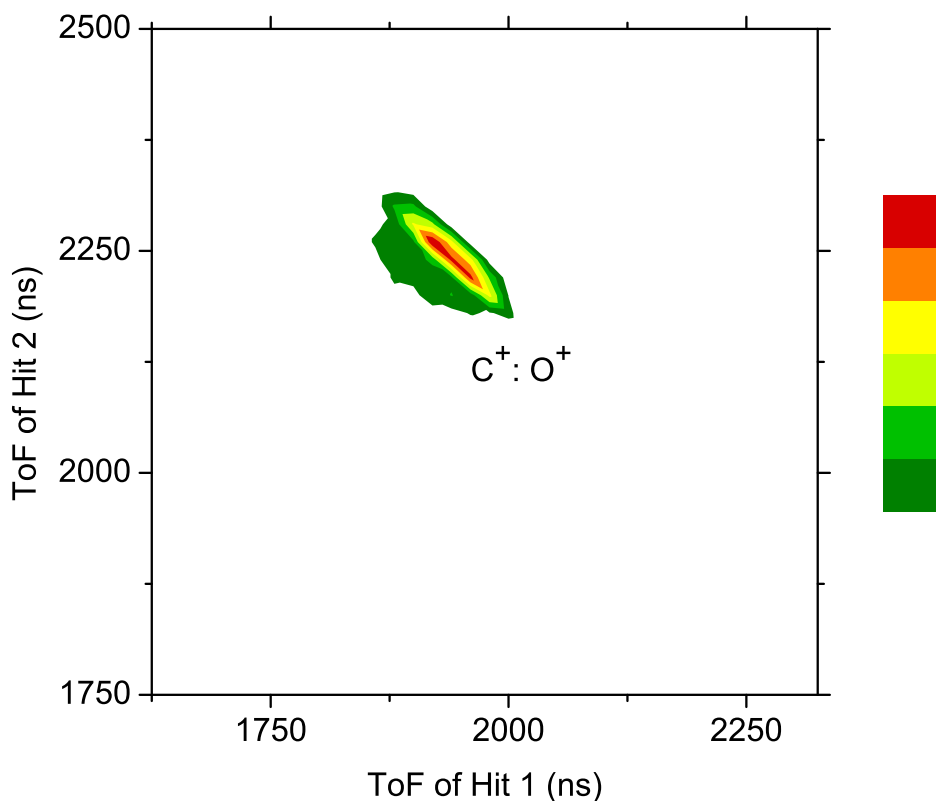


Figure 4.3: Ion-ion coincidence map showing $C^+:O^+$ island. Colour bar indicates intensity increasing from green to red. The data presented is above the threshold for false coincidence counts.

most of the photon energy is carried away by the ejected electron. Thus, the energy gained by the molecular ion is very small, insufficient to break the molecular bonds. Hence, the dominant product formed in this type of ionizations is the stable molecular ion CO^+ . Nevertheless, we observe some dissociations in these cases. The only open dissociation channels are $C^+:O$ and $O^+:C$. The cross section for dissociation is larger in case (b) as compared to case (a) because the energy gained by the transient molecular ion is more in this case. Thus, the propensity to molecular bond break is greater in this case. Case (c) however, indicates onset of double ionization and transitions to high-lying dissociative states of CO^+ . The cross section for dissociative single ionization channels far exceeds that for non-dissociative channels as now the energy gained by the transient molecular ion is sufficiently high to favour bond break. The onset of double ionization is signalled by the observation of CO^{2+} for this case.

For case (c), the information about the fragmentation channels for dissociative double ionization of CO can be gained from ion-ion coincidence map shown in Fig. 4.3. Opening up of the $C^+:O^+$ channel in case (c) is revealed in the correlation map. $C^{2+}:O$ and $O^{2+}:C$ channels are not observed at these photoelectron energies, showing that the threshold for charge symmetric dissociation is lower than that for charge asymmetric dissociation of CO^{2+} .

The results discussed above indicate that for the case of valence photoionization, singly ionized stable molecular ion is the dominant product when low binding energy valence orbitals are ionized. The cross section for fragmentation increases as higher binding energy orbitals are ionized which provides more excitation energy to the molecular ion required for bond break-up. Above the double ionization threshold, both stable and unstable CO^{2+} are formed. In general, multiply charged molecular ions have a higher propensity towards dissociation due to larger internuclear Coulomb repulsion as compared to singly ionized ones. Fragmentation of multiply charged molecular ions produce ionic fragments and by detection of these ions the complete kinematics of the fragmentation process can be studied. On the other hand, singly charged molecular ions dissociate to yield only one charged fragment and the remaining fragments are neutrals which cannot be detected. This does not pose any problem for the case of diatomic molecules but for polyatomic molecules, the kinematics of dissociation is not accessible. Thus multiply ionized tri-atomic molecular ions are ideal candidates for the kinematically complete study of dissociative ionization of molecules.

Valence photoionization yields multiply charged molecular ions but with a lower cross section than for single ionization. Further, the complete electronic decay mechanism and the excitation energy gained by the molecular ion upon valence multiple ionization of molecules cannot be determined as the energy of only one electron can be monitored at a time in our experiment. Core ionization, on the other hand, tends to produce multiply charged molecular ions due to secondary electron decay mechanisms like Auger decay. The Auger electrons are

emitted with kinetic energies characteristic to the orbitals that take part in the decay (see equation 1.11 of Chapter 1) thus providing rich information about the energetics of the electron decay mechanism. Hence, we focus on core ionization and subsequent dissociation of molecules in our studies and the following sections discuss the results we have obtained.

4.2 Core ionization and fate of excited molecule

Dissociation of molecules due to core ionization has been a subject of great interest during the last few decades. Apart from identification of ionic fragment upon core ionization [79–83], the attempt has been on establishing the fragmentation pathways of the core ionized molecule [84–87]. Core ionization of molecules often leads to Auger decay. This results in filling of the core vacancy producing two valence shell holes with the emission of Auger electrons in the process. Auger electrons are produced with a specific kinetic energy characteristic of the binding energy of the valence orbitals that take part in the decay process. Thus the kinetic energy of the Auger electrons carries the information about the final electronic configuration of the molecular ion. The dynamics of this doubly valence ionized molecular ion states govern the fragmentation pathways and hence the ionic fragments produced upon core ionization.

We have carried out experiments involving core ionization of sulphur bearing molecules like OCS and CS₂. The photon energy available at the Indus-1 synchrotron facility is suitable for ionization of 2*p* core orbital of sulphur. Other core orbitals of sulphur, oxygen and carbon are not accessible by the photon energy available at this facility. Ionization of sulphur 2*p* orbital was carried out using photons of energy equal to the binding energy of 2*p* orbital and the resulting Auger electron spectrum was recorded. This allows us to estimate the amount of excitation energy gained by the molecular ion. Following equation 1.12 in Chapter 1 the excitation energy upon S(2*p*) Auger decay can be written as,

$$E_{exi} = E_P - E_{2p} - E_{Auger} \quad (4.1)$$

where, E_P is the photon energy and E_{2p} represents the kinetic energy of ejected $2p$ electrons while E_{Auger} is the Auger electron energy. Now, since the photon energy is matched with the binding energy of the $2p$ orbital the kinetic energy of the ejected $2p$ electron, E_{2p} will be ideally be zero (equation 1.10 Chapter 1). Hence, we have,

$$E_{exi} = E_P - E_{Auger} \quad (4.2)$$

Thus, by only knowing the energy of the emitted Auger electrons, the excitation energy supplied to the molecular ion due to a particular Auger decay can be estimated. This is in contrast to valence ionization producing multiply charged molecular ion, where knowledge about the energy of all the ejected electrons is required to estimate the excitation energy gained by the molecular ion.

4.2.1 Auger decay and fragmentation channels of S($2p$) core ionized OCS

OCS is a linear molecule having a ground state valence electronic configuration of $6\sigma^2 7\sigma^2 8\sigma^2 9\sigma^2 2\pi^4 3\pi^4$. Fig. 4.4 shows the electron spectrum of OCS when ionized by 172 eV photons. Since the photon is capable of producing a core hole at S $2p_{1/2}$ as well as S $2p_{3/2}$ (which is 1.2 eV lower in energy due to spin orbit splitting [88]) states, Auger decay follows and the spectrum we get is the LVV Auger spectrum of OCS.

The raw spectrum is background subtracted and fitted with multiple Gaussian functions with centroids corresponding to each discernible feature. Owing to the width of the molecular jet and application of a constant electric field of considerable strength for ion extraction, the resolution of the electron spectrum is moderate, but is enough to pinpoint the broad features in the spectrum. The horizontal bars labelling the spectrum denote the band of Auger hole states of the

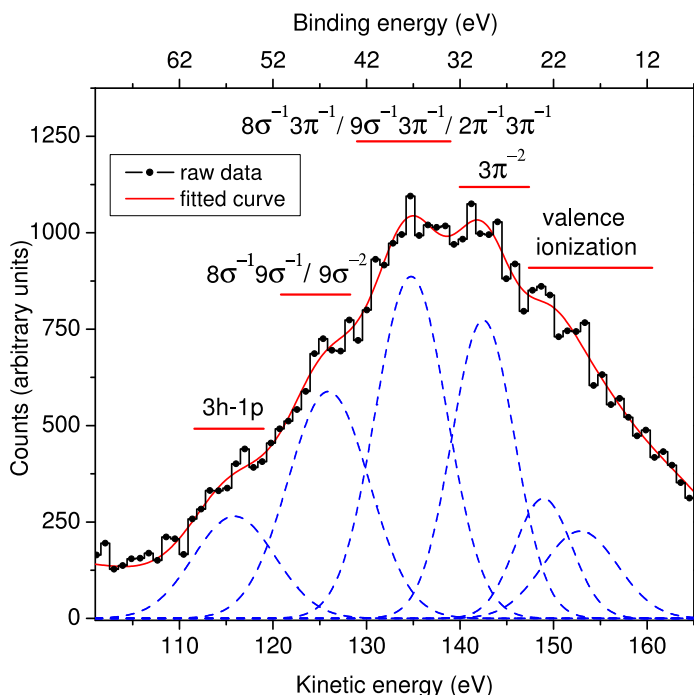


Figure 4.4: Broad features of the S($2p$) Auger electron spectrum of OCS. Features for both S $2p_{1/2}$ and S $2p_{3/2}$ Auger decay are contained in this spectrum. The histogram is raw data, the continuous (red) curve is the cumulative curve of multiple Gaussian fits corresponding to various states, the Gaussians being shown as dashed (blue) curves. Auger states are identified following [89] and [90]. The binding energy scale at the top is obtained by subtracting the Auger kinetic energy from S $2p_{1/2}$ threshold. Groups of close-lying doubly ionized states resulting from Auger decay are indicated by horizontal lines.

molecule. The states are identified following [89] and [90]. The $(3h - 1p)$ states correspond to Auger transitions that produce 3 hole 1 particle type of electronic configuration, which result when 3 vacancies are created in the molecular orbitals and 1 electron is excited to one of the virtual orbitals instead of being ejected. The centroids of the fit are found to match within 2 eV of the value reported in the literature. The mixing of events from neighbouring states with a particular Auger state owing to the low CMA resolution is estimated to be between 10% to 12%. The binding energy scale shown at the top of Fig. 4.4 is obtained by subtracting the Auger electron energy from the $2p_{1/2}$ ionization energy. Hence the binding energy gives us a measure of the excitation energy that is supplied to the molecule in its ground state due to a particular Auger decay (see 4.2). Ionization of lower binding energy state signifies lesser energy available to the

internal degrees of freedom of the residual molecular ion, while ionization of higher binding energy states signifies greater energy for the same.

The ToF spectrum of first fragment upon ionization of OCS corresponding to each electronic decay process is given in Fig. 4.5. Since the Auger process is inherently a two electron removal processes, the ion ToF spectrum is dominated by OCS^{2+} and fragments arising from its break-up. Ionization to lower binding energy states leads to the formation of stable OCS^{2+} . The cross-section for the formation of stable OCS^{2+} is highest following $3\pi^{-2}$ excitation, leading to OCS^{2+} in the ground state [91]. As higher energy becomes available to the molecular ions following ionization of higher binding energy states, the molecular ion is left in states that are by and large repulsive in nature, resulting in dissociation of the molecule. A similar observation has been reported earlier [92].

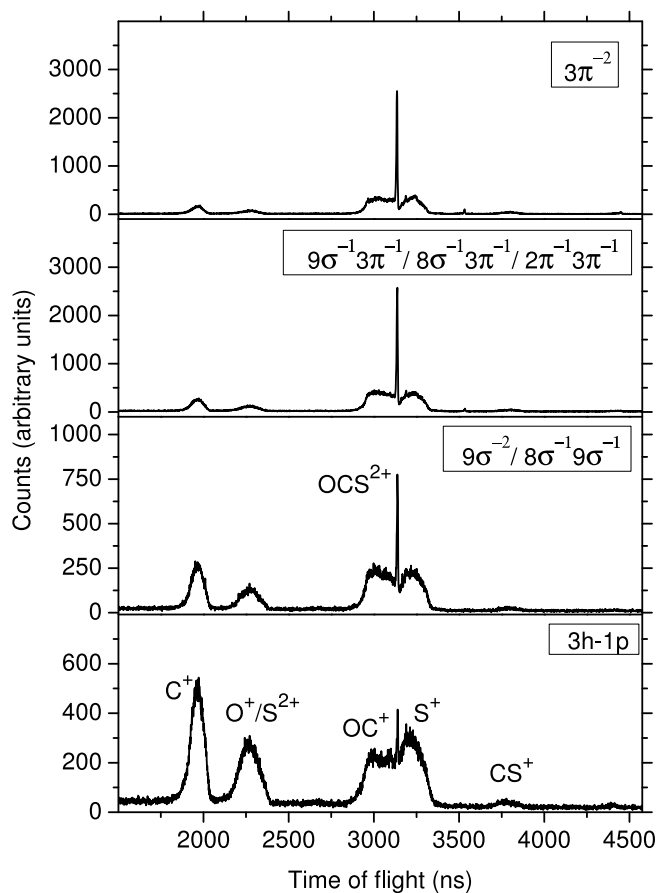


Figure 4.5: Time of flight spectra of OCS corresponding to different $S(2p)$ Auger decay states of the molecule.

The fragmentation channels of OCS^{2+} can be classified into two categories, (i) doubly ionized two body break-up where OCS^{2+} dissociates via $\text{OC}^+:\text{S}^+$ and $\text{O}^+:\text{CS}^+$ channels (ii) doubly ionized three body break-up in which OCS^{2+} completely dissociates into its atomic constituents giving rise to two charged and a neutral fragment through $\text{C}^+:\text{O}^+:\text{S}$, $\text{C}^+:\text{S}^+:\text{O}$ and $\text{O}^+:\text{S}^+:\text{C}$ channels. The fragmentation channels can be identified from the ion-ion coincidence map between ToF of first fragment and second one which is shown in Fig. 4.6 for various Auger excitations. The coincidence map for $3\pi^{-2}$ is not shown because this state is stable in nature and any fragment ions seen in the spectrum is due to contamination from higher binding energy states owing to moderate energy resolution of the CMA.

From the coincidence maps it is clear that the fragmentation of unstable OCS^{2+} from low binding energy Auger states is mainly via two body break-up. Three body break-up becomes prominent when higher energy Auger states are accessed since more excitation energy is required to break both the molecular bonds in OCS. This is direct evidence for three-body break-up requiring higher energy compared to a two-body break up. The appearance energy of $\text{OC}^+:\text{S}^+$ channel is about 34 eV [93]. Dissociation from $(9\sigma^{-1}3\pi^{-1}, 8\sigma^{-1}3\pi^{-1}, 2\pi^{-1}3\pi^{-1})$ Auger states gives the highest yield of the $\text{OC}^+:\text{S}^+$ channel. We find that among the two doubly ionized two body break-up channels, $\text{OC}^+:\text{S}^+$ is favoured over $\text{O}^+:\text{CS}^+$. This is a consequence of the difference in the two bonds in OCS^{2+} . It is postulated [94], that the O–C bond becomes stronger and C–S bond is weakened when double ionization of OCS takes place. So, break-up of C–S bond in OCS^{2+} is more probable, the manifestation of which is the higher yield of the $\text{OC}^+:\text{S}^+$ channel as compared to $\text{O}^+:\text{CS}^+$ channel upon dissociation of the transient molecular ion. Since more energy is required to break the strong O–C bond in OCS^{2+} , $\text{O}^+:\text{CS}^+$ channel opens when ionization to higher binding energy states occur providing the molecule with sufficient internal energy, required to break the O–C bond.

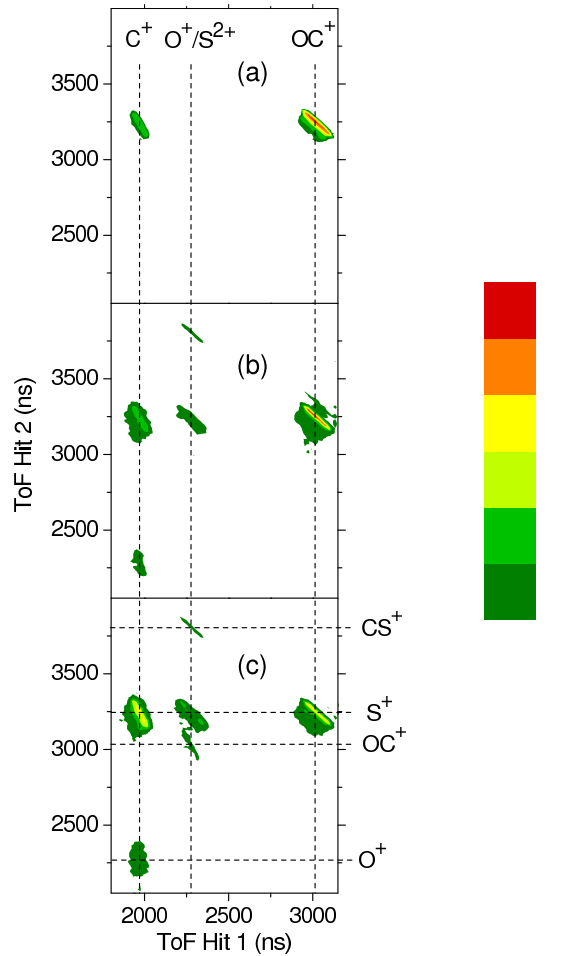


Figure 4.6: Ion-ion coincidence map of OCS corresponding to different Auger decay states: (a) $9\sigma^{-1}3\pi^{-1}$, $8\sigma^{-1}3\pi^{-1}$, $2\pi^{-1}3\pi^{-1}$, (b) $9\sigma^{-2}$, $8\sigma^{-1}9\sigma^{-1}$ and (c) $(3h - 1p)$. To bring out the relative cross-section of dissociation we have normalized the intensity in each panel to the yield of undissociated OCS^{2+} for the selected Auger state band. A common false colour intensity scale is used for all panels with intensity increasing from green to red. The data presented is above the threshold for false coincidence counts.

Three body fragmentation channels have an appearance energy of 42.5 eV [93]. In view of the moderate resolution of the electron spectrometer, we attribute the faint signature of $\text{C}^+:\text{S}^+:\text{O}$ dissociation channel arising from $(9\sigma^{-1}3\pi^{-1}$, $8\sigma^{-1}3\pi^{-1}$, $2\pi^{-1}3\pi^{-1})$ hole states (Figure 4.6 (a)) to a mixing from higher binding energy states. The ion pair coincidence map reveals that $\text{C}^+:\text{S}^+:\text{O}$ channel is most favoured three body dissociation channel, followed by $\text{O}^+:\text{S}^+:\text{C}$ and $\text{C}^+:\text{O}^+:\text{S}$ channels.

It is to be noted that the doubly ionized three-body break-up channel $C^+:O^+:S$ is indistinguishable from the triply ionized three-body break-up channel $C^+:S^{2+}:O$ because O^+ and S^{2+} have the same m/q ratio. Ankerhold *et.al.* [95] have proposed that the $m/q = 12, 16$ is due to the $C^+:S^{2+}:O$ channel whereas Erman *et.al.* [96] ascribe it to the $C^+:O^+:S$ channel. In other studies [97, 98] this channel is ignored due to the ambiguity. Our analysis favours the $C^+:O^+:S$ channel, based on the following arguments. In the ion-ion coincidence map we see that this coincidence island starts appearing upon ionization to $9\sigma^{-2}, 8\sigma^{-1}9\sigma^{-1}$ states (Fig. 3.5 b), which lie below the triple ionization threshold of OCS [99, 100]. Since the range of electron energies selected by our CMA is quite broad, the ion yield from the decay of the $(3h - 1p)$ states, may be contaminated by the fragmentation of triply ionized OCS. We do in fact, see faint signatures of $S^{2+}:CO^+$ due to the break-up of OCS^{3+} (Fig. 4.6 c). Triple ionization of OCS can occur through a double Auger decay. In one such study done with 180 eV photons [100], Eland *et.al.* report that triple ionization constitutes only 2% of the total ion yield and that the dissociation of triply ionized OCS is mostly through a two body break-up. This would imply, that the $S^{2+}:CO^+$ channel would dominate over $S^{2+}:C^+:O$ (three-body break-up). In our spectra the island corresponding to $m/q = 12, 16$ is far more intense than the island at $m/q = 16, 28$ (or $S^{2+}:CO^+$), suggesting that this three body fragmentation island is from a doubly ionized precursor rather than a triply ionized one. Absence of any signature of the other triply ionized three body break-up channel with S^{2+} as one of its fragments, namely $O^+:S^{2+}:C$, in our coincidence map is a further point in favour of identification of the channel at $m/q = 12, 16$ as $C^+:O^+:S$ channel rather than $C^+:S^{2+}:O$.

4.2.2 Auger decay and fragmentation channels of S($2p$) core ionized CS_2

CS_2 is a linear molecule and the ground state valence electronic configuration can be written as $5\sigma_g^2 4\sigma_u^2 6\sigma_g^2 5\sigma_u^2 2\pi_u^4 2\pi_g^4$ which arises due to bonding between carbon

2s 2p and sulphur 3s 3p orbitals. Ionization of the sulphur 2p orbital of CS₂ produces a core hole in the molecule. This triggers various S(2p) Auger decays and emission of Auger electrons leading to double electron removal from the valence shell of the molecule. The S(2p) Auger electron spectrum of CS₂ upon ionization by 171 eV (S 2p_{1/2} ionization threshold [101] of CS₂) photon beam is shown in Fig. 4.7. At this photon energy both the S(2p) orbitals may be ionized, thus the spectrum will have contribution from both S 2p_{1/2} and S 2p_{3/2} Auger decay. The raw spectrum is background subtracted and Gaussians are fitted with a correspondence with the features in the spectrum. Though the resolution of the spectrum is moderate, the broad features are identifiable by comparison with higher resolution S(2p) Auger spectra from the literature [102].

The binding energy of the state in question is obtained by subtracting the Auger kinetic energy from S 2p_{1/2} threshold. States other than (3h - 1p) are determined by a binding energy correspondence with the dominant dication states [103, 104]. Features having mean binding energy less than the threshold energy for double ionization (around 27 eV [105]) are marked as valence ionization since Auger transitions will always lead to double ionization. The (3h - 1p) states, as in the case of OCS, represents states corresponding to those ionization producing three holes in the molecular orbitals but one electron is excited into a virtual orbital rather than being ionized. It has been shown that (3h - 1p) states are dominant at higher binding energies [104].

Of the four groups of dication states identified from the electron spectrum, the 2π_g⁻² group of states are stable [103]. In the ToF spectrum, shown in Fig. 4.8, we observe a strong peak of CS₂²⁺ when triggered by electrons from this band of energies indicating that CS₂²⁺ remains mostly stable. The peaks corresponding to fragment ions for ionization to 2π_g⁻² state may be attributed to contamination from higher binding energy states, owing to the moderate resolution of the electron energy analyzer. The weak signals of N₂⁺ and O₂⁺ in the ToF spectrum is due to air contamination. Ion spectra triggered by electrons from the bands (6σ_g⁻²,

$5\sigma_u^{-2}$, $6\sigma_g^{-1}5\sigma_u^{-1}$) and $(3h-1p)$ lead to a weak CS_2^{2+} signal in the ToF spectrum, and various ion due to the fragmentation of CS_2^{2+} . Ionization to higher binding energy states leaves the molecular ion with higher internal energy required for bond breakage, thus we observe a increase in fragmentation for these cases. This has been observed earlier in some studies [102, 106]. A small CS_2^{3+} peak in the ToF spectrum for these dication states may be due to contributions from higher binding energy tricationic states which get partially mixed with dication states because of the CMA resolution.

To identify different fragmentation channels upon various Auger decays we look into the ion-ion coincidence map for each group of Auger decay states. Fig.

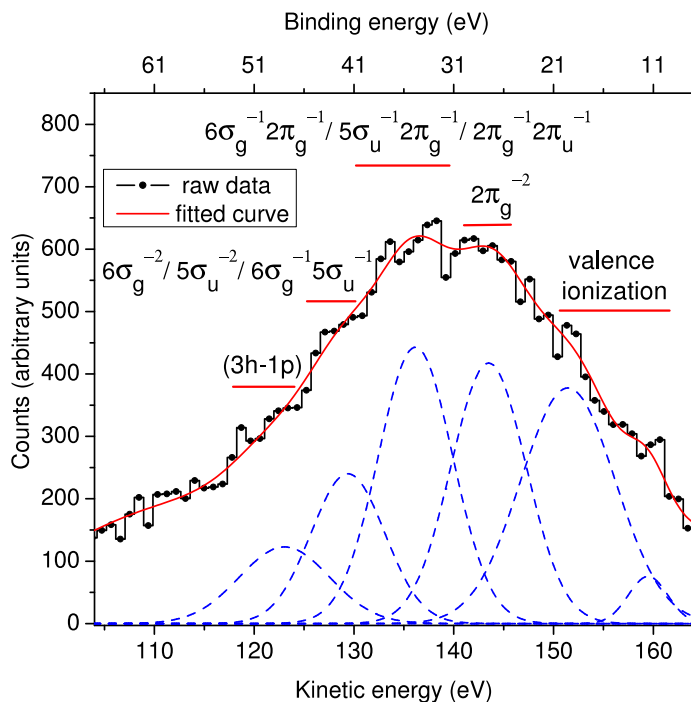


Figure 4.7: Broad features of the S($2p$) Auger electron spectrum of CS_2 . Features for both S $2p_{1/2}$ and S $2p_{3/2}$ Auger decay are contained in this spectrum. The histogram is raw data, the continuous (red) curve is the fitted sum of multiple Gaussian functions, which are shown individually by broken curves and correspond to the distribution of electrons from various Auger states. The broad features are identified following Hayes *et.al.* [102] and the dication states are determined following Lablanquie *et.al.* [103] and Millie *et.al.* [104]. The binding energy scale at the top is obtained by subtracting the Auger kinetic energy from S $2p_{1/2}$ threshold. Groups of close-lying doubly ionized states resulting from Auger decay are indicated by horizontal lines.

4.9 shows the ion-ion coincidence map between ToF of first fragment and second one, corresponding to various Auger states. The intense $S^+ : CS^+$ coincidence island for $(6\sigma_g^{-1}2\pi_g^{-1}, 5\sigma_u^{-1}2\pi_g^{-1}, 2\pi_g^{-1}2\pi_u^{-1})$ states suggests that for ionization to low binding energy states, only single bond breaks occur, leading to two body fragmentation of CS_2^{2+} . Infact the cross-section for $S^+ : CS^+$ dissociation channel is maximum for ionization to these binding energy states. The cross-section for two body break-up decreases as fragmentation occurs from higher binding energy states as can be seen in Fig. 4.9. Presence of another two body dissociation channel, namely $C^+ : S_2^+$, has been reported by Lavollée [107], we do not observe this channel in our experiment. The appearance energy threshold of the three body break-up channel $C : S^+ : S^+$ is 37 eV [108]. We see a faint signature of this channel ($S^+ : S^+$ island) for ionization to $(6\sigma_g^{-1}2\pi_g^{-1}, 5\sigma_u^{-1}2\pi_g^{-1}, 2\pi_g^{-1}2\pi_u^{-1})$

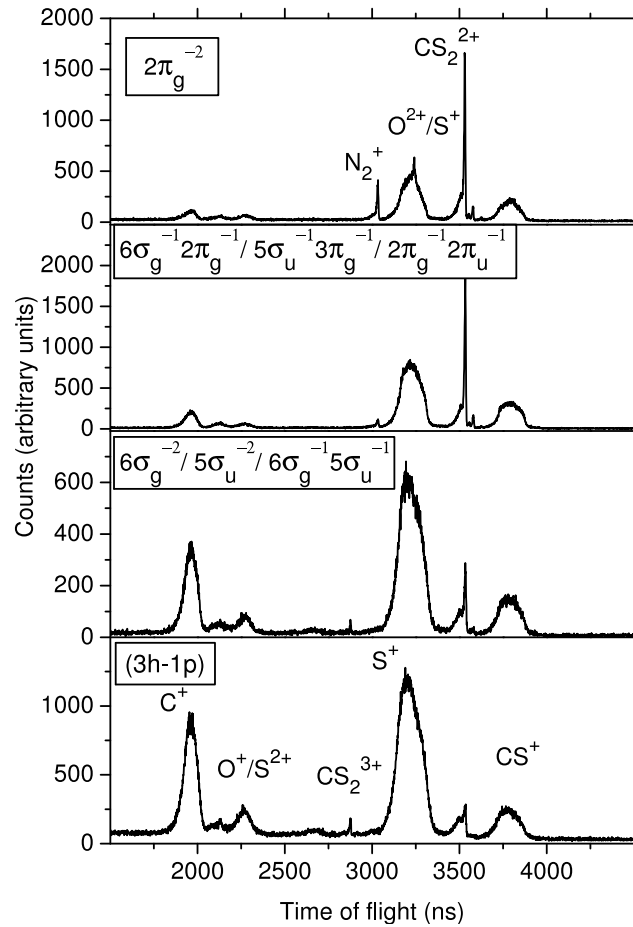


Figure 4.8: Time of flight spectra of CS_2 corresponding to different $S(2p)$ Auger decay states of the molecule.

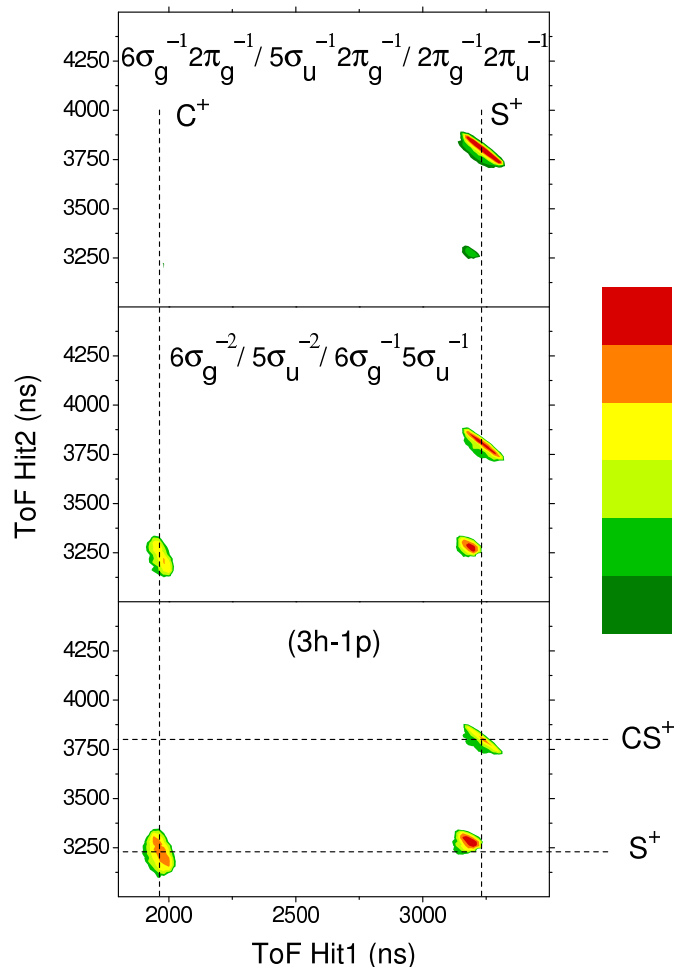


Figure 4.9: Ion-ion coincidence map of CS_2 corresponding to different final Auger states. The intensity is normalized for each panel. There is no intensity normalization across panels. A common false colour intensity scale is used for all panels with intensity increasing from green to red. The data presented is above the threshold for false coincidence counts.

states. The other three body fragmentation channel of CS_2^{2+} , $\text{C}^+:\text{S}^+:\text{S}$, has an appearance energy of 41 eV [108]. This channel begins to appear ($\text{C}^+:\text{S}^+$ island) for ionization to $(6\sigma_g^{-2}, 5\sigma_u^{-2}, 6\sigma_g^{-1}5\sigma_u^{-1})$ states. The cross-section for both the channels leading to complete atomization increases for dissociation from $(3h-1p)$ states. As it is evident, complete atomization of the molecule becomes dominant for ionization of higher binding energy orbitals. This is a direct consequence of the fact that more internal energy is required to break both the C–S bonds as compared to a single bond rupture. Adequate energy is only available to the molecular ions which are formed upon ionization to higher binding energy states. Hence, we see a gradual decrease in cross-section of two body break-up and an

increase in cross-section of three body break-up channels as we go from lower to higher binding energy states.

It is worth mentioning here that though Auger decay primarily leads to double ionization, triple ionization of CS_2 is also possible at this photon energy via double Auger decay as discussed by Eland *et.al.* [109]. Ankerhold *et.al.* [95] reports a branching ratio for CS_2^{3+} to be about 10% of the total ion yield for ionization by 174 eV photons. Lavollée [107] also observed triple ionization of CS_2 for ionization around S(2p) threshold. But these studies were conducted without any energy selection of emitted electron. The appearance energy of stable CS_2^{3+} is 53 eV [109] while that of the dissociative states will be even higher in energy. Since, the binding energy range of the states for which this study is conducted is below the appearance energy threshold of CS_2^{3+} , tricationic states will not be ideally accessed in our case. Infact, we do not see trication dissociation channel for any of the states except $(3h - 1p)$. A faint $\text{C}^+:\text{S}^+:\text{S}^+$ channel is observed in triple ion coincidence map (not shown here) for ionization to $(3h - 1p)$ states. Due to its moderate energy resolution, low kinetic energy electrons corresponding to ionization to trication states may get admitted into the CMA when it is tuned to collect Auger electrons for ionization to $(3h - 1p)$ dication states. The contribution of this channel in the $\text{C}^+:\text{S}^+$ island due to fragmentation of CS_2^{2+} is subtracted during analysis. Another possible source of contamination of the $\text{C}^+:\text{S}^+:\text{S}$ channel is from tricationic dissociation via $\text{C}^+:\text{S}_2^{2+}$ channel. These two channels cannot be distinguished from one another, but as we do not observe $\text{C}^+:\text{S}_2^+$ channel in the coincidence map, we assume $\text{C}^+:\text{S}_2^{2+}$ channel is also absent in our experiment. In general, the cross-section for triple ionization at this photon energy is small and as reported by Lavollée [107] the contamination of dicationic dissociation channel is not severe.

In summary, molecular ions formed with various electronic configurations upon different S(2p) Auger decay transitions triggered by core ionization exhibit different behaviour. Mostly dicationic molecular ions are produced due to

S($2p$) Auger decay of both OCS and CS₂. Stable molecular dications are formed when orbitals of lower binding energy are ionized as a result of Auger decay. The propensity towards production of unstable dicationic molecular ions and their subsequent dissociation increases upon ionization of higher binding energy orbitals. The energy gained by the molecular ion for ionization of low binding energy orbitals is insufficient to break the molecular bonds. On the other hand, as ionization to higher binding energy states occurs the molecular ion gains enough energy required for bond rupture, thus fragmentation inevitably follows. Complete atomization of the molecule is only achieved when sufficiently high excitation energy is gained by the molecule through ionization so as to break all its bonds. Thus, the cross-section of three body break-up of triatomic molecules like OCS and CS₂ is higher when dissociation from high binding energy states occur. Dissociation from low binding energy states favour two body break-up as lesser energy is needed to break the bond between two atoms in the molecule than all the molecular bonds.

The results indicate that, for the same ionizing agent (in this case photons of equal energy), it is the detail of the electron decay mechanism that governs the nature of the resulting molecular ion. Molecular ions formed with same charge may differ in their electronic configuration and may either be stable or dissociative in nature. The stability of the molecular ions formed is governed by the different excitation energy supplied to the molecule upon different electronic decays. The fragmentation pattern of the unstable molecular ion is also dependent on the energy gained by the molecule and thus is governed by the electronic decays leading to ionization of various orbitals.

4.3 Fragmentation kinematics of core ionized molecule

The results presented in the previous section reveal that the fragmentation pattern of the core ionized molecule depends on the Auger decays. Since various Auger decays result in different excitation energy being available to the molecular ion, the fragmentation kinematics of the unstable molecule may vary with different Auger decay. This section discusses the kinematical changes in fragmentation of core ionized molecules like OCS and CS₂ upon various S(2*p*) Auger decays. Kinematic parameters like momentum and kinetic energy of the fragments arising upon dissociation via various channels have been recorded for various Auger decay states indicated in the previous section. Relevant kinematic information has been extracted for each group of Auger decay states. We focus on the break-up mechanisms and kinetic energy release (KER) for various dissociation channels.

4.3.1 Break-up mechanisms of core ionized OCS and CS₂

The break-up mechanisms of molecules following various dissociation channels can be revealed by studying the corresponding island slopes in the ion-ion coincidence maps. From the coincidence maps for OCS and CS₂, shown in Fig. 4.6 and Fig. 4.9, the island slopes for the dissociation channels for each group of Auger decay states is computed. For a particular coincidence island corresponding to a fragmentation channel, the slope value is almost same for all the Auger states. This implies that the mechanism of dissociation does not change much with the electronic decay processes. As expected, the islands corresponding to two body break-up channels, namely, OC⁺:S⁺ and O⁺:CS⁺ for OCS and S⁺:CS⁺ for CS₂ have a slope of -1 due to equal momentum sharing among the fragments. Three-body break-ups can be concerted (*i.e.* simultaneous break of both bonds), or sequential, with various patterns in the sharing of charges. A sequential or two-step break-up, with one ion separated in the first step, and

the neutral separating from the second ion in the second step results in an island of slope $-(m_1 + m_n)/m_1$, or $-m_2/(m_2 + m_n)$ where m_1 and m_2 refer to the lighter and heavier ion, respectively, and m_n is the mass of the undetected neutral fragment. Of the two possibilities, only the first applies to the present case. A sequential break-up, in which the neutral fragment separates first, followed by separation of the ions results in an island of slope -1 , whose width is a measure of the momentum of the neutral fragment. Concerted break-up, *i.e.* simultaneous breaking of all bonds, on the other hand, may result in an island having slope of any value. In particular, it may result in an island of slope nearly -1 , if the neutral fragment has negligible momentum.

As is evident from Fig. 4.6, the three body break-up channels of OCS dication formed due to S(2p) Auger decay, have different island slopes. The $C^+:S^+(:O)$ island has a slope of -1.72 which is greater than the predicted slope for sequential break-up (which is -3.67) while the island slope for $C^+:O^+(:S)$ island is -4.61 which is less than the predicted slope for sequential break-up (which is -2.34). This indicates the possibility of a concerted break-up. The other three-body break-up, $O^+:S^+(:C)$, has an island slope of -0.97 . This dissociation channel also arises upon concerted break-up where the neutral fragment has a negligible momentum. It cannot be a two-step break-up, since the neutral fragment is at the central position in the parent molecule which cannot separate in the first step to give a OS^{2+} intermediate. The coincidence island slope values for three-body break-up channels of CS_2 dication, *viz.* $C^+:S^+:S$ and $S^+:S^+:C$, are obtained from ion-ion coincidence map for fragmentation of CS_2 shown in Fig. 4.9. The island slope of $C^+:S^+(:S)$ is -2.67 which is greater than the value predicted for sequential break-up (which is -3.67), thus indicating concerted dissociation. The slope of $S^+:S^+(:C)$ fragmentation island has a value of -1.1 , which also implies concerted break-up, the neutral fragment being at the central position of the molecule.

To visualize the break-up mechanisms in detail and map the pattern of mo-

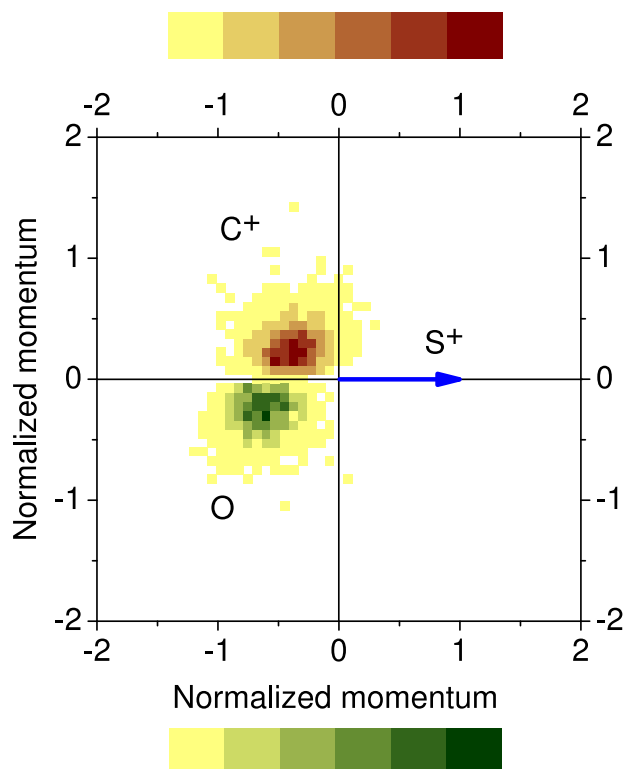


Figure 4.10: Newton diagram of $C^+:S^+:O$ fragmentation channel for $(3h - 1p)$ Auger state. Normalization of fragment momentum is done with respect to the momentum of S^+ . Normalized momentum distribution of the fragments are mapped with respect to S^+ , shown by the arrow along x -axis. The fragment carbon and the oxygen atom is shown in the upper and lower half of each plot respectively. The false colour intensity scale increases from light to dark.

momentum sharing among the fragments arising from three-body break-up, Newton diagrams are needed for each dissociation channel leading to complete atomization. The normalized momentum of each fragment is mapped in Newton diagram to yield the correlated momentum sharing of the fragments in molecular frame. The Newton diagrams for three body break-up channels of OCS^{2+} dication upon $S(2p)$ Auger decay resulting in $(3h - 1p)$ molecular ion states are presented. The Newton diagram for the three-body break-up from the $(9\sigma^{-2}, 8\sigma^{-1}9\sigma^{-1})$ Auger state has also been studied, and a similar break-up mechanism emerges in either case. Fig. 4.10 shows the Newton diagram for $C^+:S^+:O$ channel, while Fig. 4.11 and Fig. 4.12 is the same for $C^+:O^+:S$ and $O^+:S^+:C$ dissociation channels respectively. Here, the momentum of the fragment ion and the neutral fragment is normalized and mapped with respect to the other fragment ion. The latter is

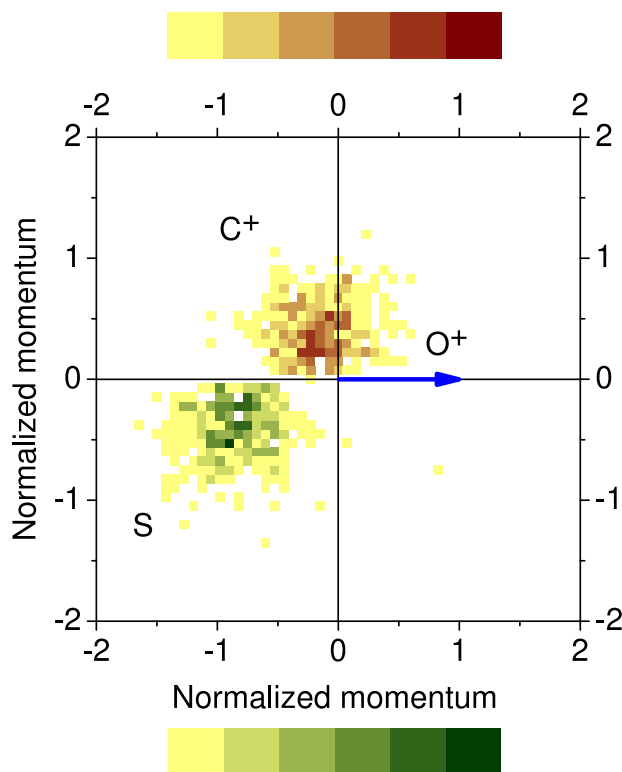


Figure 4.11: Newton diagram of $C^+:O^+:S$ fragmentation channel for $(3h - 1p)$ Auger state. Normalization of fragment momentum is done with respect to the momentum of O^+ . Normalized momentum distribution of the fragments are mapped with respect to O^+ , shown by the arrow along x -axis. The fragment carbon and the sulphur atom is shown in the upper and lower half of each plot respectively. The false colour intensity scale increases from light to dark.

shown as a vector of unit magnitude along the x -axis. The normalized momentum of the carbon fragment always appears on the upper half of the plot and on the lower half, normalized momentum of either oxygen or sulphur fragment is mapped as indicated in the plots. For $C^+:S^+:O$ channel (see Fig. 4.10), we see that S atom carries the largest momentum, while for the $C^+:O^+:S$ channel (see Fig. 4.11) the momenta of S and O atoms are comparable. For both channels, the carbon fragment has the least momentum, but is not negligible. Concerted fragmentation from linear precursor molecular ion (ground state OCS has a linear geometry) would ideally lead to a zero momentum gain of the carbon atom. The momentum gain for the carbon fragment is negligible for fragmentation via $O^+:S^+:C$ channel, as observed in the Newton diagram shown in Fig. 4.12. This may be due to break-up from a precursor molecular ion which is mostly linear

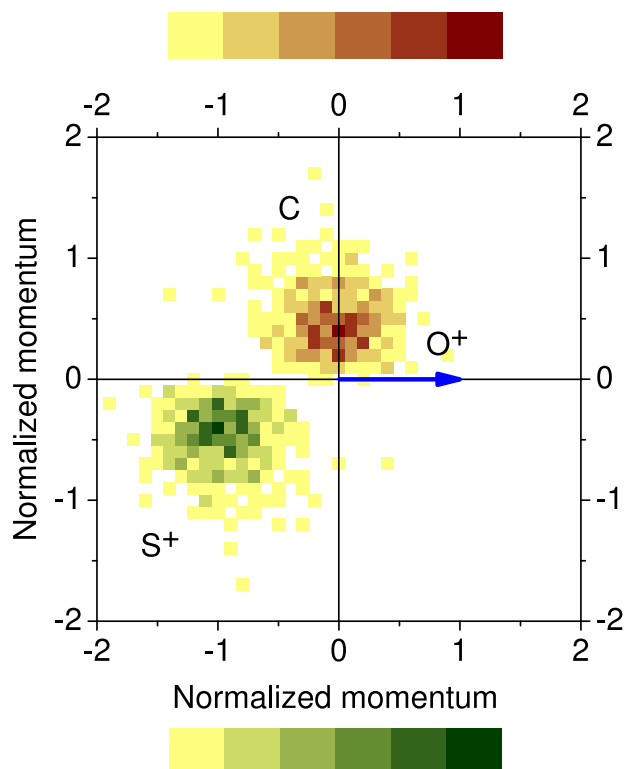


Figure 4.12: Newton diagram of $O^+:S^+:C$ fragmentation channel for $(3h - 1p)$ Auger state. Normalization of fragment momentum is done with respect to the momentum of O^+ . Normalized momentum distribution of the fragments are mapped with respect to O^+ , shown by the arrow along x -axis. The fragment carbon and the sulphur atom is shown in the upper and lower half of each plot respectively. The false colour intensity scale increases from light to dark.

in geometry. In the case of sequential fragmentation, the distribution of the momenta shows a semicircular feature. This is attributed to the rotation of the diatomic intermediate before it breaks up, as observed in the case of CO_2^{3+} by Neumann et al. [72]. This feature is not visible in the momentum maps shown here. The only possibility is that $C^+:S^+:O$ and $C^+:O^+:S$ break-ups are due to concerted dissociation of the OCS^{2+} molecular ion in a bent geometry while for dissociation via $O^+:S^+:C$ channel, OCS^{2+} mostly retains its linear geometry.

An alternative mechanism for three body fragmentation of OCS^{2+} has been proposed by Yoshiki Franzén *et.al.* [110]. Based on a simulation and its agreement with the experimentally observed ion-ion coincidence island slope, they infer the dissociation mechanism to be a quasi two-step process where, after the

first bond break yielding a charged ion and a charged diatomic species, the diatomic species fragments within the Coulomb field of the charged ion. Although this fragmentation mechanism is a valid possibility, the KER for which these simulations yielded agreement with experimental data are high (14–20 eV for $O^+:S^+:C$ channel and 14–18 eV for $C^+:S^+:O$ channel). The most probable as well as mean KER for these channels in our experiment are lower than these values (see section 4.3.2). In the view of this, it is possible that OCS^{2+} undergoes either instantaneous break-up or quasi two-step break-up depending upon the precursor molecular ion state from which the dissociation occurs.

The Newton diagram for $C^+:S^+:S$ and $S^+:S^+:C$ channel due to $S(2p)$ Auger decay of CS_2 yielding $(3h-1p)$ states are shown in Fig. 4.13 and Fig. 4.14 respec-

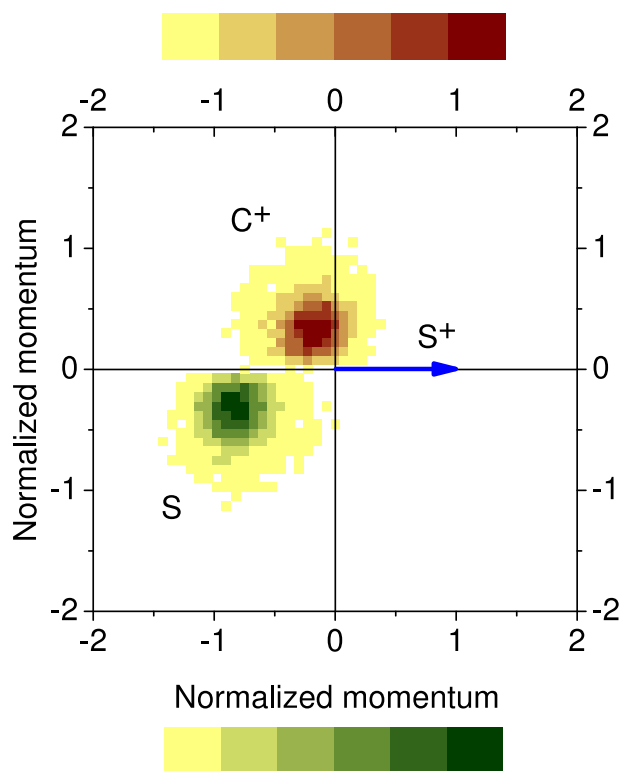


Figure 4.13: Newton diagram of $C^+:S^+:S$ fragmentation channel for $(3h-1p)$ Auger state. Normalization of fragment momentum is done with respect to the momentum of S^+ . Normalized momentum distribution of the fragments are mapped with respect to S^+ , shown by the arrow along x -axis. The fragment carbon and the sulphur atom is shown in the upper and lower half of each plot respectively. The false colour intensity scale increases from light to dark.

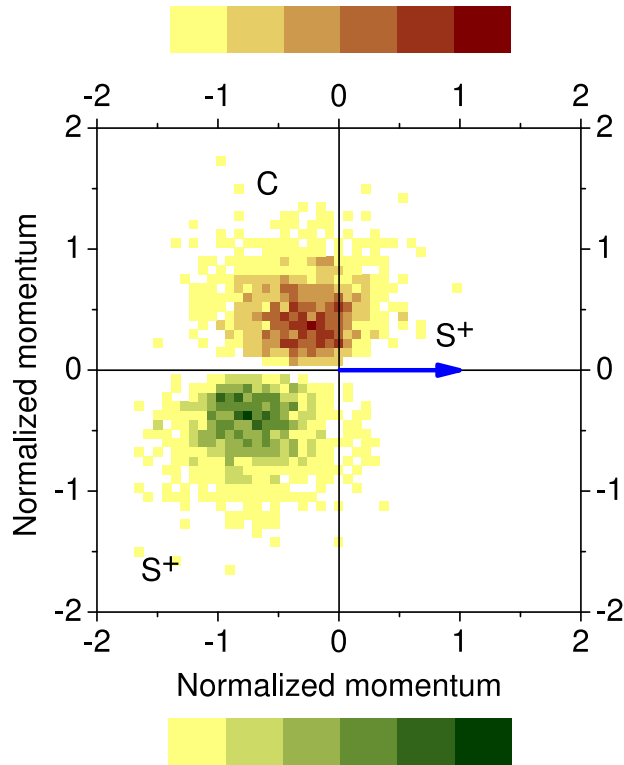


Figure 4.14: Newton diagram of $S^+:S^+:C$ fragmentation channel for $(3h - 1p)$ Auger state. Normalization of fragment momentum is done with respect to the momentum of second S^+ fragment to be detected. Normalized momentum distribution of the fragments are mapped with respect to the second S^+ fragment to be detected, shown by the arrow along x -axis. The fragment carbon and the sulphur atom is shown in the upper and lower half of each plot respectively. The false colour intensity scale increases from light to dark.

tively. For both channels, the momentum of the second fragment (S^+) is taken as the reference and shown as a unit vector along x -axis, while the momenta of the two other partners are normalized with respect to the second fragment and are mapped in the upper and lower half of the diagram respectively. We have studied the fragmentation mechanisms of $C^+:S^+:S$ and $S^+:S^+:C$ channels for both $(6\sigma_g^{-2}, 5\sigma_u^{-2}, 6\sigma_g^{-1}5\sigma_u^{-1})$ and $(3h - 1p)$ Auger states and they are found to exhibit similar behaviour. The absence of any semi-circular feature in the Newton maps rules out the possibility of sequential break-up for both the channels. This is in contrast to some earlier reports which suggests a sequential break-up based on ion-ion coincidence island slope for CS_2^{2+} dissociation upon $S(2p)$ Auger decay [95] as well as upon valence ionization [111]. Furthermore, non-zero momentum

of the C and C⁺ in the two channels suggests that three-body break-up of CS₂²⁺ is mostly from bent states.

For both the molecules, the dissociation mechanism is independent of the Auger decay process. Dissociations leading to complete atomization of OCS and CS₂ dication are concerted in nature. These dissociations occur mostly from bent dicationic precursor molecular ions with the exception of O⁺:S⁺:C channel in which case the precursor OCS²⁺ retains its linear geometry.

4.3.2 Kinetic energy release upon fragmentation of OCS and CS₂ due to various S(2p) Auger decays

Various Auger decays produce Auger electrons with different energies thus providing the molecule with different excitation energy (see equation 4.2). This excitation energy is stored as the internal energy of the molecular ion formed due to ionization. The internal energy of excited molecular ion can be dissipated by processes such as radiative decay, internal conversion etc. For the case when unstable molecular ions are formed and dissociation occur, the internal energy is shared as the internal energy and/or kinetic energy of the fragments formed. The measure of the total kinetic energy of all the fragments produced upon dissociation gives the amount of internal energy of the precursor molecular ion being released in the form of kinetic energy. This is termed as kinetic energy release (KER). Since, the internal energy of the molecular ion states attained, upon various Auger decay, is different, so should be the energy dissipation mechanisms like KER for each Auger decay state. The KER distribution of the fragmentation channels formed upon dissociation of OCS and CS₂ due to various S(2p) Auger decay is reported in this section.

The kinetic energy release (KER) upon fragmentation of OCS²⁺ formed upon S(2p) have been studied earlier. Ankerhold *et.al.* [95] computed the maximum kinetic energy of fragment ions of OCS upon dissociative ionization by 183 eV

photons from their ToF peak widths. Their maximum kinetic energies for OC^+ and S^+ are 3.3 eV and 2.4 eV, respectively, giving the maximum KER value for $\text{OC}^+:\text{S}^+$ as 5.7 eV. In another photoionization study at similar photon energy, Yoshiki Franzén *et.al.* [110] have extracted the KER information from the coincidence island corresponding to the $\text{OC}^+:\text{S}^+$ channel. Their reported mean KER is 8 eV, in disagreement with Ankerhold *et.al.* In our experiment, since we have the complete information of all the momenta components of the ions in a dissociation event, KER information can be directly obtained from experimental data. Further, the energy selection of ejected electrons allows us to study the KER distribution corresponding to different Auger states of the precursor.

The KER distribution for two body break-up channels of OCS^{2+} is shown in Fig. 4.15 (a) for different bands of Auger decay states. There is a gradual increase in the mean KER value as we go from lower to higher binding energy

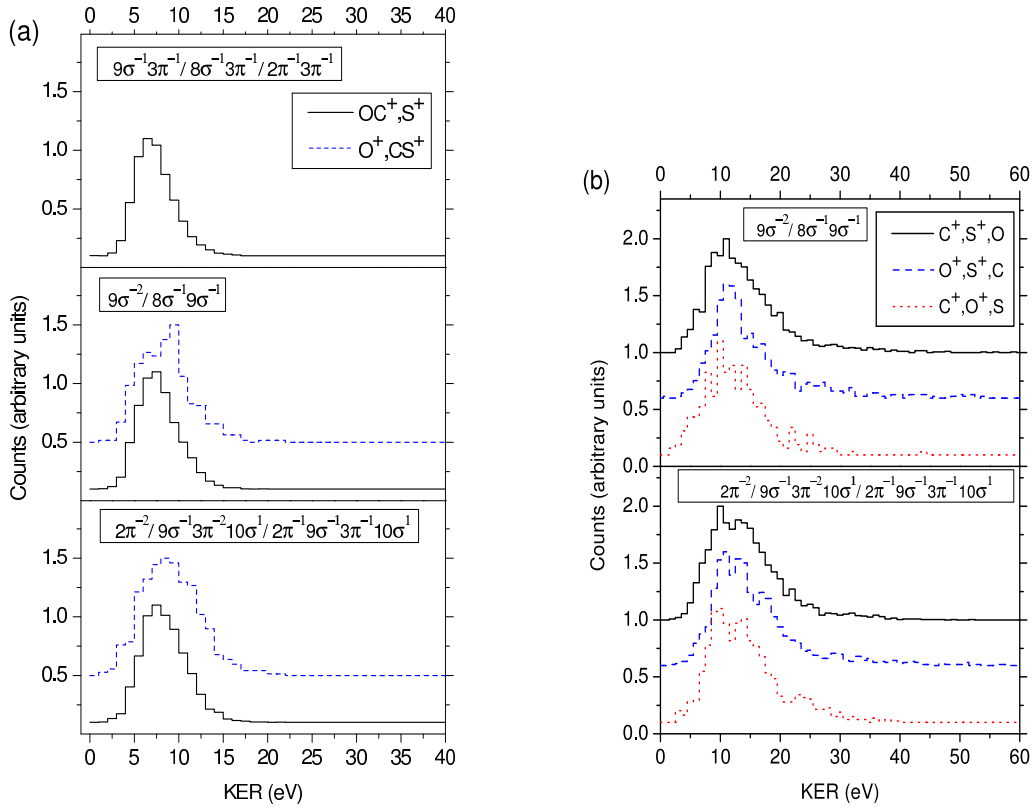


Figure 4.15: Kinetic energy release (KER) distribution for (a) two body break-up and (b) three body break-up channels of OCS^{2+} corresponding to various final Auger states. Curves are offset for clarity.

Channel	Previous studies		This work (mean values)		
			(i)	(ii)	(iii)
S ⁺ :CS ⁺	(a)	5.7 (max)	6.3±0.46	6.9±0.46	7.3±0.46
	(b)	8.0 (mean)			
O ⁺ :CS ⁺		—	—	7.6±0.46	8.3±0.46
C ⁺ :S ⁺ :O		—	—	12±0.65	12.7±0.65
C ⁺ :O ⁺ :S		—	—	11.9±0.65	12.3±0.65
O ⁺ :S ⁺ :C		—	—	11.5±0.65	13.1±0.65

Table 4.1: KER values (in eV) for different dissociation channels of OCS²⁺. KER values from previous studies by, (a) Ankerhold *et.al.* [95] and (b) Yoshiki Franzén *et.al.* [110] are presented. These studies had no electron energy selection. Mean KER values from our study for (i) $9\sigma^{-1}3\pi^{-1}$, $8\sigma^{-1}3\pi^{-1}$, $2\pi^{-1}3\pi^{-1}$ (ii) $9\sigma^{-2}$, $8\sigma^{-1}9\sigma^{-1}$ and (iii) $(3h - 1p)$, Auger states are also presented.

Auger states. For, OC⁺:S⁺ channel, the mean KER values are 6.3 eV, 6.9 eV and 7.6 eV for lower to higher energy Auger states as indicated in Fig. 4.15 (a). The mean value of KER for O⁺:CS⁺ channel are 7.6 eV and 8.3 eV for ionization to the $(9\sigma^{-2}, 8\sigma^{-1}9\sigma^{-1})$ and $(3h - 1p)$ Auger state respectively. A gradual increase in mean KER and KER range with increasing binding energy of the Auger decay states is also seen for various three body break-up channels of OCS²⁺ dication (Fig. 4.15 (b)). The mean KER value of C⁺:S⁺:O channel for $(9\sigma^{-2}, 8\sigma^{-1}9\sigma^{-1})$ states is 12 eV and for $(3h-1p)$ Auger states the value is 12.7 eV, whereas, the mean KER value of O⁺:S⁺:C and C⁺:O⁺:S channel are 11.5 eV and 11.9 eV for $(9\sigma^{-2}, 8\sigma^{-1}9\sigma^{-1})$ Auger states and 12.3 eV and 13.1 eV for $(3h - 1p)$ Auger states respectively. The KER values obtained in our experiment along with the values reported in some previous studies are summarized in Table 4.1

The increase in mean KER may be due to the excitation of OCS²⁺ to higher lying repulsive molecular ion states following ionization of deep lying electronic levels of the neutral molecule. These states may then dissociate directly or pre-dissociate [94], yielding higher KER values than in the case of dissociation from

lower molecular ion states that are accessed following ionization of weakly bound electronic states. But, the increase in mean KER is small with respect to the energy gained by the molecular dication due to ionization to high binding energy Auger states. This points to the possibility that most of the energy of OCS^{2+} is stored as internal energy of the fragments rather than being distributed as their kinetic energy thereby yielding lower KER upon dissociation. Radiative decay of a higher lying state into a lower lying less repulsive dissociative state may also give low KER, but the probability of radiative decay in OCS is found to be negligible in a previous study [94]. The mean KERs as well as the KER range are higher than that obtained in the case of valence photo double ionization of OCS, reported by Masuoka *et.al.* [97]. This shows clearly, that a different set of molecular ion states is accessed following ionization by Auger decay than in the case of valence ionization.

The KER distribution for various Auger state bands of CS_2 upon $\text{S}(2p)$ Auger decay is presented in Fig. 4.16. Studies employing various methods to obtain the kinetic energy from ToF spectra of the fragments ions arising from dissociation of CS_2^{2+} formed due to $\text{S}(2p)$ Auger decay have been done earlier. Hayes and Eberhardt [102] fitted the ion-ion coincidence spectra with various Gaussian kinetic energy release distributions and predicted the center kinetic energy for different dissociation channels. For example, for $\text{S}^+:\text{CS}^+$ channel the major distribution is reported to be centered at 4.1 eV. Alkemper and von Busch [106] reported a maximum KER for this channel as 4.5 eV by extracting the kinetic energy information from fragment ion ToF peak widths. In yet another study, von Busch [112] derived the mean kinetic energy of ion fragments from the variance of their coincidence ToF peak. For the $\text{S}^+:\text{CS}^+$ channel the mean KER is observed to be a little higher than the previous two reports. Employing a similar technique as ours but without any electron energy discrimination, Lavollée reported a peak KER value for $\text{S}^+:\text{CS}^+$ channel as 4.5 eV [107]. Due to the electron energy discrimination, we can provide KER information for various Auger state bands. For $\text{S}^+:\text{CS}^+$ channel the mean KER values corresponding to

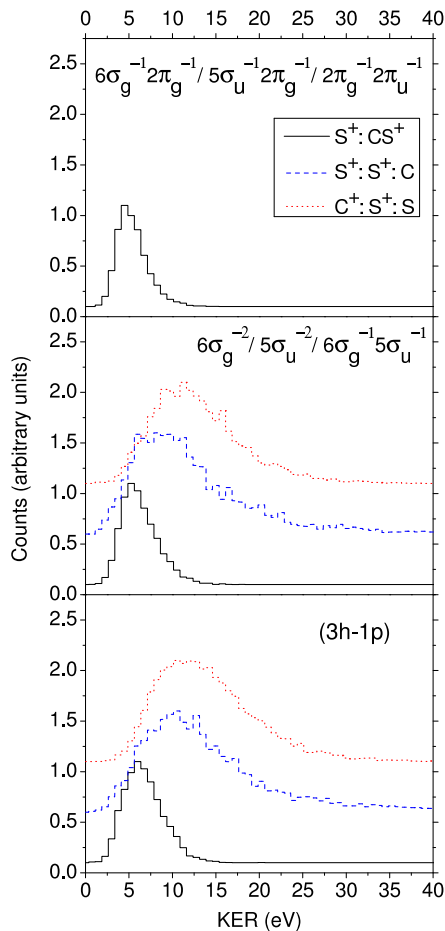


Figure 4.16: Kinetic Energy Release (KER) distribution of various fragmentation channels of CS_2^{2+} corresponding to different final Auger states. Continuous (black) curve represents $\text{S}^+:\text{CS}^+$ channel, broken (blue) curve denotes $\text{S}^+:\text{S}^+:\text{C}$ channel while dotted (red) signifies $\text{C}^+:\text{S}^+:\text{S}$ channel. Curves are offset for clarity.

dissociation from $(6\sigma_g^{-1}2\pi_g^{-1}, 5\sigma_u^{-1}2\pi_g^{-1}, 2\pi_g^{-1}2\pi_u^{-1})$, $(6\sigma_g^{-2}, 5\sigma_u^{-2}, 6\sigma_g^{-1}5\sigma_u^{-1})$ and $(3h-1p)$ Auger states are 5 eV, 5.8 eV and 6.4 eV, respectively. These values are closer to the report by von Busch [112] and also show an increasing trend in mean kinetic energy with decrease in the Auger electron energy, similar to that observed by von Busch. The KER value obtained in our experiment along with the value reported in some previous studies is summarized in Table 4.2. The maximum KER for each fragmentation channel remains same irrespective of the Auger state, but an increase in mean KER value is observed for dissociations from lower and higher binding energy states. The mean KER value for $\text{S}^+:\text{S}^+:\text{C}$ channel is 9.6 eV, 11.2 eV and for $\text{C}^+:\text{S}^+:\text{S}$ channel is 12 eV and 12.74 eV upon dissociation from $(6\sigma_g^{-2}, 5\sigma_u^{-2}, 6\sigma_g^{-1}5\sigma_u^{-1})$ and $(3h-1p)$ Auger states respectively.

Channel	Previous studies	This work (mean values)			
		(i)	(ii)	(iii)	
S ⁺ :CS ⁺	(a)	4.1 (mean)	5±0.46	5.8±0.46	6.4±0.46
	(b)	4.5 (max)			
	(c)	3.4 -7.3(mean)			
	(d)	4.5 (peak)			
C ⁺ :S ⁺ :S	—	—	12±0.65	12.74±0.65	
S ⁺ :S ⁺ :C	—	—	9.6±0.65	11.2±0.65	

Table 4.2: KER values (in eV) for different dissociation channels of CS₂²⁺. KER values from previous studies by, (a) Hayes and Eberhardt [102] (b) Alkemper and von Busch [106] (c) von Busch [112] and (d) Lavollée [107], are presented. All the studies, other than case (c), had no electron energy selection. For case (c), mean KER is derived by summing the mean kinetic energies of fragments and the range within which the KER value varies for different Auger electron energy is given. Mean KER values from our study for (i) $6\sigma_g^{-1}2\pi_g^{-1}$, $5\sigma_u^{-1}2\pi_g^{-1}$, $2\pi_g^{-1}2\pi_u^{-1}$ (ii) $6\sigma_g^{-2}$, $5\sigma_u^{-2}$, $6\sigma_g^{-1}5\sigma_u^{-1}$ and (iii) $(3h - 1p)$, Auger states are also presented.

As in the case for OCS, the increase in mean KER value with increasing binding energy of the Auger state may be attributed to the increase in probability of the molecule being excited to higher energy more repulsive molecular ion states upon ionization from highly bound electronic states, thus yielding higher KER upon dissociation. But, the mean kinetic energy of the fragments does not increase significantly with the increase in the internal energy gained by CS₂²⁺ due to ionization of higher binding energy orbitals. This, as pointed out in the earlier works [102, 106], indicates the possibility that most of the precursor ion energy goes into the internal energy (electronic excitation) of the fragments rather being converted into their kinetic energy. Another possible scenario may be radiative decay of the excited dication state into lower dissociative states hence yielding lower KER in the process.

Our observations suggests that, for all dication fragmentation channels formed upon various $S(2p)$ Auger transitions, the mean KER increases (but not significantly) for dissociation following ionization to higher binding energy Auger states. This points towards the possibility that though the dicationic molecular ion gains more energy as highly bound orbitals are ionized due to Auger decay, most of the parent molecular ion energy is partitioned as internal energy of the fragment ions than as their kinetic energy. Alternatively, the energy of the excited dication may also be expelled in the form of photons thus yielding lower KER upon dissociation. Nevertheless, the results discussed here show that the kinematics of fragmentation vary with the electronic decay mechanisms.

4.4 Conformation of the transient molecular ion and its effect on fragmentation kinematics

It has been observed that the excited molecular ion does not retain the ground state geometry of the molecule. Changes in precursor molecular ion geometries have been observed for three body break-up of molecules [113]. Since the fragmentation mechanism depends on the molecular ion state from which the dissociation occur, it would be interesting to know whether the precursor molecular ion conformation affects the dissociation kinematics. We focus on the three-body break-up channels ($C^+:S^+:S$ and $S^+:S^+:C$) of CS_2^{2+} due to ionization to highest binding energy Auger states (*i.e.* $(3h - 1p)$ Auger state band) as the propensity to complete atomization is the highest for this case. Dissociation from other Auger states has also been studied and they yield similar results.

Dalitz plots are employed to investigate the conformal changes in the precursor molecular ion at the instant of break-up. Following equation 3.3 (see Chapter 3), the Dalitz plot co-ordinates for CS_2 molecule can be written as,

$$\begin{aligned}
 \text{DalitzX} &= \sqrt{\frac{M}{m_C} \frac{E_{S_1} - E_{S_{2,N}}}{3E}} \\
 \text{DalitzY} &= \frac{M}{m_S} \frac{E_C}{3E} - \frac{1}{3}
 \end{aligned}
 \tag{4.3}$$

where, M is the mass of the molecule, m_S and m_C are masses of sulphur and carbon atom respectively. E_{S_1} is the kinetic energy of the first sulphur fragment to be detected and $E_{S_{2,N}}$ is the same for the second sulphur atom either singly charged or neutral as the case may be. E_C is the kinetic energy of carbon atom and E is the total KER from the fragmentation process. Each point in the Dalitz plot represents a certain momentum vector geometry of the CS_2^{2+} precursor ion at the time of break-up as illustrated in Fig. 4.17 (a) for a few points.

The Dalitz plots for three body fragmentation via $\text{C}^+:\text{S}^+:\text{S}$ and $\text{S}^+:\text{S}^+:\text{C}$ channels are shown in Fig. 4.17 (b) and Fig. 4.17 (c) respectively. In its ground state configuration, CS_2 is a linear molecule belonging to the $D_{\infty h}$ point group. For $\text{C}^+:\text{S}^+:\text{S}$ fragmentation we see that not only does the precursor ion mostly have a bent geometry as indicated earlier by the non-zero momentum of C^+ , but also there is an asymmetric stretch of the C^+-S^+ bond in many cases prior to break-

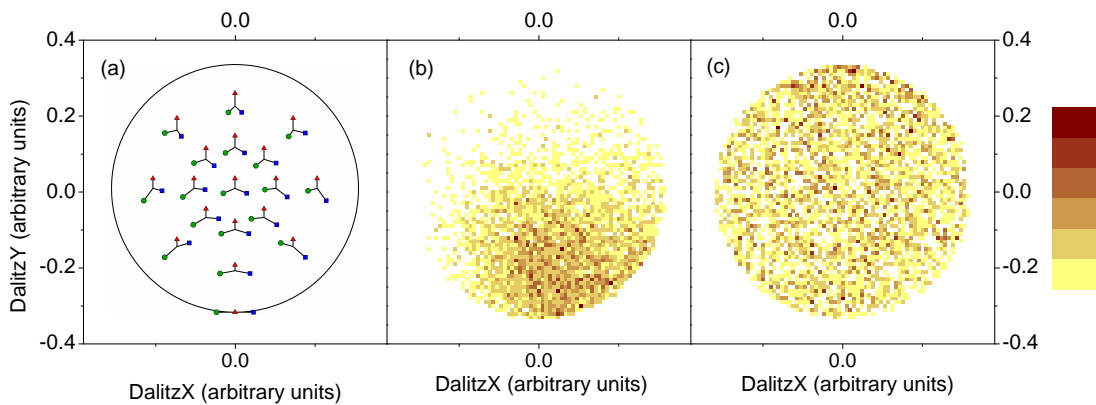


Figure 4.17: (a) Characteristic momentum vector geometry of CS_2^{2+} precursor ion in Dalitz plot. \blacktriangle denotes the momentum of the carbon ion, while \blacksquare marks the momentum of the first sulphur fragment to be detected. \bullet gives the momentum of the other sulphur atom either singly charged or neutral as the case may be (b) Dalitz plot for $\text{C}^+:\text{S}^+:\text{S}$ channel and (c) Dalitz plot for $\text{S}^+:\text{S}^+:\text{C}$ channel. The fragmentation channels are for $(3h - 1p)$ Auger ionizations only. The colour bar indicates intensity, increasing from light to dark.

up. Thus the CS_2^{2+} precursor ion belongs to either C_{2v} (for bending only) or C_s (for bending with asymmetric stretch of the $\text{C}^+ - \text{S}^+$ bond) point group. The Dalitz plot for $\text{S}^+:\text{S}^+:\text{C}$ channel on the other hand suggests that the fragmentation occurs from precursor ions having all possible geometries *i.e.* any bond angle is possible. Since the changes in geometry are likely to affect the KER, we look into Dalitz plots for different kinetic energy ranges.

The KER range A and B for $\text{C}^+:\text{S}^+:\text{S}$ channel is from 0–17 eV and 17–40 eV respectively. The selection of the range is arbitrary and is chosen such that KER range A spans from zero to a few eV above the modal KER, while KER range B covers the higher energy tail part. Fig. 4.18 (a) and (b) show the Dalitz plots for the two KER ranges while Fig. 4.18 (c) depicts the angle between the momenta of S^+ and S fragments for both the KER ranges for the same channel. For this channel, it is clear that dissociations yielding lower KER are due to precursor molecular ions in which the $\text{C}^+ - \text{S}^+$ bond is asymmetrically stretched. For higher KER range, which may arise due to dissociation from repulsive molecular ion states of higher energy, no asymmetric bond stretching occurs. The bending of the molecule is similar in the two cases as can be seen in Fig. 4.18 (c).

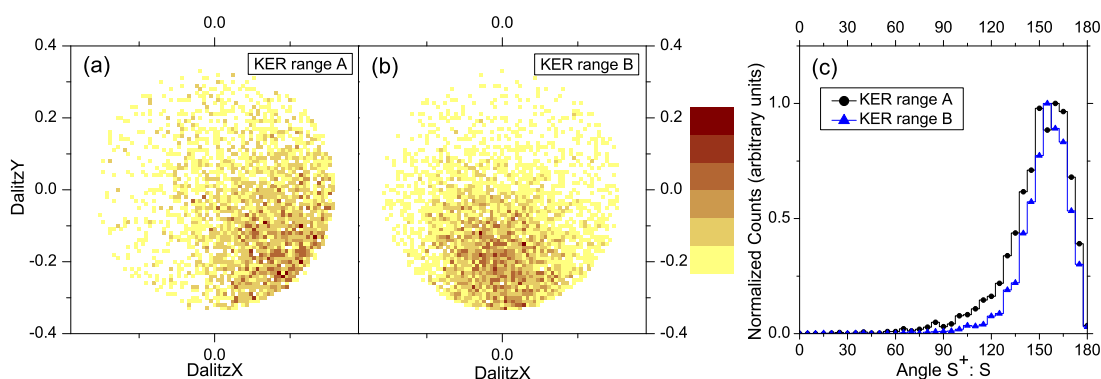


Figure 4.18: (a) Dalitz plot of $\text{C}^+:\text{S}^+:\text{S}$ for KER range A and (b) for KER range B. (c) Angle between momentum vectors of S^+ and S fragments upon $\text{C}^+:\text{S}^+:\text{S}$ break-up. The fragmentation channels are for $(3h - 1p)$ Auger ionizations only. The colour bar indicates intensity, increasing from light to dark.

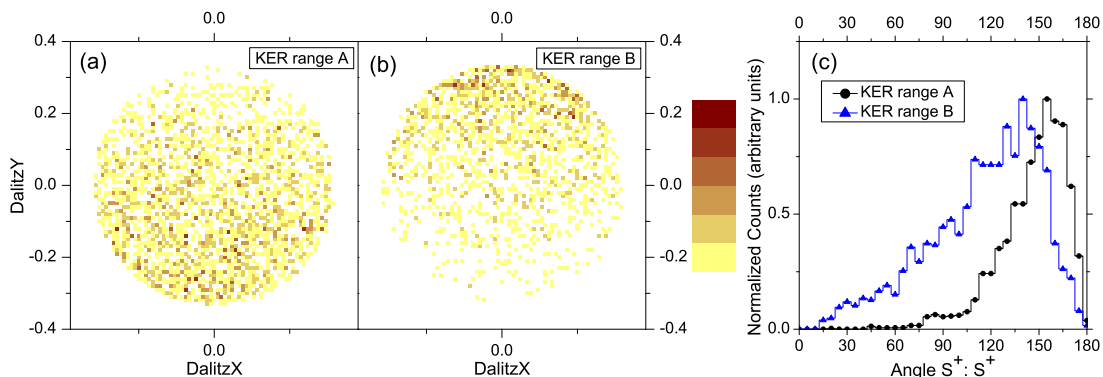


Figure 4.19: (a) Dalitz plot of $S^+:S^+:C$ for KER range A and (b) for KER range B. (c) Angle between momentum vectors of S^+ and S^+ fragments upon $S^+:S^+:C$ break-up. The fragmentation channels are for $(3h - 1p)$ Auger ionizations only. The colour bar indicates intensity, increasing from light to dark.

For the fragmentation channel $S^+:S^+:C$, KER range A is 0–14 eV while KER range B is 14–40 eV respectively. Again, the KER range is so chosen that KER range A spans from zero to a few eV above the modal KER, while KER range B covers the higher energy tail part. The KER range dependent Dalitz plots and the angle between momentum vectors of the two sulphur atoms for $S^+:S^+:C$ break-up is shown in Fig. 4.19 (a),(b) and (c). As can be seen in the Dalitz plots, irrespective of the KER range, the molecular ion can just be bent or there may be bending along with symmetric or asymmetric stretching of both the C– S^+ bonds of CS_2^{2+} precursor leading to $S^+:S^+:C$ channel. Kinematic differences depending on the degree of bending of the molecular ion are observed. Both the Dalitz plots and the angular correlation of the sulphur atoms indicate that fragmentation from molecular ions which have a less bent geometry lead to lower KER as compared to those with highly bent geometries.

We observe that the geometry of the excited molecular ion may be drastically different from its ground state conformation. For $S(2p)$ core ionized CS_2 , the conformation of the transient CS_2^{2+} dication leading to different fragmentation channels may be different from each other. The conformational changes in the precursor molecular ion affect the kinematics of dissociation. In a simplified pic-

ture, this can be attributed to different Coulomb repulsion experienced by the atoms in the molecular ion for various conformation attained. With the change in conformation of the molecular ion, the relative distances between the atoms in the molecule also changes. Thus the Coulomb repulsion among them also changes, leading to very different kinetic energy of the fragment ions. Hence, the KER upon fragmentation varies with the conformal changes in the molecular ion. Theoretical calculations are clearly needed to identify the molecular ion states in non-linear conformations that lead to the observed KER values.

Chapter 5

Summary and Future Directions

5.1 Summary

This thesis reports an experimental investigation of the fragmentation kinematics of molecular ions corresponding to various electron relaxation processes triggered by valence and core ionization molecules. Ionization was effected in our experiments using photon beams of specific energy. Valence shell ionization and the subsequent molecular dissociation was studied for the CO molecule. Valence shell ionization mostly led to singly charged molecular ion. Our study indicates that ionization of low binding energy valence orbitals in a molecule results in formation of stable singly charged molecular ion. The propensity towards dissociation increases as highly bound valence orbitals are ionized. The energy available to the molecular ion formed upon ionization of higher binding energy orbital is more than that in the case of ionization of low binding energy orbital. Hence, molecular bonds may be easily broken in the former scenario than in the latter case.

The probability of fragmentation increases with the charge state of the molecular ion formed due to ionization. Core ionization and subsequent Auger decays offers not only an efficient way of creating multiply charged molecular ions, but also a favourable way of keeping track of the ionization and subsequent relaxation

processes. Tri-atomic molecules viz. OCS and CS₂ were studied with this view. Subsequent to the ionization of the S(2*p*) shells in these molecules, the relaxation of the excited molecule occurs by Auger electron emission, resulting in the formation of mostly dicationic molecular ions with a wide gamut of electronic configurations. Doubly ionized molecular ion states resulting after ejection of high energy Auger electrons (i.e due to electronic decay from low binding energy orbitals) are stable in nature. On the other hand unstable states are only attained when low energy Auger electrons are emitted, and, as a consequence results in a stronger coupling of the excess energy to the nuclear degrees of freedom, leading to molecular bond rupture. A clear correspondence between the energy ordering of the levels participating in the electronic decay and the availability of energy for subsequent breaking of the molecular bonds is observed: two body break-up is dominant for ionization to dissociative states that are lower in binding energy, while three-body fragmentation increases as higher energy states are accessed. For all fragmentation channels, the mean kinetic energy released upon molecular break-up shows a gradual increase for dissociation following ionization to higher binding energy Auger states. This increase is much lesser than the estimated difference in energy acquired by the molecule upon various Auger decay. This implies that though the higher and more repulsive dissociative states become more populated as highly bound orbitals are ionized due to Auger decay, most of the parent molecular ion energy is partitioned as internal energy of the fragment ions than as their kinetic energy. Alternatively, the energy of the excited dication may also be expelled in the form of photons thus yielding lower KER upon dissociation. It is found that bent conformations of the triatomic molecular ions are accessed in course of the dissociation and the fragment kinetic energies are found to depend on the geometry of the transient molecular ion.

Our study reveals that molecular dissociation is highly dependent on the electronic decay mechanisms, to the extent that for the same ionizing perturbation the stability of the molecular ion is governed by which electronic decays follow the primary perturbation. The kinematics of the dissociation is also found to

be dependent on the electron loss processes. The dependence can be understood in terms of the energy sharing between the electrons and nuclei of the molecule. These observations will aid theoretical computations of the dissociative ionization processes in triatomic molecules, as the observations provide clues to the coupling between electronic and nuclear degrees of freedom in excited molecular ion states. They also provide clues as to which molecular ion conformations are relevant to dissociation.

5.2 Future Scope

The study presented here is limited to core ionization of single atom in a molecule, namely, the $2p$ orbital of sulphur in OCS and CS₂. The scope of the study can be easily extended for core ionization of all the atoms that make a molecule. The energetics involved in core ionization of different atoms and the resultant Auger decay in a molecule is different. Thus, the evolution of the molecular ion will be highly dependent on which atomic core is ionized and the Auger decay following such ionization. Selectively ionizing deep core orbitals of various atoms in a molecule, investigations can be made if the effect of such ionization remains localized or the perturbation is shared by all the atomic partners. Signatures of this can be sought in the resulting Auger decay by identifying the orbitals that take part in the decay mechanism. Simultaneously, tracking the molecular fragmentation pattern for core ionization of various atoms in a molecule will shed light on which bonds are broken upon the ionization and subsequent Auger decays. Thus, insights can be gained about the local and overall effects on the molecule due to different atomic core orbital ionization and various Auger decays.

Improving the energy resolution of the electron spectrometer will enable us to come closer to being able to select specific electronic states that are precursors of dissociation. This would be a step ahead of the current ability to merely select a band of states within a certain energy range. Such selectivity will bring us closer

to measuring the cross-section (for a particular fragmentation channel) differential in the internal energy of the transient molecular ion. In turn this will make it easier to compare experimental cross-sections with theoretical predictions as it will narrow down the number of excited states that are needed to be taken into account.

Another interesting direction to look in is to perform similar core ionization experiments with electron or ion impact. The ionization mechanism by electron or ion impact on molecules is quite different than ionization due to photoabsorption. The electronic decay mechanisms and the behaviour of the core ionized molecular ion may thus be different for the two cases. Just as core electron can be selectively ionized by photon of specific energy, for ion impact ionization of molecules, certain core shell can also be preferentially ionized. Matching the velocity of the projectile ion with the orbital velocity of the electron in the core shell enhances the probability of capture of the core electron by the ionic projectile creating a core hole. Thus, selective ionization of core electrons is plausible for ion impact experiments and the electronic decays and fragmentation mechanisms of molecules can be studied by a similar experiment and compared with the photoionization studies reported here. We have done some preliminary ion impact experiments at 15 MV Pelletron facility at IUAC, New Delhi. A complete set of experiments are planned to be carried out in near future.

Bibliography

- [1] J. Dalton, *A New System of Chemical Philosophy*, Vol. 1 (Rickerstaff, 1808).
- [2] J. J. Thomson, *Phil. Mag.* **44**, 293 (1897).
- [3] E. Rutherford, *Phil. Mag.* **21**, 669 (1911).
- [4] N. Bohr, *Phil. Mag.* **26**, 1 (1913).
- [5] W. Pauli, *Z.Physik A* **31**, 765 (1925).
- [6] E. Schrödinger, *Ann. Physik* **79**, 361 (1926).
- [7] E. Schrödinger, *Ann. Physik* **79**, 489 (1926).
- [8] E. Schrödinger, *Ann. Physik* **80**, 437 (1926).
- [9] E. Schrödinger, *Ann. Physik* **81**, 109 (1926).
- [10] P. Linstrom and W. Mallard, *NIST chemistry webbook* (National Institute of Standards and Technology Gaithersburg MD, 2001).
- [11] M. Born and R. Oppenheimer, *Ann. Physik* **84**, 457 (1927).
- [12] A. Szabo and N. S. Ostlund, *Modern Quantum Chemistry: Introduction to advanced electronic structure theory* (Dover Publications, 1989).
- [13] I. N. Levine, *Quantum Chemistry*, Vol. 5 (Prentice Hall, 2000).
- [14] P. W. Atkins and R. S. Friedman, *Molecular Quantum Mechanics*, Vol. 3 (Oxford University Press, 1997).

- [15] G. Herzberg, *Molecular spectra and molecular structure. I. Spectra of diatomic molecules*, Vol. 1 (D. Van Nostrand, 1950).
- [16] J. Xie and R. N. Zare, *J. Chem. Phys.* **93**, 3033 (1990).
- [17] P. Auger, *C. R. A. S.* **177**, 169 (1923).
- [18] J. Ullrich and V. Shevelko, *Many-particle quantum dynamics in atomic and molecular fragmentation* (Springer, 2003).
- [19] D. Mathur, *Phys. Rep.* **225**, 193 (1993).
- [20] H. Hertz, *Weid. Ann.* **31**, 983 (1887).
- [21] W. Hallwachs, *Weid. Ann.* **33**, 301 (1888).
- [22] P. Lenard, *Ann. Physik* **8**, 149 (1902).
- [23] A. Einstein, *Ann. Physik* **17**, 132 (1905).
- [24] K. Siegbahn, C. Nordling, A. Fahnnann, R. Nordberg, K. Hamrin, J. Hedmann, G. Johansson, T. Bergmark, S. Karlsson, I. Lindgren, and B. Lindberg, *ESCA-Atomic, Molecular and Solid State Structure Studied by Means of Electron Spectroscopy* (Almqvist and Wiksells, 1967).
- [25] K. Siegbahn, C. Nordling, G. Johansson, J. Hedmann, P. Heden, K. Hamrin, U. Gelius, T. Bergmark, L. Werme, R. Manne, and Y. Baer, *ESCA Applied to Free Molecule* (North Holland, 1969).
- [26] D. Matthews, *Methods of Experimental Physics: Atomic Physics, Accelerators*, edited by P. Richard, Vol. 17 (Academic Press, 1980) Chap. 9.
- [27] E. Granneman and M. van der Wiel, *Handbook on Synchrotron Radiation*, edited by E. Koch, Vol. 1a (North-Holland, 1983) Chap. 6.
- [28] V. Abrosimov, Y. Gordeev, M. Panov, and N. Fedorenko, *Sov. Phys. Tech. Phys.* **9**, 1248 (1965).
- [29] E. Everhart and Q. C. Kessel, *Phys. Rev. Lett.* **14**, 247 (1965).

- [30] Q. C. Kessel and E. Everhart, *Phys. Rev.* **146**, 16 (1966).
- [31] J. McConkey, A. Crowe, and M. Hender, *Phys. Rev. Lett.* **29**, 1 (1972).
- [32] R. Olson, J. Ullrich, and H. Schmidt-Böcking, *J. Phys. B* **20**, L809 (1987).
- [33] J. Levin, R. Short, H. Cederquist, S. Elston, J. Gibbons, I. Sellin, H. Schmidt-Böcking, *et al.*, *Phys. Rev. A* **36**, 1649 (1987).
- [34] G. Grandin, D. Hennecart, X. Husson, D. Lecler, I. Lesteven-Vaisse, and D. Lisfi, *Eur. Phys. Lett.* **6**, 683 (1988).
- [35] J. Ullrich and H. Schmidt-Böcking, *Phys. Lett. A* **125**, 193 (1987).
- [36] J. Ullrich, H. Schmidt-Böcking, and C. Kelbch, *Nucl. Instrum. Methods. A* **268**, 216 (1988).
- [37] R. Ali, V. Frohne, C. Cocke, M. Stockli, S. Cheng, and M. Raphaelian, *Phys. Rev. Lett.* **69**, 2491 (1992).
- [38] B. Siegmann, U. Werner, R. Mann, N. M. Kabachnik, and H. O. Lutz, *Phys. Rev. A* **62**, 022718 (2000).
- [39] B. Siegmann, U. Werner, Z. Kaliman, Z. Roller-Lutz, N. M. Kabachnik, and H. O. Lutz, *Phys. Rev. A* **66**, 052701 (2002).
- [40] T. Reddish, *Nature* **431**, 404 (2004).
- [41] T. Weber, A. O. Czasch, O. Jagutzki, A. Müller, V. Mergel, A. Kheifets, E. Rotenberg, G. Meigs, M. H. Prior, S. Daveau, *et al.*, *Nature* **431**, 437 (2004).
- [42] V. Sharma and B. Bapat, *Eur. Phys. J. D* **37**, 223 (2006).
- [43] J. Ullrich, R. Dörner, V. Mergel, O. Jagutzki, L. Spielberger, and H. Schmidt-Böcking, *Comments At. Mol. Phys.* **30**, 285 (1994).
- [44] V. Mergel, R. Dörner, J. Ullrich, O. Jagutzki, S. Lencinas, S. Nüttgens, L. Spielberger, M. Unverzagt, C. L. Cocke, R. E. Olson, M. Schulz, U. Buck,

- E. Zanger, W. Theisinger, M. Isser, S. Geis, and H. Schmidt-Böcking, *Phys. Rev. Lett.* **74**, 2200 (1995).
- [45] R. Dörner, V. Mergel, O. Jagutzki, L. Spielberger, J. Ullrich, R. Moshhammer, and H. Schmidt-Böcking, *Phys. Rep.* **330**, 95 (2000).
- [46] R. Moshhammer, J. Ullrich, M. Unverzagt, W. Schmidt, P. Jardin, R. E. Olson, R. Mann, R. Dörner, V. Mergel, U. Buck, and H. Schmidt-Böcking, *Phys. Rev. Lett.* **73**, 3371 (1994).
- [47] R. Moshhammer, M. Unverzagt, W. Schmitt, J. Ullrich, and H. Schmidt-Böcking, *Nucl. Instrum. Methods. B* **108**, 425 (1996).
- [48] R. Moshhammer, J. Ullrich, H. Kollmus, W. Schmitt, M. Unverzagt, O. Jagutzki, V. Mergel, H. Schmidt-Böcking, R. Mann, C. J. Woods, and R. E. Olson, *Phys. Rev. Lett.* **77**, 1242 (1996).
- [49] T. Jahnke, T. Weber, A. L. Landers, A. Knapp, S. Schössler, J. Nickles, S. Kammer, O. Jagutzki, L. Schmidt, A. Czasch, T. Osipov, E. Arenholz, A. T. Young, R. Díez Muiño, D. Rolles, F. J. García de Abajo, C. S. Fadley, M. A. Van Hove, S. K. Semenov, N. A. Cherepkov, J. Rösch, M. H. Prior, H. Schmidt-Böcking, C. L. Cocke, and R. Dörner, *Phys. Rev. Lett.* **88**, 073002 (2002).
- [50] A. T. Eppink and D. H. Parker, *Rev. Sci. Instrum.* **68**, 3477 (1997).
- [51] D. Parker and A. T. Eppink, *J. Chem. Phys.* **107**, 2357 (1997).
- [52] T. P. Rakitzis, P. C. Samartzis, and T. N. Kitsopoulos, *J. Chem. Phys.* **111**, 10415 (1999).
- [53] B. Bakker, D. Parker, and W. van der Zande, *Phys. Rev. Lett.* **86**, 3272 (2001).
- [54] C. Cocke and R. E. Olson, *Phys. Rep.* **205**, 153 (1991).
- [55] J. Ullrich, R. Moshhammer, R. Dörner, O. Jagutzki, V. Mergel, H. Schmidt-Böcking, and L. Spielberger, *J. Phys. B* **30**, 2917 (1997).

- [56] J. Ullrich, R. Moshhammer, A. Dorn, R. Dörner, L. Schmidt, and H. Schmidt-Böcking, *Rep. Prog. Phys.* **66**, 1463 (2003).
- [57] B. Whitaker, *Imaging in molecular dynamics: technology and applications* (Cambridge University Press, 2003).
- [58] W. Wiley and I. McLaren, *Rev. Sci. Instrum.* **26**, 1150 (1955).
- [59] D. R. Olander and V. Kruger, *J. App. Phys.* **41**, 2769 (1970).
- [60] D. Secombe, S. Collins, and T. Reddish, *Rev. Sci. Instrum.* **72**, 2550 (2001).
- [61] J. Risley, *Rev. Sci. Instrum.* **43**, 95 (1972).
- [62] D. Manura and D. Dahl, *SIMION 8.0*, Tech. Rep. (User Manual, Tech. rep., Scientific Instrument Services, Inc., NJ 08551, 2007).
- [63] O. Jagutzki, V. Mergel, K. Ullmann-Pfleger, L. Spielberger, U. Meyer, R. Dörner, and H. Schmidt-Boecking, in *SPIE's International Symposium on Optical Science, Engineering, and Instrumentation* (International Society for Optics and Photonics, 1998) pp. 322–333.
- [64] I. Ali, R. Dörner, O. Jagutzki, S. Nüttgens, V. Mergel, L. Spielberger, K. Khayyat, T. Vogt, H. Bräuning, K. Ullmann, R. Moshhammer, J. Ullrich, S. Hagmann, K.-O. Groeneveld, C. Cocke, and H. Schmidt-Böcking, *Nucl. Instrum. Methods B* **149**, 490 (1999).
- [65] A. Savitzky and M. Golay, *Analytical Chemistry* **36**, 1627 (1964).
- [66] A. Kikas, S. Osborne, A. Ausmees, S. Svensson, O.-P. Sairanen, and S. Aksela, *J. Electron Spect. Relat. Phenom.* **77**, 241 (1996).
- [67] L. Frasiniski, M. Stankiewicz, P. Hatherly, and K. Codling, *Meas. Sci. Tech.* **3**, 1188 (1992).
- [68] A. E. Slattery, T. A. Field, M. Ahmad, R. I. Hall, P. Lablanquie, and F. Penent, *Meas. Sci. Tech.* **13**, 2007 (2002).

- [69] G. Prümper and K. Ueda, Nucl. Instrum. Methods A **574**, 350 (2007).
- [70] J. Eland, Laser. Chem. **11**, 259 (1991).
- [71] B. Bapat and V. Sharma, J. Phys. B **40**, 13 (2007).
- [72] N. Neumann, D. Hant, L. Schmidt, J. Titze, T. Jahnke, A. Czasch, M. Schöffler, K. Kreidi, O. Jagutzki, H. Schmidt-Böcking, and R. Dörner, Phys. Rev. Lett. **104**, 103201 (2010).
- [73] R. Dalitz, Phil.Mag. **44**, 1068 (1953).
- [74] A. Bettini, *Introduction to Elementary Particle Physics* (Cambridge University Press, 2008).
- [75] L. Lammich, Doctoral Dissertation, University of Heidelberg (2004).
- [76] M. Hochlaf, R. Hall, F. Penent, H. Kjeldsen, P. Lablanquie, M. Lavollée, and J. Eland, Chem. Phys. **207**, 159 (1996).
- [77] J. Eland and E. Duerr, Chem. Phys. **229**, 13 (1998).
- [78] W. H. Press, B. P. Flannery, S. A. Teukolsky, and W. T. Vetterling, *Numerical Recipes* (Cambridge Univ Press, 1990).
- [79] W. Eberhardt, T. Sham, R. Carr, S. Krummacher, M. Strongin, S. Weng, and D. Wesner, PRL **50**, 1038 (1983).
- [80] W. Eberhardt, J. Stöhr, J. Feldhaus, E. Plummer, and F. Sette, PRL **51**, 2370 (1983).
- [81] J. Murakami, M. Nelson, S. Anderson, and D. Hanson, J. Chem. Phys. **85**, 5755 (1986).
- [82] C. Miron, M. Simon, N. Leclercq, D. Hansen, and P. Morin, PRL **81**, 4104 (1998).
- [83] X. J. Liu, G. Prümper, E. Kukk, R. Sankari, M. Hoshino, C. Makochekanwa, M. Kitajima, H. Tanaka, H. Yoshida, Y. Tamenori, and K. Ueda, Phys. Rev. A **72**, 042704 (2005).

- [84] W. Eberhardt, E. Plummer, I.-W. Lyo, R. Carr, and W. Ford, *PRL* **58**, 207 (1987).
- [85] R. Murphy and W. Eberhardt, *J. Chem. Phys.* **89**, 4054 (1988).
- [86] U. Alkemper, R. Hörnig, and F. von Busch, *J. Phys. B* **29**, 35 (1996).
- [87] D. Céolin, O. Travnikova, Z. Bao, M. Piancastelli, T. Tanaka, M. Hoshino, H. Kato, H. Tanaka, J. Harries, Y. Tamenori, C. Prümper, T. Lischke, X. J. Liu, and K. Ueda, *J. Chem. Phys.* **128**, 024306 (2008).
- [88] J. A. Bearden, *Rev. Mod. Phys.* **39**, 78 (1967).
- [89] T. Carroll, D. Ji, and T. Thomas, *Journal of Electron Spectroscopy and Related Phenomena* **51**, 471 (1990).
- [90] D. Minelli, F. Tarantelli, A. Sgamellotti, and L. Cederbaum, *J. Chem. Phys.* **107**, 6070 (1997).
- [91] J. Ridard, B. Levy, and P. Millié, *Chem. Phys.* **122**, 403 (1988).
- [92] T. Kaneyasu, M. Ito, Y. Hikosaka, and E. Shigemasa, *Journal of Korean Physical Society* **54**, 371 (2009).
- [93] T. Masuoka and H. Doi, *Phys. Rev. A* **47**, 278 (1993).
- [94] V. Brites, J. Eland, and M. Hochlaf, *Chem. Phys.* **346**, 23 (2008).
- [95] U. Ankerhold, B. Esser, and F. von Busch, *Chem. Phys.* **220**, 393 (1997).
- [96] P. Erman, A. Karawajczyk, E. Rachlew, M. Stankiewicz, and K. Y. Franzén, *Phys. Rev. A* **56**, 2705 (1997).
- [97] T. Masuoka, I. Koyano, and N. Saito, *J. Chem. Phys.* **97**, 2392 (1992).
- [98] M. Jana, B. Ray, P. Ghosh, and C. Safvan, *J. Phys. B: At. Mol. Opt. Phys.* **43**, 215207 (2010).
- [99] M. Hamdan, D. Almeida, and A. Brenton, *J. Phys. B: At. Mol. Opt. Phys.* **22**, 1817 (1989).

- [100] J. Eland, M. Hochlaf, P. Linusson, E. Andersson, L. Hedin, and R. Feifel, *J. Chem. Phys.* **132**, 014311 (2010).
- [101] A. Krasnoperova, E. Gluskin, and L. Mazalov, *Journal of Structural Chemistry* **18**, 206 (1977).
- [102] R. G. Hayes and W. Eberhardt, *J. Chem. Phys.* **94**, 6398 (1991).
- [103] P. Lablanquie, I. Nenner, P. Millie, P. Morin, J. Eland, M. Hubin-Franskin, and J. Delwiche, *J. Chem. Phys.* **82**, 2951 (1985).
- [104] P. Milli e, I. Nenner, P. Archirel, P. Lablanquie, P. Fournier, and J. Eland, *J. Chem. Phys.* **84**, 1259 (1986).
- [105] M. Hochlaf, R. Hall, F. Penent, J. Eland, and P. Lablanquie, *Chem. Phys.* **234**, 249 (1998).
- [106] U. Alkemper and F. Von Busch, *J. Electron Spect. Relat. Phenom.* **93**, 115 (1998).
- [107] M. Lavoll e, *Rev. Sci. Instrum.* **70**, 2968 (1999).
- [108] M. Hochlaf, G. Chambaud, and P. Rosmus, *J. Chem. Phys.* **108**, 4047 (1998).
- [109] J. Eland, C. Rigby, E. Andersson, J. Palaudoux, L. Andric, F. Penent, P. Linusson, L. Hedin, L. Karlsson, J.-E. Rubensson, Y. Hikosaka, K. Ito, P. Lablanquie, and R. Fiefel, *J. Chem. Phys.* **132**, 104311 (2010).
- [110] K. Yoshiki Franz en, P. Erman, P. Hatherly, A. Karawajczyk, E. Rachlew, and M. Stankiewicz, *Chem. Phys. Lett.* **285**, 71 (1998).
- [111] J. Eland, *Mol. Phys.* **61**, 725 (1987).
- [112] F. von Busch, *J. Phys. B* **34**, 431 (2001).
- [113] V. Sharma and B. Bapat, *Phys. Rev. A* **75**, 040503 (2007).

Publications attached with the thesis

1. **A combined electron-ion spectrometer for studying complete kinematics of molecular dissociation upon shell selective ionization**, K. Saha, S. B. Banerjee, and B. Bapat, Rev. Sci. Instrum., **84**, 073101 (2013).
2. **Three body dissociation of CS_2^{2+} subsequent to various S(2*p*) Auger transitions**, K. Saha, S. B. Banerjee, and B. Bapat, J. Chem. Phys., **139**, 164309 (2013).

A combined electron-ion spectrometer for studying complete kinematics of molecular dissociation upon shell selective ionization

K. Saha,^{a)} S. B. Banerjee, and B. Bapat

Physical Research Laboratory, Navrangpura, Ahmedabad 380009, India

(Received 23 January 2013; accepted 10 June 2013; published online 1 July 2013)

A combined electron-ion spectrometer has been built to study dissociation kinematics of molecular ions upon various electronic decay processes ensuing from ionization of neutral molecules. The apparatus can be used with various ionization agents. Ion time-of-flight (ToF) spectra arising from various electronic decay processes are acquired by triggering the ToF measurement in coincidence with energy analyzed electrons. The design and the performance of the spectrometer in a photoionization experiment is presented in detail. Electron spectra and ion time of flight spectra resulting from valence and $2p_{1/2}$ ionization of Argon and those from valence ionization of CO are presented to demonstrate the capability of the instrument. The fragment ion spectra show remarkable differences (both kinematic and cross sectional) dependent on the energy of the ejected electron, corresponding to various electron loss and decay mechanisms in dissociative photoionization of molecules.

© 2013 AIP Publishing LLC. [<http://dx.doi.org/10.1063/1.4811796>]

I. INTRODUCTION

The formation and dissociation of molecular ions under the impact of various projectiles has been an active area of research for several decades, and detailed kinematics have become available from experiments in the last decade.¹ Such studies have usually been performed using time-of-flight (ToF) mass spectrometers with multiparticle coincidence technique, revealing dissociation patterns.²⁻⁴ One approach towards obtaining greater details of the electronic processes accompanying dissociative ionization involves combination of ToF mass spectrometer with electron energy analyzer.⁵⁻⁸ For the ions alone, with the advent of Recoil Ion Momentum Spectroscopy (RIMS),⁹ extremely detailed kinematics of the ions formed in atomic collisions became accessible, and this technique was later extended to the study of dissociative ionization of molecules. The latter development enables probing into the transient precursor molecular ion and reveal properties such as its geometry, molecular state, and kinetic energy distribution of the fragments that are formed due to dissociation.¹⁰⁻¹³

In this paper, we report the design and performance of a spectrometer capable of studying the kinematics of molecular dissociation upon various electronic decay processes due to valence or core ionization of the molecule. The instrument is a combination of an electrostatic electron energy analyzer to identify an electron loss process (we use the term “electron loss process” to cover electron ejection due to photoionization and subsequent decays leading to different (ground/excited) final states of the target) in a molecule and the corresponding dissociation kinematics is revealed by an ion momentum spectrometer. Though, spectrometers, such as “reaction microscopes,”¹⁴ are capable of revealing electron and ion kinematics simultaneously,^{15,16} a pulsed excitation source is essential for their operation. The spectrometer described here

is free from this restriction. It is based on analyzing the energy of the electrons ejected in any projectile–target collision (under single collision conditions) by an electrostatic cylindrical mirror analyzer (CMA) and using the energy-analyzed electron signal as the trigger for the time-of-flight measurement of the ion ejected in the same event. The ion detector is a position sensitive, multi-hit capable detector, permitting the recovery of complete ion kinematics.

II. DESCRIPTION OF SET-UP

A. Target and excitation source

A primary requirement for this kind of experiments, is a collision zone that is well localized in space, and target atoms or molecules that have a narrow spread of kinetic energies. This is by-and-large achieved by a crossed projectile beam and target beam geometry. Large spatial extent of the target source leads to poorer resolution of fragment ion momentum as well as electron spectrum. In our set-up, a fine capillary of internal diameter of 0.15 mm is used to obtain an effusive beam of the target gas. The target density of 10^{12} cm⁻³ is obtained with this arrangement. Additionally, the same gas can be admitted into the vacuum chamber through a 6 mm aperture which is kept away from the ionization region, while maintaining the flow rate. This aperture and the effusive capillary has the same gas input line with the provision of controlling both of them by separate valves. This bypass gas inlet line is used to purge the gas line and can also be useful for recording spectra with the gas flooding the vacuum chamber.

In this work, photons from the Indus-1 Synchrotron source at RRCAT, Indore are used as the projectile. The Indus-1 synchrotron is a 450 MeV electron storage ring with peak current of 100 mA. Beam lifetime of Indus-1 is about 4 h. Radiation in the VUV range is produced at a bending magnet with a critical wavelength of 61 Å. A toroidal grating monochromator was used to select the photon wavelength.

^{a)}Electronic mail: koushik@prl.res.in

The photon beam cross section was $1 \times 3 \text{ mm}^2$ having a photon flux of 10^{10} s^{-1} with energy resolution of $E/\Delta E = 300$. A polyamide filter was used between the experimental station and the monochromator to avoid contamination of the beam line by the target gas as well as to cut off higher order wavelength from the toroidal grating, although the higher order wavelength contamination from the grating at the wavelengths used is negligible.

The apparatus can be used not only with photon beams, but also with electron or ion beams, with the simple addition of a Faraday cup at the beam exit.

B. The spectrometer

In order to perform kinematically complete analysis of molecular fragmentation, detection and identification of all the ionic fragments along with the electrons emitted in the process is important. The ionic fragments must be analyzed for their charge state, mass, as well as momentum and detected in a time ordered sequence. The electrons, on the other hand, must be energy analyzed to pinpoint the ionization and subsequent relaxation process within the molecule. Hence, a combination of both, ion momentum spectrometer and an electron spectrometer, working simultaneously, is required to realize this.

1. Ion momentum spectrometer

The ion momentum spectrometer consists of a double field Wiley–McLaren¹⁷ type ToF spectrometer with a position sensitive ion detector. The spectrometer is second order space focusing ToF spectrometer, i.e, it compensates for the effect of spatial spread of the ions on their flight times to second order in the initial spread. Three rings (marked r_1 , r_2 , r_3 , see Fig. 1) with the provision to hold fine meshes are used to generate the extraction field for the ions formed due to ionization. These rings have a outer diameter of 100 mm and an inner (open) diameter of 42 mm. All rings are fitted with fine mesh to generate uniform electric field. The extraction gap (s) is 6 mm and the acceleration gap (a) too is 6 mm. The gas-jet is placed midway between r_1 and r_2 . After the ring stack is a drift tube of length 162 mm and inner diameter of 42 mm. The drift tube is terminated with a ring and mesh assembly (marked r_4 , see Fig. 1). Beyond the drift tube is a microchannel plate of active area of 40 mm diameter with a delay line anode for position resolved detection of the ions (Roentdek GmbH). By applying suitable potentials to the extraction rings, a continuous electric field of 166 V/cm is generated in the extraction region, while an electric field 1000 V/cm is created in the acceleration region. The drift region is kept field free by shorting the drift tube and the rings r_3 , r_4 . The detector is biased at -2300 V for detection of ions.

Ions produced due to projectile impact on the target atoms/molecules are first extracted from the interaction region and then accelerated by a second electric field before entering the field free drift tube. Ion time of flight is recorded by an electron–ion coincidence (described later), and is the key for identification of the ionic species on the basis of the

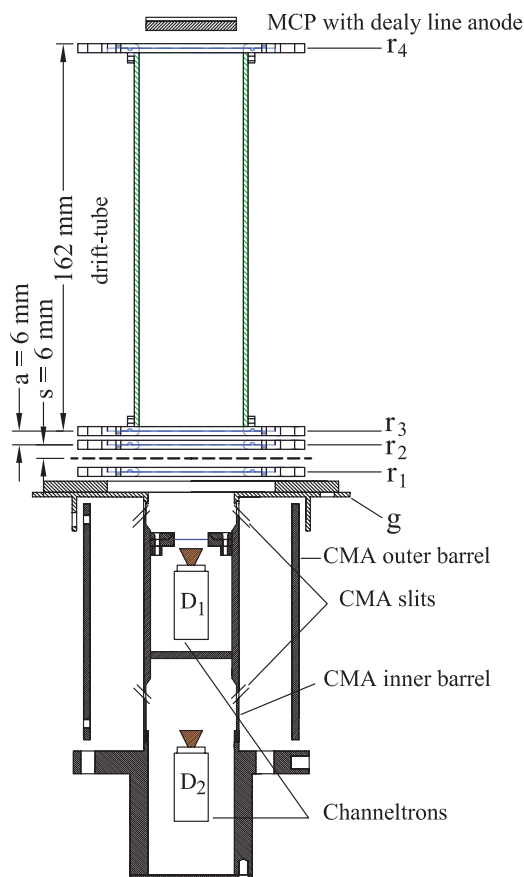


FIG. 1. The combined electron ion spectrometer. The horizontal thick dashed line denotes the projectile beam molecular beam plane. The slits of the CMA are shown exaggerated for clarity. The figure is approximately to scale.

mass-to-charge ratio. Additionally, the ion momentum component along the direction of the applied extraction field (p_z) can be derived from the time of flight information. The ion hit position on the other hand reveals the components of the momentum of the ion along the transverse direction with respect to the applied field (p_x , p_y). Thus, complete kinematics of molecular dissociation event can be studied using this method. A detailed description of this method can be found in Refs. 10 and 18.

Particle trajectory simulation for this spectrometer was carried out using SIMION 8.0.¹⁹ Assuming a point source for ion creation and applying the extraction fields as mentioned earlier, it was observed that singly charged ionic fragments having kinetic energy up to 7 eV can be detected without any loss irrespective of their direction of emission. For doubly and triply charged ionic fragments, the kinetic energies for which there is complete detection are 14 eV and 21 eV, respectively. This is true for any ionic species as the divergence of the ions in the extraction field is roughly proportional to the ratio of the square root of kinetic energy gained by the ion to its charge. The simulated trajectories for a few ionic species are shown in Fig. 2.

2. Electron spectrometer

Energy analysis of the electrons emitted due to ionization of the target gas is done by a Cylindrical Mirror

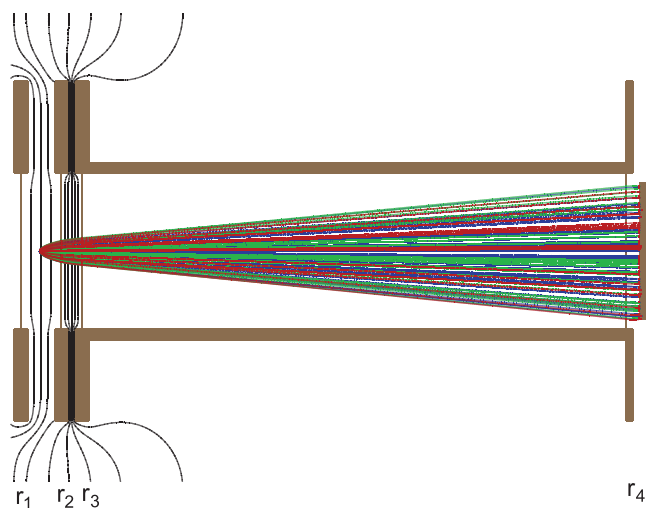


FIG. 2. Simulated trajectories of C^+ , N^+ , and O^+ ions with 7 eV initial kinetic energy. Black contours are the equipotential lines.

Analyzer (CMA). This analyzer is mounted co-axially opposite to the ToF spectrometer. Since a low event rate is mandatory for electron-ion coincidence measurements, it is vital that the genuine electrons from the reaction volume are efficiently detected and analyzed by the electron analyzer. A single pass CMA²⁰ has a high luminosity, while offering reasonable energy resolution, and was therefore chosen as the analyzer. In the standard CMA configuration, there is no electric field in the reaction zone. For our purpose, however, this requirement cannot be met as the reaction zone has to be immersed in an electric field for extracting the ions. The CMA was designed with this constraint. The length of the CMA is 106 mm with slit to slit distance (L) of 79.8 mm. The slit width (w) is 3 mm. The outer diameter of the inner barrel and the inner diameter of the outer barrel of CMA are 42 mm and 89 mm, respectively. A grounded disc (g, see Fig. 1) with an aperture of 40 mm at its center is placed in front of the CMA. This disc creates a retarding field that compensates for the increase in energy of the electrons due to field in the extraction gap. Thus, the electrons enter the CMA with almost the same energy with which it was ejected from the atom/molecule albeit with a spread in energies owing to varying angles of ejection. This energy compensation is beneficial due to the fact that the resolution of the CMA decreases with increase in energy. So, for the same initial energy electron, energy enhanced electrons (due to the extraction field) without any energy compensation will be detected with a lower resolution than the electrons which undergo retardation due to the grounded disc. In the standard configuration, the included angle of the cone of trajectories entering the CMA is $42^\circ \pm 2^\circ$. In the present configuration, the trajectories of electrons are altered by the extraction field. This results in transport of electrons ejected at angles greater than the standard angle to the CMA for energy analysis.

Simulations of the electron spectrometer were done using SIMION. Trajectories of electrons of different energy were studied. As expected, simulations show that due to the electric field applied for ion extraction, the correct angle of ejection

for any electron to enter the analyzer depends on the energy with which it is ejected. The extraction field (in the interaction zone) and the subsequent retarding field before the entrance into the CMA radial field distorts the envelope of trajectories entering the CMA, resulting in a larger portion of the Newton sphere being projected onto the CMA slits, increasing the luminosity of the analyzer in comparison with the standard configuration without an extraction field. For isotropically emitted 70 eV electrons, the acceptance with a field of 166 V/cm is 1.3 times the acceptance without field. The gain is 1.16 for 140 eV electrons. Simulations show that the optimum distance between the source of electrons from entrance slit plane of the CMA assembly is 15 mm. The effusive target jet is therefore set at that distance. The appropriate voltages to be applied to the outer barrel of the CMA for electrons with various energies were calculated. The CMA voltage was found to vary linearly with the energy of the electrons maintaining constant scale factor of 1.6. The angular acceptance ($\Delta\alpha$) of the slit was found to span $\pm 2^\circ$ around the ideal ejection angle for all electron energies. Simulated electron trajectories, assuming a point source for electron emission, are shown in Fig. 3.

Electrons entering the CMA are energy analyzed by the electrostatic field that is generated by applying a negative potential to the outer cylinder and keeping the inner cylinder at ground potential. Due to this field electrons of a particular energy are focussed onto to the exit slit for detection. Varying the potential of the outer cylinder such that it scans the range in which the energies of the emitted electrons lie, generates the electron spectrum. Two channeltrons (Sjuts Optotechnik) of active diameter of 10 mm are used as detectors in this CMA assembly. One is placed inside the inner barrel of the CMA for detecting energy un-analyzed electrons (D_1), whereas the other is placed at the end of the CMA assembly to detect energy analyzed electrons (D_2). A positive bias of 1800 V is applied to both the channeltrons for electron

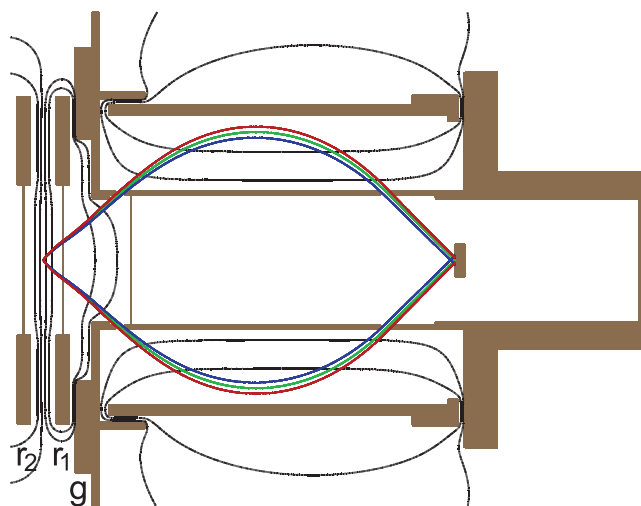


FIG. 3. Simulated trajectory of electrons with 70 eV energy. Middle one (green) is the trajectory for electrons with ideal angle of ejection. Outer (red) and inner (blue) trajectories are for electrons with ejection angle varying by $+2^\circ$ and -2° respectively from the ideal ejection angle. Black contours are the equipotential lines.

detection. The usefulness of the first detector will be discussed later.

C. Spectrometer housing and vacuum specifications

The spectrometer assembly is housed in stainless steel vacuum chamber with all metal joints. The chamber has a diameter of 160 mm and length of 725 mm with four orthogonal CF63 ports in one plane for the crossed target and projectile beams. The spectrometer is mounted with its axis along the axis of the chamber, so that the projectile beam, gas jet, and the spectrometer axis are mutually perpendicular. There are auxiliary ports for pumping, electrical connections, and vacuum gauges. The chamber is pumped by a 520 l/s turbomolecular pump backed by a dry scroll pump. The chamber pressure after bake out is 2×10^{-8} mbar, which rises to 5.0×10^{-7} mbar when gas is introduced at 5.0 mbar stagnation pressure behind the effusive capillary. An ionization gauge is used to monitor the chamber pressure while stagnation pressure is monitored by a Pirani gauge. Vaporized liquid samples can also be used as target for which the gas line is kept warm to avoid any condensation of the sample in the gas line.

D. Data acquisition

The experiment was conducted under single collision condition. Simultaneous detection of all the ionic species in coincidence with the electrons ejected in the process were done on an event by event basis. The electron detection signal from the channeltrons are first amplified by a preamp (ORTEC VT 120) and then fed to a Constant Fraction Discriminator (Philips Scientific, Model 715) to reduce spurious counts. The discriminated output from any one of the channeltrons can act as the START for the ion ToF clock. The STOP signal is derived from the ion detection pulse output of the MCP. For each ion STOP, four signals are generated by the delay line, which are processed to obtain the position of the ion hit.^{21,22} All signals from an ion hit (MCP collector and four delay lines) are amplified and discriminated in a ATR 19 unit (Roentdek GmbH). After discrimination, all ion time signals are digitized by a time to digital convertor (TDC), also from Roentdek GmbH). The digitized output is read on an event by event basis and stored as a list-mode file in a computer hard disk. The TDC has a time resolution of 500 ps. The position resolution depends on the ability to separate the delay line signals in time and the effective position resolution of the detector is found to be 0.85 mm. For each event trigger, the TDC remains active for 32 μ s during which up to four fragment ions can be recorded. The event rate for electron-ion coincidence from the first channeltron (D_1) is typically 300–3000 Hz and that with the second channeltron (D_2) is 30–150 Hz. The event rate depends on the photon flux at a particular wavelength and the target gas density and additionally, for the second channeltron (D_2), the CMA pass voltage. As is evident, the event rate for the energy discriminated electrons is low hence the first channeltron (D_1) becomes extremely useful for calibration and optimization of the ToF spectrometer.

III. PERFORMANCE OF THE SPECTROMETER

A. Calibration

1. Electron spectrometer

Calibration of the electron spectrometer was done using photoelectrons from ionization of Helium. Photons of various energies were used to generate photoelectrons having different energies. Helium was chosen as target gas for calibration, because it is a two electron system with a relatively simple electron spectrum. Each spectrum was background subtracted and the peak fitted with Gaussian function. The peak or the centroid value of the Gaussian is due to single ionization of the $1s$ orbital of Helium which has a binding energy of 24.59 eV.²³ The simulated and the experimental energy calibration of the CMA voltage against the pass energy are in close agreement, and the linearity of the pass energy with the voltage applied to the CMA has a R^2 value of 0.99.

Estimates of the energy resolution, ΔE , of the CMA are based on purely geometrical considerations, from simulations and from actual observation. The value of ΔE based on CMA geometry is calculated using Eq. (26) of Granneman and van der Wiel,²⁴ retaining terms up to the second order:

$$\frac{\Delta E}{E} = C_w \left(\frac{w}{L} \right) + C_\alpha (\Delta\alpha)^2. \quad (1)$$

Here, w , L , and $\Delta\alpha$ are geometrical parameters of the CMA whose values are mentioned earlier. The C_w and C_α coefficients have values 2.28 and 35.3 respectively in our case. For $E = 140$ eV, ΔE is calculated to be 18.1 eV. The value of ΔE from simulations, taking into account the transverse spatial spread of the photon beam, the divergence of the effusive beam (about 2.4 mm at the photon beam molecular beam overlap) and the voltages applied to the spectrometer, is about 40 eV at $E = 140$ eV. The experimentally determined value of ΔE at $E = 140$ eV is 24 eV. The reason for the disagreement in simulated and experimental ΔE values is discussed later.

Figure 4 shows the electron spectrum of Argon at photon energy 155 eV. This photon energy is well below the $2p$ threshold of Argon hence the electron spectrum generated is only due to the valence shell electrons. The raw spectrum is background subtracted and then smoothed using the Savitzky–Golay method.²⁵ The $3p$ and $3s$ lines are identified according to the NIST database²³ and two bands corresponding to few satellite lines are identified following Kikas *et al.*²⁶

2. Ion spectrometer

Mass calibration of the ToF spectrometer was done using photoionization of Argon at 210 eV (non resonant with Argon shell energies) with the START signal taken from channeltron D_1 . The ToF spectrum when triggered by an energy analyzed electron has fewer false coincidences due to the rejection of stray electrons. The ToF spectrum (at 155 eV photon energy), triggered by an energy analyzed electron (i.e, by CMA detector D_2), corresponding to the $3p$ peak of the electron spectrum is shown in Fig. 5. Argon was chosen as it is an easily available atomic gas which yields multiply charged ionic species upon ionization. Molecular gases are not suitable as they

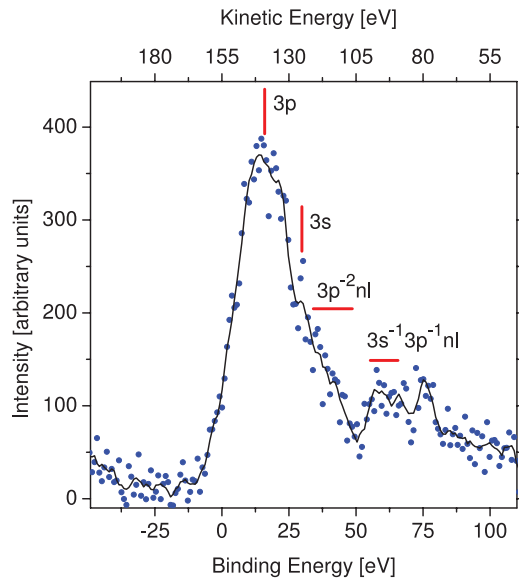


FIG. 4. Electron spectrum of Argon at 155 eV photon energy. The dots are the experimental data. The black line is generated by Savitzky-Golay smoothing. The $3p$ and $3s$ binding energy values are taken from the NIST database,²³ while positions of the satellite lines are taken from Kikas *et al.*²⁶

produce fragments with large kinetic energy, and few multiply charge parent molecular ions. The FWHM of the Ar^+ peak was found to be 16 ns while the mean ToF is 3607 ns, which gives a ToF resolution $t/\Delta t = 226$ corresponding to a mass resolution $m/\Delta m = 113$.

The ToF resolution also limits the resolution of the component of the ion momentum along the direction of the electric field. The resolution of the z component of momentum (Δp_z) is given by

$$\Delta p_z = q E_{ext} \Delta t,$$

where q is charge and E_{ext} is the electric field applied in the extraction region. For Ar^+ , $\Delta p_z = 21.6$ a. u.

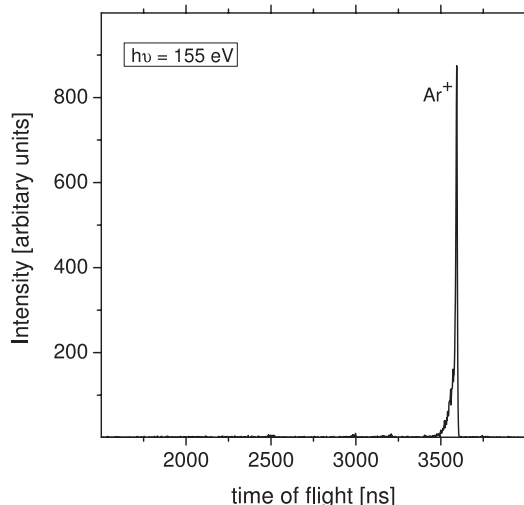


FIG. 5. Time of flight spectrum of Argon corresponding to ionization of $3p$ shell by 155 eV photons.

The resolution of the transverse component of ion momentum is limited by the position resolution of the delay line detector

$$\Delta p_{x,y} = m \Delta x, y / t.$$

For Ar^+ , this value is 8 a. u.

3. Discussion

To understand the reason for the discrepancies in estimated and actual values of the energy resolution of the CMA, and also the asymmetry in the peak shapes of the TOF spectrum, we carried out further simulation of the particle trajectories, in which the collision zone was moved slightly about the geometric mid-plane of the extraction gap. An approximate profile of the molecular beam was also generated based on Olander's work.²⁷ These simulations in conjunction with the actual spectra show that the overlap between the photon beam and the molecular beam is not optimal. The central axis of the neutral beam (where the number density is highest) does not intersect the photon beam at the mid-point of the transverse spatial extent of the photon beam. The mid-point of the photon beam spot is approximately 1 mm off the mid-plane, toward the ToF spectrometer and does not lie in the virtual zero potential plane as it ideally should, when the extraction voltages are symmetric (but opposite in sign). However, the distribution of the density of ions formed in the intersection zone is dominated by the distribution of molecules in the effusive beam, not the spatial profile of the photon beam. The photon beam profile is essentially flat across a 3 mm extent along the spectrometer axis. The ion source extent is thus sharply curtailed on the CMA side, resulting in a tail on the lower ToF side of the ToF peak and a sharp truncation on the higher ToF side.

Similar considerations apply to the photoelectron spectrum. Due to the asymmetry of the ion source w.r.t. the zero potential plane in the extraction field, there is a smaller flux of electrons born closer to the CMA, and in general, there will be few electrons contributing to the lower binding energy side of any given peak. However, the effect is not obvious in the electron spectrum, owing, primarily to the poor resolution. The actual CMA resolution is better than the simulated value primarily due to the asymmetric overlap of the effusive beam with the photon beam; the effective extent of the ionization region is about half of the spread of the effusive beam.

B. Shell selective ionization of Ar

Ionization of Argon at the $2p_{1/2}$ threshold is carried out by setting the photon energy to 250.6 eV. Since the outermost shell of Argon is $3p$, ionization of the $2p_{1/2}$ shell results in copious LVV Auger electron emission, and the electron spectrum at this photon energy is significantly different from the previous case, as seen in Fig. 6.

Some of the LMM Auger lines are identified following Werme *et al.*²⁸ The Auger lines are not well resolved owing to the limitation of the CMA resolution.

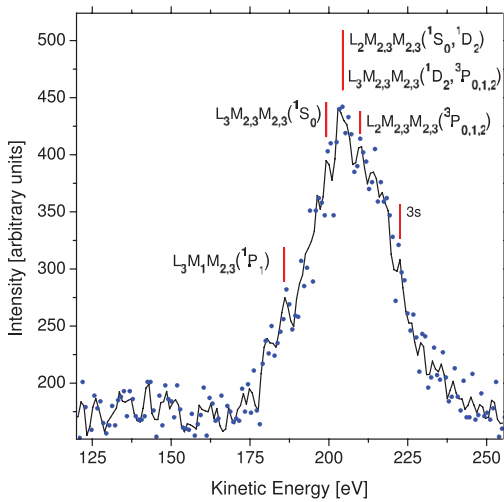


FIG. 6. Auger electron spectrum of Argon at 250.6 eV photon energy. The dots are the experimental data. The black line is generated by 5-point Savitzky–Golay smoothing. Line identification is done following Werme.²⁸

Figure 7 shows the ToF spectrum for the peak corresponding to $L_2M_{2,3}M_{2,3}(^1S_0, ^1D_2)$ and $L_3M_{2,3}M_{2,3}(^1D_2, ^3P_{0,1,2})$ Auger lines in the electron spectrum. It is evident that in this case, the formation of doubly ionized species is more likely than singly ionized species. This is due to the fact that Auger emission inherently is a double ionization process.

Although the dominant ion peak in the ToF spectrum with Auger electron–ion coincidence is Ar^{2+} , a small Ar^+ peak also appears. The ratio of $\text{Ar}^{2+}/\text{Ar}^+$ with Auger coincidence in the present work is 26, which is significantly higher than the reported value (6) of the same ratio for the same photon energy, but without the selection of the ejected electron.²⁹ This implies that although we are mostly recording Ar^{2+} , consistent with the Auger process, there is a small Ar^+ signal which may be associated with the electron continuum under the Auger peak.

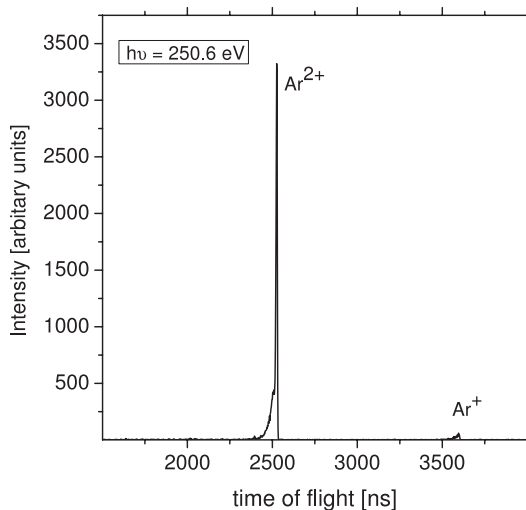


FIG. 7. Time of flight spectrum of Argon corresponding to $L_2M_{2,3}M_{2,3}(^1S_0, ^1D_2)$, $L_3M_{2,3}M_{2,3}(^1D_2, ^3P_{0,1,2})$ Auger transitions. The small Ar^+ signal is due to the electron continuum which lies under the Auger peak.

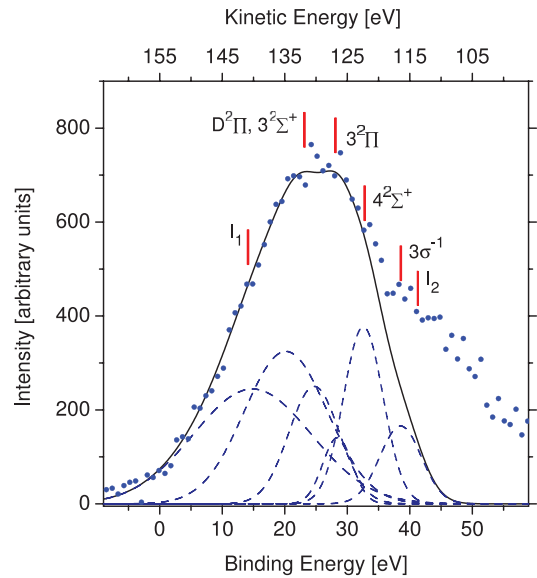


FIG. 8. Electron spectrum of CO at 155 eV photon energy. Dots are experimental data. The black curve is the sum of multiple Gaussian fits, the latter shown by dashed curves. The fit extends only up to the double ionization threshold, as beyond this energy the two ejected electrons share the energy continuously, leading to a continuum distribution. I_1 and I_2 indicate the single and double ionization potentials, taken from the NIST database²³ and Hochlaf *et al.*,³⁰ respectively. Line identification in the range 22 eV – 40 eV follows Eland *et al.*³¹

C. Molecular fragmentation and correlated kinematics

We have carried out dissociative ionization of CO at 155 eV photon energy. This photon energy is non-resonant with the energy levels of CO, but is sufficiently higher than the double ionization threshold of CO, so at this energy some deep-lying electronic levels can be excited to ionization. The K shell of neither O nor C can be ionized with the shortest photon wavelength available at this beamline.

The electron spectrum of CO upon excitation by photon beam of energy 155 eV is shown in Fig. 8. The raw spectrum was background subtracted following a quadratic fit to the background, and a multiple Gaussian fit was made to the subtracted spectrum by employing the Levenberg–Marquardt method. The first and second ionization potentials I_1 and I_2 were taken from the NIST database²³ and Hochlaf *et al.*,³⁰ respectively. The initial values of the centroids and the number of Gaussians for the fitting procedure were set by a correspondence with the major features reported by Eland *et al.*³¹ The centroids were not frozen to the initial values in the fitting procedure. In the final fit, the centroids were found to deviate from the values in the literature by approximately 1 eV. The fit extends only up to the double ionization threshold, as beyond this energy the two ejected electrons share the energy continuously, leading to a continuum distribution.

We consider three cases of ionization–excitation of CO, by selecting the pass energy of the ejected electrons, and recording the ion spectrum in each case. The ToF spectra are shown in Fig. 9. The energy of the electrons correspond to

- (a) excitation just above the single ionization threshold of CO;

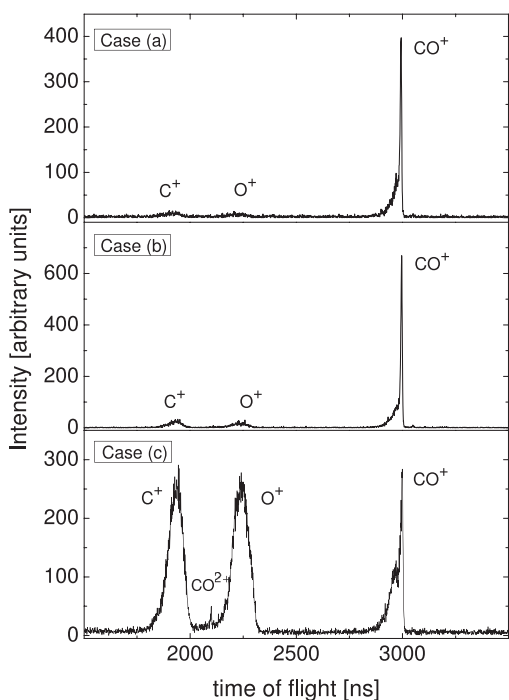


FIG. 9. Time of flight spectrum of CO corresponding to different excitation energies as described in the text.

- (b) excitation well above single ionization, but below double ionization, mostly leading to $D^2\Pi$, $3^2\Sigma^+$ states of CO^+ ; and
- (c) excitation just above the double ionization threshold of CO.

The ToF spectra in the three cases are vastly different, indicating that propensity to a particular dissociation channel is a function of the electron loss mechanism. The dissociation channels $\text{CO}^+ \rightarrow \text{O}^+ + \text{C}$ and $\text{CO}^+ \rightarrow \text{C}^+ + \text{O}$ are open in each case. In cases (a) and (b), where most of the photon energy is carried away by the ejected electron, the dominant channel is non-dissociative single ionization. As compared to case (a) there is a slight enhancement of the dissociative channels in case (b), as some of the absorbed energy is coupled to the internal degrees of freedom of the molecular ion. Case (c) is the onset of double ionization accompanied by transitions to high-lying dissociative states of CO^+ . In this case, the cross section for dissociative single ionization channels far exceeds that for non-dissociative channels.

For every detected ion, the complete momentum vector is determined in the experiment. When a break-up results into only ions, the complete correlated momentum map can be determined from the measured momenta of the multiple ions formed in the break-up. In the case of a diatomic molecule, the momentum of the neutral fragment, if there is one, is simply equal and opposite to the momentum of the charged fragment, so the correlated momentum, and hence the kinetic energy of the neutral fragment may also be derived. Thus, the sum of the fragment kinetic energies, or the kinetic energy release (KER) in the dissociation, can be determined for all dissociation channels of a diatomic molecule.

The kinetic energy release distributions (KERD) for the channel $\text{CO}^+ \rightarrow \text{O}^+ + \text{C}$ in the three cases are shown in

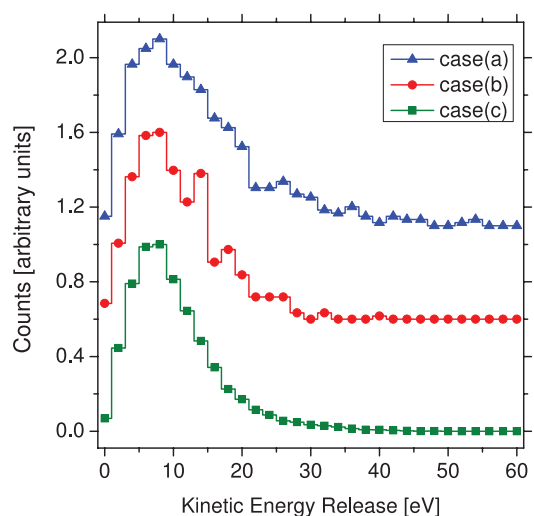


FIG. 10. Kinetic Energy Release distribution for the channel $\text{CO}^+ \rightarrow \text{O}^+ + \text{C}$ corresponding to different excitation energies as described in the text. Curves are offset for clarity.

Fig. 10. The variation in the KER of the fragments as a function of the energy of the electron ejected in the ionization is clearly seen from these graphs. Differences in the KERD suggest that different electron loss processes trigger different dissociation pathways, even though the same set of fragments are formed in the end. Dissociation pathways corresponding to different photoelectron energies can be attributed to the variety of excited states accessed by the precursor molecular ion. The excited state attained by the molecular ion due to particular electron loss mechanism governs the kinematics of the dissociation process while the population of the excited state is related to the cross section of the dissociation channel.

In case (c), an additional channel opens up: that of charge symmetric dissociation of the dication, viz., $\text{CO}^{2+} \rightarrow \text{C}^+ + \text{O}^+$. This channel is revealed in the (t_1, t_2) correlation map (Fig. 11). The KERD for this channel is also shown in the same figure. Detailed investigation of the kinematics of this

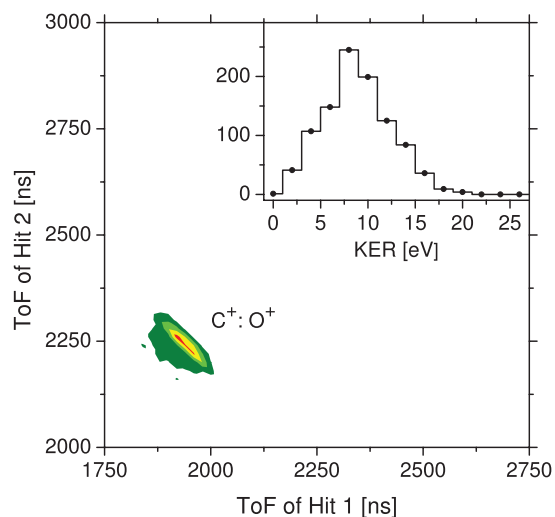


FIG. 11. Ion-ion correlation map for the channel $\text{CO} \rightarrow \text{C}^+ + \text{O}^+$, which opens when the excitation energy is just above the double ionization threshold (case (c) described in the text). The inset shows the kinetic energy release distribution for this channel.

dissociation channel has been reported by Tarisien *et al.*³² The charge asymmetric dissociation channels of CO_2^{2+} , leading to $\text{C}^{2+}:\text{O}$ and $\text{O}^{2+}:\text{C}$ are still closed. We conclude that the threshold for charge symmetric dissociation of CO^{2+} is lower than that for charge asymmetric dissociation.

IV. SUMMARY

We have designed and tested a combined electron and ion spectrometer in which a cylindrical mirror analyzer is used to analyze the energy of the electrons and the corresponding ion is mass and momentum analyzed using an ion momentum spectrometer in coincidence with this electron. The basic performance of the spectrometer is demonstrated in the case of photoionization of Argon. The electron spectrum as well as the ToF spectrum are presented, both for valence shell ionization as well as $2p_{1/2}$ inner shell ionization of Argon. It is demonstrated that valence shell excitations produce singly ionized ionic species while inner shell excitations yield doubly ionized ionic species due to Auger type electronic decay.

Further, kinematics of dissociation of CO molecule upon various valence shell ionization processes were studied. It is in the case of molecular fragmentation that the instrument's capability truly stands out. In spite of moderate energy resolution of the CMA owing to a source width and fairly strong extraction field, broad features in the electron spectrum of CO are discernible. Molecular dissociation mechanisms were studied for selected electron loss processes. Excitation to high lying dissociative states of the singly ionized molecule and the onset of double ionization could be separated by selecting the energy of the ejected electron. Greater selectivity of the dissociation pathways is possible with improved CMA resolution. The resolving power of the CMA may be improved by reducing the source extent (apart of course, from reducing the slit size, with a consequent loss of luminosity).

Kinetic energy and kinetic energy release distributions of the fragments have been analyzed for ionization of various electronic states. The distributions reflect the nature of the excited state potential energy surface of the molecular ion. Effectively, the selection of ejected electron energy and recording of ion kinematics subject to this selection by our instrument gives us control over which excited electronic state we investigate the dynamics of.

ACKNOWLEDGMENTS

The authors would like to express their gratitude to G. S. Lodha, M. H. Modi, R. K. Gupta, and Amol Singh for the support provided at the Indus-1 synchrotron facility, RRCAT, Indore. They also thank their colleagues K. P. Subramanian, Amrendra Pandey, Prashant Kumar, and C. P. Safvan for useful discussions, suggestions, and help in running the experiment. The assistance provided by the staff of the PRL

and SAC workshops in the fabrication of the instrument is also gratefully acknowledged. The authors would also like to thank the anonymous referee for constructive criticisms and suggestions.

- ¹J. Ullrich and V. Shevelko, *Many-Particle Quantum Dynamics in Atomic and Molecular Fragmentation* (Springer, 2003).
- ²P. Lablanquie, J. Delwiche, M. Hubin-Franskin, I. Nenner, P. Morin, K. Ito, J. Eland, J. Robbe, G. Gandara, J. Fournier *et al.*, *Phys. Rev. A* **40**, 5673 (1989).
- ³I. Ben-Itzhak, K. Carnes, S. Ginther, D. Johnson, P. Norris, and O. Weaver, *Phys. Rev. A* **47**, 3748 (1993).
- ⁴T. Field and J. Eland, *Chem. Phys. Lett.* **211**, 436 (1993).
- ⁵R. Murphy and W. Eberhardt, *J. Chem. Phys.* **89**, 4054 (1988).
- ⁶T. Kerkau, B. Krässig, O. Schwarzkopf, H. Kossmann, B. Kämmerling, and V. Schmidt, *Nucl. Instrum. Methods Phys. Res. A* **479**, 555 (2002).
- ⁷G. Alberti, E. Fainelli, F. Maracci, M. Mastropietro, R. Platania, and L. Avaldi, *Rev. Sci. Instrum.* **76**, 073101 (2005).
- ⁸D. Céolin, O. Travnikova, Z. Bao, M. Piancastelli, T. Tanaka, M. Hoshino, H. Kato, H. Tanaka, J. Harries, Y. Tamenori *et al.*, *J. Chem. Phys.* **128**, 024306 (2008).
- ⁹J. Ullrich, R. Moshhammer, R. Dörner, O. Jagutzki, V. Mergel, H. Schmidt-Böcking, and L. Spielberger, *J. Phys. B* **30**, 2917 (1997).
- ¹⁰K. Ueda and J. Eland, *J. Phys. B* **38**, S839 (2005).
- ¹¹S. Legendre, E. Giglio, M. Tarisien, A. Cassimi, B. Gervais, and L. Adoui, *J. Phys. B* **38**, L233 (2005).
- ¹²B. Bapat and V. Sharma, *J. Phys. B* **40**, 13 (2007).
- ¹³N. Neumann, D. Hant, L. Schmidt, J. Titze, T. Jahnke, A. Czasch, M. Schöffler, K. Kreidi, O. Jagutzki, H. Schmidt-Böcking *et al.*, *Phys. Rev. Lett.* **104**, 103201 (2010).
- ¹⁴J. Ullrich, R. Moshhammer, A. Dorn, R. Dörner, L. Schmidt, and H. Schmidt-Böcking, *Rep. Prog. Phys.* **66**, 1463 (2003).
- ¹⁵R. Moshhammer, M. Unverzagt, W. Schmitt, J. Ullrich, and H. Schmidt-Böcking, *Nucl. Instrum. Methods Phys. Res. B* **108**, 425 (1996).
- ¹⁶R. Doerner, H. Bräuning, J. Feagin, V. Mergel, O. Jagutzki, L. Spielberger, T. Vogt, H. Khemliche, M. Prior, J. Ullrich *et al.*, *Phys. Rev. A* **57**, 1074 (1998).
- ¹⁷W. Wiley and I. McLaren, *Rev. Sci. Instrum.* **26**, 1150 (1955).
- ¹⁸B. Whitaker, *Imaging in Molecular Dynamics: Technology and Applications* (Cambridge University Press, 2003).
- ¹⁹D. Manura and D. Dahl, Technical Report: User Manual (Scientific Instrument Services, Inc., New Jersey, 2007).
- ²⁰J. Risley, *Rev. Sci. Instrum.* **43**, 95 (1972).
- ²¹O. Jagutzki, V. Mergel, K. Ullmann-Pfleger, L. Spielberger, U. Meyer, R. Dörner, and H. Schmidt-Boecking, in *SPIE's International Symposium on Optical Science, Engineering, and Instrumentation* (International Society for Optics and Photonics, 1998), pp. 322–333.
- ²²I. Ali, R. Dörner, O. Jagutzki, S. Nüttgens, V. Mergel, L. Spielberger, K. Khayyat, T. Vogt, H. Bräuning, K. Ullmann *et al.*, *Nucl. Instrum. Methods Phys. Res. B* **149**, 490 (1999).
- ²³P. Linstrom and W. Mallard, *NIST Chemistry WebBook* (National Institute of Standards and Technology, Gaithersburg, MD, 2001).
- ²⁴E. Granneman and M. van der Wiel, *Handbook on Synchrotron Radiation*, edited by E. Koch (North-Holland, 1983), Vol. 1a, Chap. 6.
- ²⁵A. Savitzky and M. Golay, *Anal. Chem.* **36**, 1627 (1964).
- ²⁶A. Kikas, S. Osborne, A. Ausmees, S. Svensson, O.-P. Sairanen, and S. Aksela, *J. Electron Spectrosc. Relat. Phenom.* **77**, 241 (1996).
- ²⁷D. R. Olander and V. Kruger, *J. Appl. Phys.* **41**, 2769 (1970).
- ²⁸L. Werme, T. Bergmark, and K. Siegbahn, *Phys. Scr.* **8**, 149 (1973).
- ²⁹U. Ankerhold, B. Esser, and F. von Busch, *Chem. Phys.* **220**, 393 (1997).
- ³⁰M. Hochlaf, R. Hall, F. Penet, H. Kjeldsen, P. Lablanquie, M. Lavollée, and J. Eland, *Chem. Phys.* **207**, 159 (1996).
- ³¹J. Eland and E. Duerr, *Chem. Phys.* **229**, 13 (1998).
- ³²M. Tarisien, L. Adoui, F. Frémont, D. Lelièvre, L. Guillaume, J. Chesnel, H. Zhang, A. Dubois, D. Mathur, S. Kumar *et al.*, *J. Phys. B* **33**, L11 (2000).

Three body dissociation of CS_2^{2+} subsequent to various S(2p) Auger transitions

K. Saha,^{a)} S. B. Banerjee, and B. Bapat

Physical Research Laboratory, Navrangpura, Ahmedabad 380009, India

(Received 21 August 2013; accepted 8 October 2013; published online 25 October 2013)

Fragmentation kinematics of CS_2 following various S(2p) Auger transitions is studied. Employing a combination of electron energy analysis and recoil ion momentum spectroscopy, changes in the dissociation channel yields, as well as the differences in the kinematical parameters for various bands of Auger hole states are presented. The fragmentation mechanism for dissociative channels leading to complete atomization of CS_2^{2+} molecular ion is studied in detail. We find that CS_2^{2+} does not retain linear geometry and is bent before undergoing concerted break-up. It is also observed that different geometric configurations of the CS_2^{2+} precursor result in different kinetic energy release values.

© 2013 AIP Publishing LLC. [<http://dx.doi.org/10.1063/1.4826468>]

I. INTRODUCTION

Dissociation of molecules due to core ionization has been a subject of great interest during the last few decades. Apart from identification of ionic fragment upon core ionization,¹⁻⁵ the attempt has been on establishing the fragmentation pathways of the core ionized molecule.⁶⁻⁹ Core ionization of molecules often leads to Auger decay. This results in filling up of the core vacancy producing two valence shell holes with the emission of Auger electrons in the process. Auger electrons are produced with a specific kinetic energy characteristic of the binding energy of the valence orbitals that take part in the decay process. Thus, the kinetic energy of the Auger electrons carries the information about the final electronic configuration of the molecular ion. It is the dynamics of this doubly valence ionized molecular ion states that govern the fragmentation pathways and hence the ionic fragments produced upon core ionization. The first step towards understanding the dynamics of molecular dissociation is to have information about complete kinematics of the process. In this paper, we present the fragmentation kinematics of CS_2 following various S(2p) Auger transitions. The changes in the kinematics and cross-section of various dissociation channels is studied for different Auger transitions leading to the formation of different CS_2^{2+} molecular ion states. The fragmentation mechanisms for complete atomization of the molecule are also studied in detail.

II. EXPERIMENT

The experiments were performed at a bending magnet beam line at INDUS-1, a 450 MeV synchrotron facility at RRCAT, Indore. The beam line is equipped with a toroidal grating monochromator. Photons of mean energy of 171 eV at an energy resolution of $E/\Delta E = 300$ were used for this experiment. The critical wavelength of the synchrotron source is 61 Å (about 203 eV) and the photon flux beyond 270 eV at

our beamline was found to negligible, in part due to the ageing of the gratings. Thus, when the grating is set for 171 eV, second order contamination will be minor. The photon beam had a cross section of $1 \times 3 \text{ mm}^2$ with a flux of 10^{10} s^{-1} . The photon beam was in a cross beam geometry with the effusive target gas jet which was admitted in the experimental chamber through a fine capillary. The CS_2 sample used for the experiment was 99.5% pure. CS_2 is a volatile liquid at room temperature (boiling point 46 °C). The sample as well as the entire gas line was kept warm throughout the experiment to prevent condensation in the gas line. The capillary was placed in the middle of two spectrometers, a Cylindrical Mirror Analyzer (CMA)¹⁰ for electron energy analysis and a Recoil Ion Momentum Spectrometer (RIMS) for fragment ion detection, set axially opposite to each other. The capillary remained immersed in the continuous ion extraction field, but was kept in the virtual ground plane between the positively and negatively biased extraction plates. Details of the spectrometer and the experimental procedure followed are reported elsewhere.¹¹

Electrons ejected from the target CS_2 molecules were energy analyzed by the CMA upon applying a varying voltage to its outer cylinder while the inner cylinder was held at ground potential. Electrons with different energies are admitted in the CMA depending on the voltage in its outer cylinder and is detected by a channeltron, thus generating the electron spectrum. A high resolution electron spectrum is not achievable in our set-up due to the finite width of the ionization region and the effect of the continuous ion extraction field on the ejected electrons. The overall resolution of the CMA taking into account these factors is about 17%. Once the electron spectrum was generated, the CMA was set to appropriate voltage so as to admit electrons of specific kinetic energies which correspond to a certain electronic decay process.

The resultant ionic fragments were detected in coincidence with the energy analyzed electrons by RIMS set-up. We used a double field Wiley-McLaren type time of flight (ToF) spectrometer¹² with a positive sensitive micro channel

^{a)}Electronic mail: koushik@prl.res.in

plate (MCP) placed at its end for detection of ions. Fragment ions produced due to photo-ionization of the molecule were first extracted and then accelerated by continuous electric fields of 166 V/cm and 1000 V/cm, respectively. The ions then fly through a field free drift tube and get detected by the MCP kept at the end of the drift tube. The ToF of each ion was recorded taking START from the electron detection pulse while ion detection marked the STOP. Positions of the ion hit were also recorded along with the ToF information; this was used to obtain the momentum of the ion. The correlated ToF and position information of up to four fragment ions from an ionization event can be recorded in coincidence with the energy analyzed electron and stored in a list mode file. This makes our spectrometer suitable for studying the complete kinematics of fragmentation of small molecules.

Experiments were performed under single collision condition. The count rate in the experiment varies with the storage ring electron current. Typically, the ion count rate varied between 200 and 1000 Hz and that of the Auger electron was between 50 and 250 Hz while the electron-ion coincidence event rate varied over 30–150 Hz. The data acquisition time for each Auger energy was typically about 4 h. Although the coincidence event rate was kept low, the unequal count rates of electrons and ions led to false coincidence counts. About 10% of the total electron-ion-ion triple coincidence counts was estimated to be due to false coincidences in our experiment. Analysis was done after subtracting the contribution due to false coincidences. Another source of error in the analysis may arise due to the dead time of the MCP and the associated electronics. Ions with same mass to charge ratio will not get registered as two particles if they arrive within the dead time. The dead time of our ion detection system is about 20 ns. This amounts to a loss of only 0.7% in the simultaneous detection of two S^+ ions, assuming an isotropic distribution of the fragments. Hence, the detector dead time issue does not pose a serious source of error in our analysis.

III. RESULTS AND DISCUSSION

A. Electron spectrum

CS_2 is a linear molecule belonging to the $D_{\infty h}$ point group. The ground state valence electronic configuration can be written as $(5\sigma_g)^2(4\sigma_u)^2(6\sigma_g)^2(5\sigma_u)^2(2\pi_u)^4(2\pi_g)^4$ which arises due to bonding between carbon $2s2p$ and sulphur $3s3p$ orbitals. Ionization of the sulphur $2p$ orbital of CS_2 produces a core hole in the molecule. This triggers various $S(2p)$ Auger decays, and emission of Auger electrons leads to double electron removal from the valence shell of the molecule. Each Auger decay mechanism yields Auger electrons with specific kinetic energy and unique valence electronic configuration of the doubly ionized molecule. The $S(2p)$ Auger electron spectrum of CS_2 upon ionization by 171 eV ($S2p_{1/2}$ ionization threshold¹³ of CS_2) photon beam is shown in Fig. 1. At this photon energy both the $S(2p)$ orbitals may be ionized, thus the spectrum will have contribution from both $S2p_{1/2}$ and $S2p_{3/2}$ Auger decay. The photon energy is shared between the emitted electrons and the molecular ion. Using photons of energy equivalent to the $S2p_{1/2}$ ionization threshold ensures that

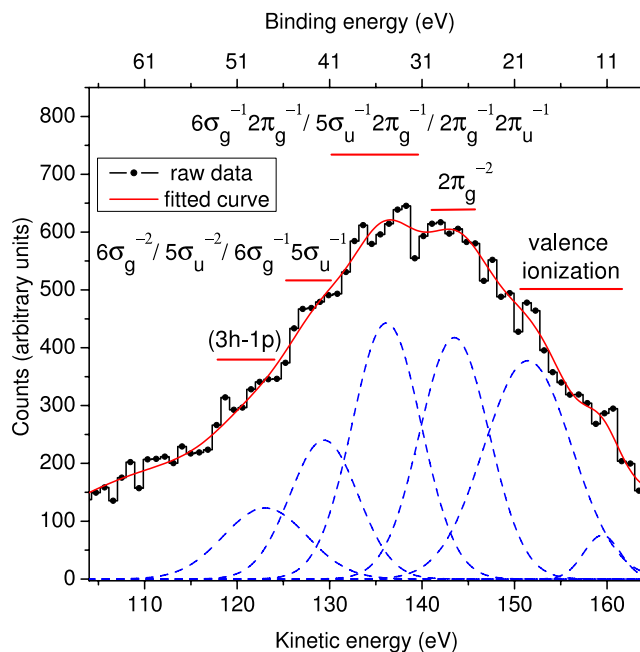


FIG. 1. Broad features of the $S(2p)$ Auger electron spectrum of CS_2 . Features for both $S2p_{1/2}$ and $S2p_{3/2}$ Auger decay are contained in this spectrum. The histogram is raw data; the continuous curve is the fitted sum of multiple Gaussian functions, which are shown individually by broken curves and correspond to the distribution of electrons from various Auger states. The broad features are identified following Hayes *et al.*¹⁴ and the dication states are determined following Lablanquie *et al.*¹⁵ and Millie *et al.*¹⁶ The binding energy scale at the top is obtained by subtracting the Auger kinetic energy from $S2p_{1/2}$ threshold. Groups of close-lying doubly ionized states resulting from Auger decay are indicated by horizontal lines.

the photo electron emitted will have negligible kinetic energy, thus, by measuring the Auger electron kinetic energy we can have a rough estimate of the energy gained by the molecular dication. On the other hand, post collisional interactions may introduce energy shift in the electron spectrum, but the resolution of the CMA is not sufficient enough to account for this. The raw spectrum is background subtracted and Gaussians are fitted with a correspondence with the features in the spectrum. Though the resolution of the spectrum is moderate, the broad features are identifiable by comparison with higher resolution $S(2p)$ Auger spectra from the literature.¹⁴

The binding energy of the state in question is obtained by subtracting the Auger kinetic energy from $S2p_{1/2}$ threshold. States other than $(3h - 1p)$ are determined by a binding energy correspondence with the dominant dication states.^{15,16} Features having mean binding energy less than the threshold energy for double ionization (around 27 eV¹⁷) are marked as valence ionization since Auger transitions will always lead to double ionization. The $(3h - 1p)$ states correspond to Auger transitions that produce 3 hole 1 particle type of electronic configuration, which results when 3 vacancies are created in the molecular orbitals and 1 electron is excited to one of the virtual orbitals instead of being ejected. It has been shown that $(3h - 1p)$ states are dominant at higher binding energies.¹⁶ A similar dominance of $(3h - 1p)$ states has been reported for $S(2p)$ Auger decay of OCS .¹⁸

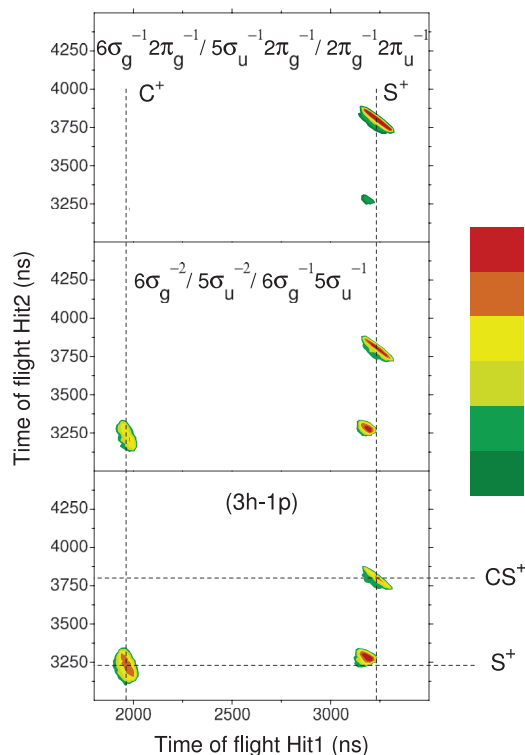


FIG. 2. Ion-ion coincidence map of CS_2 corresponding to different final Auger states. Color bar indicates intensity. There is no intensity normalization across panels.

B. Fragmentation channels

Of the four groups of dication states identified from the electron spectrum, the $2\pi_g^{-2}$ group of states is stable.¹⁵ The stability implies a large CS_2^{2+} signal in the ToF spectrum but no fragment ions, when triggered by electrons from this band of energies. On the other hand, ion spectra triggered by electrons from the bands $(6\sigma_g^{-2}, 5\sigma_u^{-2}, 6\sigma_g^{-1}5\sigma_u^{-1})$ and $(3h-1p)$ would lead to a weak CS_2^{2+} signal in the ToF spectrum, and various ions due to the fragmentation of CS_2^{2+} . This has been observed earlier in some studies.^{14,19} In our ToF spectrum, however, we observe weak signals of fragment ions for ionization to the $2\pi_g^{-2}$ state, which is attributable to contamination from higher binding energy states, owing to the moderate resolution of the electron energy analyzer.

The fragmentation channels arising from unstable molecular ions can be visualized in the ion-ion coincidence map, where the ToF of the ionic fragments are plotted against each other. Each island in the coincidence map denotes a particular fragmentation channel. Fig. 2 shows the ion-ion coincidence map between ToF of first fragment and second one, corresponding to various Auger states. The intense $\text{S}^+:\text{CS}^+$ coincidence island for $(6\sigma_g^{-1}2\pi_g^{-1}, 5\sigma_u^{-1}2\pi_g^{-1}, 2\pi_g^{-1}2\pi_u^{-1})$ states suggests that for ionization to low binding energy states, only single bond breaks occur, leading to two body fragmentation of CS_2^{2+} . In fact the cross-section for $\text{S}^+:\text{CS}^+$ dissociation channel is maximum for ionization to these binding energy states. The cross-section for two body break-up decreases as fragmentation occurs from higher binding energy

states as can be seen in Fig. 2. Presence of another two body dissociation channel, namely $\text{C}^+:\text{S}_2^+$, has been reported by Lavollée;²⁰ we do not observe this channel in our experiment. The appearance energy threshold of the three body break-up channel $\text{C}:\text{S}^+:\text{S}^+$ is 37 eV.²¹ We see a faint signature of this channel ($\text{S}^+:\text{S}^+$ island) for ionization to $(6\sigma_g^{-1}2\pi_g^{-1}, 5\sigma_u^{-1}2\pi_g^{-1}, 2\pi_g^{-1}2\pi_u^{-1})$ states. The other three body fragmentation channel of CS_2^{2+} , $\text{C}^+:\text{S}^+:\text{S}$, has an appearance energy of 41 eV.²¹ This channel begins to appear ($\text{C}^+:\text{S}^+$ island) for ionization to $(6\sigma_g^{-2}, 5\sigma_u^{-2}, 6\sigma_g^{-1}5\sigma_u^{-1})$ states. The cross-section for both the channels leading to complete atomization increases for dissociation from $(3h-1p)$ states. As it is evident, complete atomization of the molecule becomes dominant for ionization of higher binding energy orbitals. This is a direct consequence of the fact that more internal energy is required to break both the C–S bonds as compared to a single bond rupture. Adequate energy is only available to the molecular ions which are formed upon ionization to higher binding energy states. Hence, we see a gradual decrease in cross-section of two body break-up and an increase in cross-section of three body break-up channels as we go from lower to higher binding energy states. Complete atomization can occur by either simultaneous or sequential breaking of the two bonds while the precursor molecular ion may have different geometries. Several variations of these possibilities have been considered in the literature for many triatomics.^{22–25} We focus on the complete atomization channels of CS_2^{2+} with a view to understand the kinematical changes occurring in the molecular ion during dissociation from different bands of Auger states. We base our analysis on the observed kinetic energy release and momentum distributions of the fragments.

It is worth mentioning here that though Auger decay primarily leads to double ionization, triple ionization of CS_2 is also possible at this photon energy via double Auger decay as discussed by Eland *et al.*²⁶ Ankerhold *et al.*²⁷ report a branching ratio for CS_2^{3+} to be about 10% of the total ion yield for ionization by 174 eV photons. Lavollée²⁰ also observed triple ionization of CS_2 for ionization around S(2p) threshold. But these studies were conducted without any energy selection of emitted electron. The appearance energy of stable CS_2^{3+} is 53 eV²⁶ while that of the dissociative states will be even higher in energy. Since, the binding energy range of the states for which this study is conducted is below the appearance energy threshold of CS_2^{3+} , tricationic states will not be ideally accessed in our case. In fact, we do not see trication dissociation channel for any of the states except $(3h-1p)$. A faint $\text{C}^+:\text{S}^+:\text{S}^+$ channel is observed in triple ion coincidence map (not shown here) for ionization to $(3h-1p)$ states. Due to its moderate energy resolution, low kinetic energy electrons corresponding to ionization to trication states may get admitted into the CMA when it is tuned to collect Auger electrons for ionization to $(3h-1p)$ dication states. The contribution of this channel in the $\text{C}^+:\text{S}^+$ island due to fragmentation of CS_2^{2+} is subtracted during analysis. Another possible source of contamination of the $\text{C}^+:\text{S}^+:\text{S}$ channel is from tricationic dissociation via $\text{C}^+:\text{S}_2^{2+}$ channel. These two channels cannot be distinguished from one another, but as we do not observe

$C^+:S_2^+$ channel in the coincidence map, we assume $C^+:S_2^{2+}$ channel is also absent in our experiment. In general, the cross-section for triple ionization at this photon energy is small and as reported by Lavollée²⁰ the contamination of dicationic dissociation channel is not severe.

C. Kinetic energy release

An important parameter in the kinematics of a dissociation pathway is the kinetic energy release (KER). Since several pathways may be active, there will be a kinetic energy release distribution (KERD), which is measured in the experiment. Studies employing various methods to obtain the kinetic energy from ToF spectra of the fragment ions arising from dissociation of CS_2^{2+} formed due to $S(2p)$ Auger decay have been done earlier. Hayes and Eberhardt¹⁴ fitted the ion-ion coincidence spectra with various Gaussian kinetic energy release distributions and predicted the center kinetic energy for different dissociation channels. For example, for $S^+:CS^+$ channel the major distribution is reported to be centered at 4.1 eV. Alkemper and von Busch¹⁹ reported a maximum KER for this channel as 4.5 eV by extracting the kinetic energy information from fragment ion ToF peak widths. In yet another study, von Busch²⁸ derived the mean kinetic energy of ion fragments from the variance of their coincidence ToF peak and for $S^+:CS^+$ channel the mean KER is observed to be a little higher than the previous two reports. By contrast to these works, in our experiment the complete information of all the momenta components enable us to directly measure the KER for various channels. Employing a similar technique Lavollée reported a peak KER value for $S^+:CS^+$ channel as 4.5 eV.²⁰ Due to the electron energy discrimination, we can provide KER information for various Auger state bands. For $S^+:CS^+$ channel the mean KER values corresponding to dissociation from $(6\sigma_g^{-1}2\pi_g^{-1}, 5\sigma_u^{-1}2\pi_g^{-1}, 2\pi_g^{-1}2\pi_u^{-1})$, $(6\sigma_g^{-2}, 5\sigma_u^{-2}, 6\sigma_g^{-1}5\sigma_u^{-1})$, and $(3h-1p)$ Auger states are 5 eV, 5.8 eV, and 6.4 eV, respectively. These values are closer to the report by von Busch²⁸ and also shows the increasing trend in mean kinetic energy as Auger electron kinetic energy de-

TABLE I. KER values (in eV) for different dissociation channels of CS_2^{2+} . KER values from previous studies by (a) Hayes and Eberhardt,¹⁴ (b) Alkemper and von Busch,¹⁹ (c) von Busch,²⁸ and (d) Lavollée²⁰ are presented. All the studies, other than case (c), have no electron energy selection. For case (c), mean KER is derived by summing the mean kinetic energies of fragments, and the range within which the KER value varies for different Auger electron energy is given. Mean KER values from our study for (i) $6\sigma_g^{-1}2\pi_g^{-1}, 5\sigma_u^{-1}2\pi_g^{-1}, 2\pi_g^{-1}2\pi_u^{-1}$, (ii) $6\sigma_g^{-2}, 5\sigma_u^{-2}, 6\sigma_g^{-1}5\sigma_u^{-1}$, and (iii) $(3h-1p)$ Auger states are also presented.

Channel	Previous studies	This work			
		(i)	(ii)	(iii)	
$S^+:CS^+$	(a)	4.1 (mean)	5 ± 0.46	5.8 ± 0.46	6.4 ± 0.46
	(b)	4.5 (max)			
	(c)	3.4–7.3(mean)			
	(d)	4.5 (peak)			
$C^+:S^+:S$	12 ± 0.65	12.74 ± 0.65	
$S^+:S^+:C$	9.6 ± 0.65	11.2 ± 0.65	

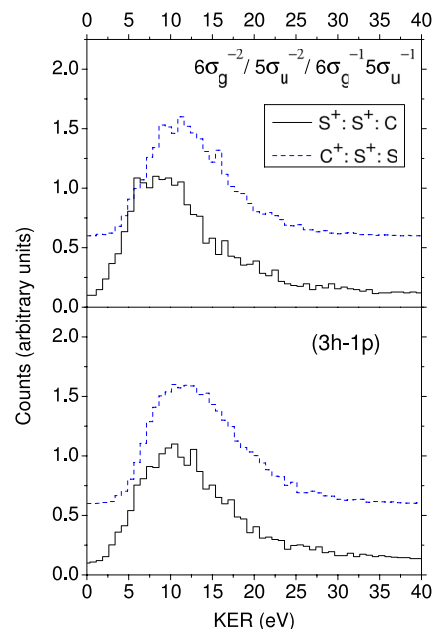


FIG. 3. Kinetic Energy Release (KER) distribution of various three body fragmentation channels of CS_2^{2+} corresponding to different final Auger states. Continuous curve: $S^+:S^+:C$ channel, broken curve: $C^+:S^+:S$ channel. Curves are offset for clarity.

creases as observed by von Busch. The KER value obtained in our experiment along with the value reported in some previous studies is summarized in Table I. The KERD for three-body fragmentation triggered by different Auger transitions is shown in Fig. 3. The maximum KER for each fragmentation channel remains same irrespective of the trigger Auger state, but an increase in mean KER value is observed for dissociations from lower and higher binding energy states. The mean KER value for $S^+:S^+:C$ channel is 9.6 eV and 11.2 eV, and for $C^+:S^+:S$ channel is 12 eV and 12.74 eV upon dissociation from $(6\sigma_g^{-2}, 5\sigma_u^{-2}, 6\sigma_g^{-1}5\sigma_u^{-1})$ and $(3h-1p)$ Auger states, respectively.

The increase in mean KER value with increasing binding energy of the triggering Auger state may be attributed to the increase in probability of the molecule being excited to higher energy more repulsive molecular ion states upon ionization from highly bound electronic states, thus yielding higher KER upon dissociation. But, the mean kinetic energy of the fragments does not increase significantly with the increase in the internal energy gained by the CS_2^{2+} due to ionization of higher binding energy orbitals. This, as pointed out in the earlier works,^{14,19} indicates the possibility that most of the precursor ion energy goes into the internal energy of the fragments rather being converted into their kinetic energy. Another possible scenario may be radiative decay of the excited dication state into lower dissociative states hence yielding lower KER in the process.

D. Correlated momenta

One of the ways to unravel the fragmentation mechanisms is a Newton diagram, which is a representation of the correlated momentum of the fragments in molecular frame. The Newton diagram for $C^+:S^+:S$ and $S^+:S^+:C$ channel due

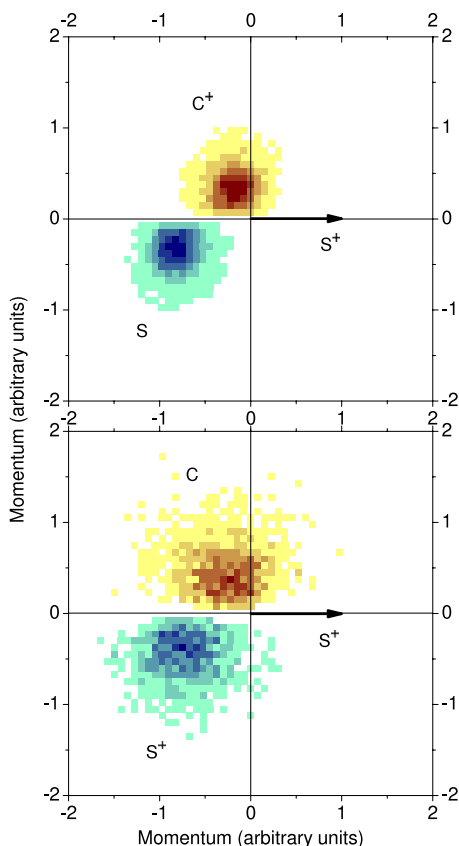


FIG. 4. Newton diagram of (upper) $C^+ : S^+ : S$ channel and (lower) $S^+ : S^+ : C$ channel for $(3h - 1p)$ Auger state. Normalized momentum distributions of the fragments are mapped with respect to the second ionic fragment in each case, shown by the arrow along x -axis. The fragment carbon and the sulphur atom are shown in the upper and lower half of each plot, respectively. The false color intensity scale increases from light to dark.

to $(3h - 1p)$ ionizations is shown in Fig. 4. For both channels, the momentum of the second fragment (S^+) is taken as the reference and shown as a unit vector along x -axis, while the momenta of the two other partners are normalized with respect to the second fragment and are mapped in the upper and lower half of the diagram, respectively. We have studied the fragmentation mechanisms of $C^+ : S^+ : S$ and $S^+ : S^+ : C$ channels for both $(6\sigma_g^{-2}, 5\sigma_u^{-2}, 6\sigma_g^{-1}5\sigma_u^{-1})$ and $(3h - 1p)$

Auger states and they are found to exhibit similar behaviour; hence, we show here the results for only $(3h - 1p)$ ionization. If the dissociation is sequential, a semi-circular feature appears in the momentum map due to the rotation of the diatomic intermediate prior to the second bond break.²⁹ Such a feature is observed by Lavollée²⁰ for tricationic fragmentation channel $C^+ : S^+ : S^+$, when kinetic energy of C^+ is high. In our case, the absence of such feature rules out the possibility of sequential break-up for both channels. This is in contrast to some earlier reports which suggest a sequential break-up based on ion-ion coincidence island slope for CS_2^{2+} dissociation upon $S(2p)$ Auger decay²⁷ as well as upon valence ionization.³⁰ Furthermore, non-zero momentum of the C and C^+ in the two channels suggests that three-body break-up of CS_2^{2+} is mostly from bent states. That is, CS_2^{2+} precursor ions leading to complete atomization do not retain the inversion symmetry, falling to C_{2v} or even lower symmetry. Dissociation from a bent precursor ion is also reported for $C^+ : S^+ : S^+$ channel²⁰ when the C^+ fragment has an intermediate kinetic energy.

This point can be further addressed by the Dalitz plot³¹ technique, which reveals the dication geometry at the instant of the break-up. The geometry information is revealed by computing the correlated momenta of the fragments in terms of reduced energy which forms the co-ordinate of these plots. The co-ordinates of the Dalitz plot³² are given by

$$\text{DalitzX} = \sqrt{\frac{M}{m_S} \frac{E_{S_1} - E_{S_{2,N}}}{3E}}, \quad (1)$$

$$\text{DalitzY} = \frac{M}{m_C} \frac{E_C}{3E} - \frac{1}{3}, \quad (2)$$

where M is the mass of the molecule, and m_S and m_C are masses of sulphur and carbon atoms, respectively. E_{S_1} is the kinetic energy of the first sulphur fragment to be detected and $E_{S_{2,N}}$ is the same for the second sulphur atom either singly charged or neutral as the case may be. E_C is the kinetic energy of carbon atom and E is the total KER from the fragmentation process. Each point in the Dalitz plot represents a certain momentum vector geometry of the CS_2^{2+} precursor ion at the time of break-up as illustrated in Fig. 5(a) for a few points.

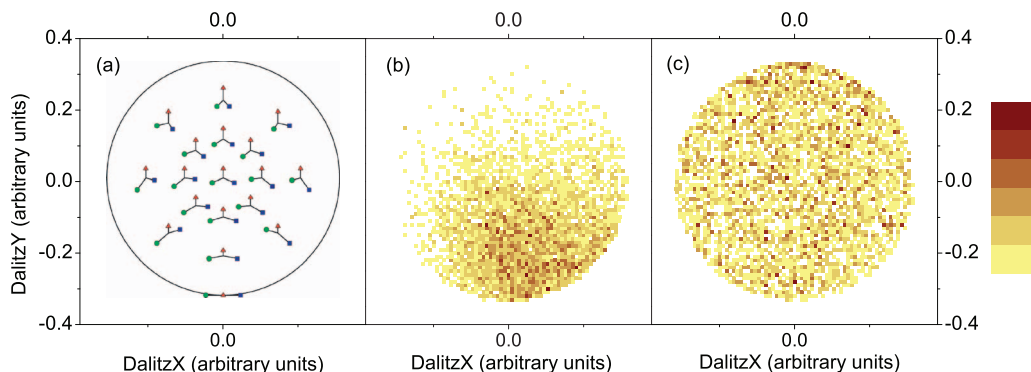


FIG. 5. (a) Characteristic momentum vector geometry of CS_2^{2+} precursor ion in Dalitz plot. \blacktriangle (red) denotes the momentum of the carbon ion, while \blacksquare (blue) marks the momentum of the first sulphur fragment to be detected. \bullet (green) gives the momentum of the other sulphur atom either singly charged or neutral as the case may be. (b) Dalitz plot for $C^+ : S^+ : S$ channel and (c) Dalitz plot for $S^+ : S^+ : C$ channel. The fragmentation channels are for $(3h - 1p)$ Auger ionizations only. The color bar indicates intensity.

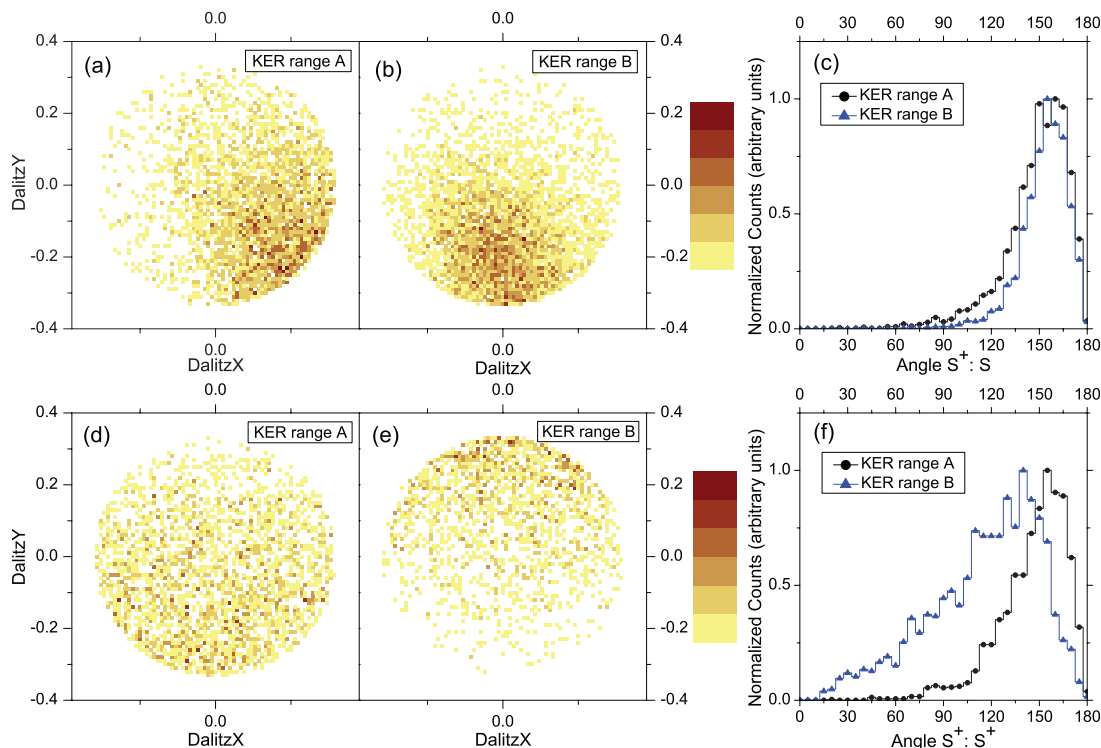


FIG. 6. (a) Dalitz plot of $C^+:S^+:S$ for KER range A, and (b) for KER range B. (c) Angle between momentum vectors of S^+ and S fragments upon $C^+:S^+:S$ break-up. (d) Dalitz plot of $S^+:S^+:C$ for KER range A, and (e) for KER range B. (f) Angle between momentum vectors of S^+ and S^+ fragments upon $S^+:S^+:C$ break-up. The fragmentation channels are for $(3h - 1p)$ Auger ionizations only. The color bar indicates intensity.

The Dalitz plots for three body fragmentation via $C^+:S^+:S$ and $S^+:S^+:C$ channels are shown in Figs. 5(b) and 5(c), respectively. For $C^+:S^+:S$ fragmentation we see that not only does the precursor ion mostly have a bent geometry as indicated earlier by the non-zero momentum of C^+ , but also there is an asymmetric stretch of the $C^+ - S^+$ bond in many cases prior to break-up. Thus the CS_2^{2+} precursor ion belongs to either C_{2v} (for bending only) or C_s (for bending with asymmetric stretch of the $C^+ - S^+$ bond) point group. The Dalitz plot for $S^+:S^+:C$ channel on the other hand suggests that the fragmentation occurs from precursor ions having all possible geometries, i.e., any bond angle is possible. To investigate the precursor geometry for different molecular ion states we present the Dalitz plots for different kinetic energy ranges in Fig. 6.

The KER ranges A and B for $C^+:S^+:S$ channel are from 0–17 eV and 17–40 eV while for $S^+:S^+:C$ channel are 0–14 eV and 14–40 eV, respectively. The selection of the range is arbitrary and is chosen such that KER range A spans from zero to a few eV above the modal KER, while KER range B covers the higher energy tail part. Figs. 6(a) and 6(b) show the Dalitz plots for the two KER ranges while Fig. 6(c) depicts the angle between the momenta of S^+ and S fragments for the same when dissociation takes place via $C^+:S^+:S$ channel. For this channel, it is clear that dissociations yielding lower KER and hence may as well be from lower energy states are due to precursor molecular ions in which the $C^+ - S^+$ bond is asymmetrically stretched. For higher KER range, which may arise due to dissociation from repulsive molecular ion states of higher energy, no asymmetric bond stretching oc-

cur. The bending of the molecule is similar in both the cases as can be seen in Fig. 6(c). The KER range dependent Dalitz plots and the angle between momentum vectors of the two sulphur atoms for $S^+:S^+:C$ break-up are shown in Figs. 6(d)–6(f). In this case, both the Dalitz plots and the angular correlation of the sulphur atoms indicate that fragmentation from molecular ions which have a less bent geometry lead to lower KER as compared to those with highly bent geometries. Theoretical calculations are clearly needed to identify the molecular ion states which yield precursor geometry dependent KER.

IV. CONCLUSION

The fragmentation kinematics of CS_2^{2+} in various electronic configurations, attained following $S(2p)$ Auger transitions is presented. In agreement with previous studies we find that CS_2^{2+} states accessed by ejection of high kinetic energy Auger electrons (i.e., due to electronic decay from low binding energy orbitals) are stable in nature and are the dominant channel when the final state has an electronic configuration of $2\pi_g^{-2}$. Unstable states are only attained when electrons from highly bound orbitals are involved in Auger decay producing low kinetic energy Auger electrons; hence, energy available to the nuclear degrees of freedom is adequate for bond rupture. Two body break-up is dominant for ionization to dissociative states that are lower in binding energy while the cross-section of three-body fragmentation increases as higher energy states are accessed. For all dication fragmentation channels, the KER range remains the same for various $S(2p)$ Auger transitions, while the mean KER increases

(but not significantly) for dissociation following ionization to higher binding energy Auger states. This points towards the possibility that though CS_2^{2+} gains more energy as highly bound orbitals are ionized due to Auger decay, most of the parent molecular ion energy is partitioned as internal energy of the fragment ions than as their kinetic energy. Alternatively, the energy of the excited dication may also be expelled in the form of photons, thus yielding lower KER upon dissociation.

All three-body break-ups are concerted and the precursors are mostly in bent geometries. For some precursor ions giving rise to $\text{C}^+:\text{S}^+:\text{S}$ channel, asymmetric stretching of the C^+-S^+ bond along with bending occurs. These unstable molecular ions give low KER upon dissociation whereas precursor ions with no asymmetric stretching of the bonds (but of bent geometry) yield higher KER. The degree of bending for both types of precursor ions of $\text{C}^+:\text{S}^+:\text{S}$ channel is found to be same. The CS_2^{2+} precursor ions of $\text{S}^+:\text{S}^+:\text{C}$ break-up can have any geometry. In this case, molecular ions which undergo greater bending yield higher KER than those from less bent ones. Precursor states giving low KER may be lower in energy than the states producing higher KER. Theoretical calculations are needed to pin-point the molecular states giving rise to precursor geometry dependent KER.

- ¹W. Eberhardt, T. Sham, R. Carr, S. Krummacher, M. Strongin, S. Weng, and D. Wesner, *Phys. Rev. Lett.* **50**, 1038 (1983).
- ²W. Eberhardt, J. Stöhr, J. Feldhaus, E. Plummer, and F. Sette, *Phys. Rev. Lett.* **51**, 2370 (1983).
- ³J. Murakami, M. Nelson, S. Anderson, and D. Hanson, *J. Chem. Phys.* **85**, 5755 (1986).
- ⁴C. Miron, M. Simon, N. Leclercq, D. Hansen, and P. Morin, *Phys. Rev. Lett.* **81**, 4104 (1998).
- ⁵X. J. Liu, G. Prümper, E. Kukk, R. Sankari, M. Hoshino, C. Makochekanwa, M. Kitajima, H. Tanaka, H. Yoshida, Y. Tamenori, and K. Ueda, *Phys. Rev. A* **72**, 042704 (2005).
- ⁶W. Eberhardt, E. Plummer, I.-W. Lyo, R. Carr, and W. Ford, *Phys. Rev. Lett.* **58**, 207 (1987).

- ⁷R. Murphy and W. Eberhardt, *J. Chem. Phys.* **89**, 4054 (1988).
- ⁸U. Alkemper, R. Hörnig, and F. von Busch, *J. Phys. B* **29**, 35 (1996).
- ⁹D. Céolin, O. Travnikova, Z. Bao, M. Piancastelli, T. Tanaka, M. Hoshino, H. Kato, H. Tanaka, J. Harries, Y. Tamenori, C. Prümper, T. Lischke, X. J. Liu, and K. Ueda, *J. Chem. Phys.* **128**, 024306 (2008).
- ¹⁰J. Risley, *Rev. Sci. Instrum.* **43**, 95 (1972).
- ¹¹K. Saha, S. Banerjee, and B. Bapat, *Rev. Sci. Instrum.* **84**, 073101 (2013).
- ¹²W. Wiley and I. McLaren, *Rev. Sci. Instrum.* **26**, 1150 (1955).
- ¹³A. Krasnoperova, E. Gluskin, and L. Mazalov, *J. Struct. Chem.* **18**, 206 (1977).
- ¹⁴R. G. Hayes and W. Eberhardt, *J. Chem. Phys.* **94**, 6398 (1991).
- ¹⁵P. Lablanquie, I. Nenner, P. Millie, P. Morin, J. Eland, M. Hubin-Franskin, and J. Delwiche, *J. Chem. Phys.* **82**, 2951 (1985).
- ¹⁶P. Millie, I. Nenner, P. Archirel, P. Lablanquie, P. Fournier, and J. Eland, *J. Chem. Phys.* **84**, 1259 (1986).
- ¹⁷M. Hochlaf, R. Hall, F. Penent, J. Eland, and P. Lablanquie, *Chem. Phys.* **234**, 249 (1998).
- ¹⁸D. Minelli, F. Tarantelli, A. Sgamellotti, and L. Cederbaum, *J. Chem. Phys.* **107**, 6070 (1997).
- ¹⁹U. Alkemper and F. Von Busch, *J. Electron Spectrosc. Relat. Phenom.* **93**, 115 (1998).
- ²⁰M. Lavollée, *Rev. Sci. Instrum.* **70**, 2968 (1999).
- ²¹M. Hochlaf, G. Chambaud, and P. Rosmus, *J. Chem. Phys.* **108**, 4047 (1998).
- ²²J. Eland, *Laser Chem.* **11**, 259 (1991).
- ²³S. Hsieh and J. Eland, *J. Phys. B* **30**, 4515 (1997).
- ²⁴Y. Muramatsu, K. Ueda, N. Saito, H. Chiba, M. Lavollée, A. Czasch, T. Weber, O. Jagutzki, H. Schmidt-Böcking, R. Moshhammer, U. Becker, K. Kubozuka, and I. Koyano, *Phys. Rev. Lett.* **88**, 133002 (2002).
- ²⁵J. Laksman, E. Månsson, C. Grunewald, A. Sankari, M. Gisselbrecht, D. Céolin, and S. Sorensen, *J. Chem. Phys.* **136**, 104303 (2012).
- ²⁶J. Eland, C. Rigby, E. Andersson, J. Palaudoux, L. Andric, F. Penent, P. Linusson, L. Hedén, L. Karlsson, J.-E. Rubensson, Y. Hikosaka, K. Ito, P. Lablanquie, and R. Fiefel, *J. Chem. Phys.* **132**, 104311 (2010).
- ²⁷U. Ankerhold, B. Esser, and F. von Busch, *Chem. Phys.* **220**, 393 (1997).
- ²⁸F. von Busch, *J. Phys. B* **34**, 431 (2001).
- ²⁹N. Neumann, D. Hant, L. Schmidt, J. Titze, T. Jahnke, A. Czasch, M. Schöffler, K. Kreidi, O. Jagutzki, H. Schmidt-Böcking, and R. Dörner, *Phys. Rev. Lett.* **104**, 103201 (2010).
- ³⁰J. Eland, *Mol. Phys.* **61**, 725 (1987).
- ³¹R. Dalitz, *Philos. Mag. Series 6* **44**, 1068 (1953).
- ³²L. Lammich, Ph.D. dissertation, University of Heidelberg 2004, <http://nbn-resolving.de/urn:nbn:de:bsz:16-opus-48331>, pp. 111–114.